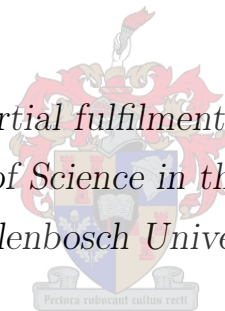


Development of VUV tunable Laser Spectroscopy Techniques for Characterizing Calcium Fluoride

by

Tresor MATINDI

*Thesis presented in partial fulfilment of the requirements for
the degree of Master of Science in the Faculty of Science at
Stellenbosch University*



Department of Physics,
University of Stellenbosch,
Private Bag X1, Matieland 7602, South Africa.

Supervisors:

Dr. Christine.M. Steenkamp

Prof. Erich.G. Rohwer

December 2014

Declaration

By submitting this thesis electronically, I declare that the entirety of the work contained therein is my own, original work, that I am the sole author thereof (save to the extent explicitly otherwise stated), that reproduction and publication thereof by Stellenbosch University will not infringe any third party rights and that I have not previously in its entirety or in part submitted it for obtaining any qualification.

Date:

Copyright © 2014 Stellenbosch University
All rights reserved.

Abstract

The large band gap (approximately 11.5-12.1 eV) and high transmission of calcium fluoride (CaF_2) crystal in the ultraviolet (UV) and vacuum ultraviolet (VUV) region makes it an important material for optics for laser applications in UV. However, CaF_2 degrades during long exposure to UV irradiation due to defect generation. The formation of self-trapped excitons (STE) is considered the first step in defect generation. In this project the possibility of observing STE states in CaF_2 using a narrow bandwidth tunable VUV laser source is investigated. This is the first spectroscopy study of an alkaline earth fluoride using VUV tunable laser radiation instead of a fixed wavelength laser. The use of a VUV tunable laser source has potential for determining the energies of the STE states, which are unknown. Our main objective is addressed by developing techniques to measure absorption spectra of pure and doped CaF_2 samples, using a VUV scanning monochromator and a tunable VUV laser, and by doing a literature study. The results obtained with the scanning monochromator show absorption features in 126-180 nm range of all our samples. These vary for different samples and correlate with information from the supplier on the samples' fluorescence spectra. Total absorption of the VUV light by CaF_2 in the 115-126 nm range is observed. With the narrow bandwidth tunable laser light, absorption spectra were obtained in the range of 143-146.7 nm of all our CaF_2 samples. No significance peaks which can be related to the STE states in CaF_2 were observed in the VUV laser absorption spectra, but the results are valuable to improve the technique. The conclusion is that either a different spectral range or fluorescence detection can be investigated in future.

Opsomming

Die groot bandgaping (ongeveer 11.5-12.1 eV) en hoë transmissie van kalsiumfluoried (CaF_2) kristal in die ultraviolet (UV) en die vakuum ultraviolet (VUV) gebied maak dit 'n belangrike materiaal vir optika vir laser toepassings in die UV. CaF_2 degradeer egter gedurende langdurige blootstelling aan UV lig as gevolg van die generering van defekte. Die vorming van 'n elektron-holte paar wat deur die kristalstruktuur gestabiliseer word teen rekombinasie (self-trapped excitons, afgekort STE) word beskou as die eerste stap in defek generering. In hierdie projek word die moontlikheid ondersoek om STE toestande in CaF_2 waar te neem deur die gebruik van 'n afstembare VUV laserbron met emissie in 'n smal spektrale band. Dit is die eerste spektroskopiese studie van 'n aardalkali-fluoried deur die gebruik van afstembare VUV laserlig in plaas van 'n vaste golflengte laser. Die gebruik van 'n afstembare VUV laserbron het potensiaal vir die bepaling van die energieë van die STE toestande, wat onbekend is. Ons hoofdoel word aangespreek deur die ontwikkeling van tegnieke vir die meet van absorpsie spektra van suiwer en gedoteerde CaF_2 monsters met behulp van 'n VUV skanderende monochromator en 'n afstembare VUV laser, en deur 'n literatuurstudie. Die resultate wat behaal is met die skanderende monochromator toon die absorpsieprofiële van al ons monsters in die 126-180 nm spektrale gebied. Die absorpsieprofiële varieer vir die verskillende monsters en korreleer met die inligting van die verskaffer oor die fluoressensie spektra van die monsters. Totale absorpsie van die VUV lig deur CaF_2 in die 115-126 nm gebied is waargeneem. Met die smalband afstembare laserlig is absorpsie spektra in die 143-146.7 nm gebied vir al ons CaF_2 monsters verkry. Geen beduidende pieke wat verband hou met die STE toestande in CaF_2 is waargeneem in die VUV laser absorpsie spektra nie, maar die resultate is waardevol vir die verbetering van die tegniek. Die gevolgtrekking is dat of 'n ander spektraalgebied of fluoressensiedeteksie in die toekoms ondersoek kan word.

Acknowledgement

This research project would not have been possible without the support of many people.

I wish to express my gratitude to my supervisor, Dr Christine Steenkamp who was abundantly helpful and offered invaluable assistance, support and guidance.

Deepest gratitude are also due to my co-supervisor Prof Erich Rohwer without whose knowledge and assistance this study would not have been successful.

Special thanks to Mr U.G.K Deutschländer, Mr J. M. Germishuizen, B. Botha and J. Burns for a the technical assistance they contributed towards this project for always being available for technical matters.

Thanks to you Charles Rigby and Andre De Bruyn for helping me during my experiment.

I wish to express my love and gratitude to my beloved families; for their understanding and endless love, through the duration of my studies.

Special thanks to you Brandy Matindi for your prayers, support and love.

I would also like to acknowledge the African Institute for Mathematical Sciences (AIMS), the University of Stellenbosch and the African Laser Centre (ALC) for funding my MSc studies.

This work is based on the research supported in part by the National Research Foundation of South Africa. The Grantholder acknowledges that opinions, findings and conclusions or recommendations expressed in any publication generated by the NRF supported research are that of the author, and that the NRF accepts no liability whatsoever in this regard.

The CSIR National Laser Centre through the Rental Pool Programme provided financial support to this Project.

Contents

Declaration	i
Abstract	ii
Opsomming	iii
Acknowledgement	iv
Contents	v
List of Figures	vii
List of Tables	xi
1 Introduction and aims	1
1.1 Introduction	1
1.2 Aims	2
1.3 Outline of thesis	2
2 Theory of the generation of tunable vacuum ultraviolet (VUV) laser light	3
2.1 Third order sum-frequency generation	4
2.2 Resonant enhancement	9
2.3 Phase matching	11
2.4 Beam polarisation	14
3 Principles of a grating monochromator	16
3.1 Grating theory	16
4 Literature study on VUV spectroscopy of CaF₂ crystals	22
4.1 Properties of CaF ₂ crystals	22
4.2 Steady state spectra of pure and doped CaF ₂	23

<i>CONTENTS</i>	vi
4.3 Pulsed laser spectroscopy of CaF ₂	24
4.4 Model of M _{Na} center formation and annealing	26
5 Experimental Setups	38
5.1 Experimental setup of McPherson Model 225 monochromator	38
5.2 Experimental setup of the VUV laser source	41
5.3 Experimental setup for absorption measurements of CaF ₂ using the VUV laser source	43
6 Results and discussion	45
6.1 Characterisation of the McPherson 225 monochromator	45
6.2 Measurement procedures and data processing with the monochromator . .	61
6.3 Absorption spectra of CaF ₂ using the monochromator	67
6.4 Characterisation of the VUV laser source	79
6.5 Absorption spectra of CaF ₂ using VUV laser source	82
7 Conclusions	91
7.1 Summary	91
7.2 Conclusion regarding methods	92
7.3 Conclusion regarding the possibility to observe STE states.	92
7.4 Future work	93
Appendices	94
A Result and discussion	95
A.1 Data Processing	95
List of References	102

List of Figures

2.1	Diagrammatic illustration of four-wave sum-frequency mixing.	3
2.2	Diagrams illustrating of the resonances that enhance the sum-frequency generation process. (a) One-photon resonance, (b) Two-photon resonance, and (c) Three-photon resonance.	10
3.1	Illustration of diffraction by a plane grating.	17
3.2	Sketch of the optical path length of a monochromator.	18
4.1	The crystal lattice structure of Calcium Fluoride.	22
4.2	Illustration of the optical excitation and the non-radiative and fluorescing (LIF) relaxation pathways.	25
4.3	Diagram of laser induced generation and annealing of M_{Na} centers in CaF_2 [1].	27
5.1	Schematic illustration of the experimental setup for absorption measurements of CaF_2 with a McPherson Model 225 monochromator. Components are not drawn to scale. The vacuum system is not shown.	38
5.2	Schematic illustration of the McPherson 225 monochromator vacuum system	40
5.3	Photo of the new setup in which the sample cell is under vacuum.	41
5.4	Schematic illustration of the setup for wavelength calibration.	41
5.5	Diagram of the experimental setup for the generation of tunable VUV by sum-frequency mixing. Details of the heat pipe oven setup are not shown.	42
5.6	Setup of absorption measurements of CaF_2 using the VUV laser source. The vacuum pumps and gauges are not shown.	44
6.1	Emission spectrum of mercury lamp recorded with PMT R106.	46
6.2	Plot of mercury lines from NIST tables	46
6.3	Comparison of the experimental spectrum against the plot of the mercury lines from NIST tables.	47
6.4	Plot of mercury line wavelengths from NIST tables against the counter reading divided by 2.	47

6.5	Deuterium lamp spectra recorded in 1 bar N ₂ , with an entrance slit fix at 200 μm while the exit slits was successively change to 200,400, 600, 800 and 1000 micrometer.	49
6.6	Plot of the height and width of the peaks of the first set of measurements against the slit width. For this example the peak at 160 nm was considered and its width is determined by the full width at 3/4 maximum.	49
6.7	Deuterium lamp spectra recorded in 1 bar N ₂ , with the exit slit fix at 200 μm while the entrance slits was successively changed to 200, 400, 600, 800 and 1000 micrometer.	50
6.8	Plot of the height and width of peaks of the second set of measurements against the slit width. For this example the peak at 160 nm was considered and the width is determine by the full width at 3/4 maximum.	51
6.9	Deuterium lamp spectra recorded in 1 bar N ₂ , with both entrance and exit slits in the same width.	51
6.10	Plot of the height and width of peaks of the third set of measurements against the slit width. For this example the peak at 160 nm was considered and the width is determining by the full width at 3/4 maximum.	52
6.11	Comparison of two Deuterium lamp spectrum recorded with different slit widths. Both entrance and exit slit widths are set to 1000 μm (left hand graph) and 200 μm (right hand graph)	53
6.12	Deuterium lamp spectra recorded in vacuum, 1 bar N ₂ and Ar.	54
6.13	Residual oxygen absorption in the monochromator.	56
6.14	Decrease of lamp intensity over time.	59
6.15	Decrease of lamp intensity over time over a month.	60
6.16	Decrease of lamp intensity over time and the effect of window cleaning. The horizontal line at * is due to the signal being larger than the upper limit of the analogue to digital converter	61
6.17	Example of two deuterium lamp spectra (115-150 nm) measured with and without the sample in the light path.	63
6.18	A small part of spectra A and B. Before (left hand side) calibration and after (right hand side)of B relative to A.	65
6.19	Illustration of data points of two spectra before (a) and after (b) interpolation.	66
6.20	Absorption spectrum of the pure calcium fluoride sample (sample A) in the VUV range	68
6.21	Superposition of the absorption spectrum of the pure calcium fluoride sample (sample A)with the graph which contains peaks of oxygen absorption in the VUV range.	69

6.22	Illustration of two absorption spectra of a same CaF ₂ sample measured with (right hand side) and without (left hand side) the extra tube.	70
6.23	Absorption measurements (130-180 nm) of pure and doped calcium fluoride samples recorded with sample cell purge with 1 bar nitrogen 5.0. The spectra were taken without the use of the extra tube to keep the optical path length in the gas the same. The graphs are label by the sample labels A-G. For the larger graph see appendix A.1.0.2.	71
6.24	Absorption measurements (130-180 nm) of CaF ₂ samples recorded with sample cell under vacuum. The graphs are labeled by the sample labels A-G. For larger graphs see appendix A.1.0.3.	72
6.25	Absorption measurements of pure and doped calcium fluoride samples recorded with sample cell purge with 1 bar nitrogen 5.0. Subfigures are labelled with the letters A-G corresponding to labels at samples as on page 6.2.4. For larger graphs see appendix A.1.1.	74
6.26	Broadband absorption spectra of pure CaF ₂ sample (sample A) at the room temperature.	74
6.27	Absorption spectra of pure CaF ₂ sample (sample A) at the room temperature. Measurement were done with an evacuated sample cell (Pressure: 3×10^{-6} mbar).	75
6.28	Emission spectra of Deuterium lamp in vacuum, recorded with and without CaF ₂ sample in the path length. Spectra B and D are two Deuterium lamp spectrum taken with the empty sample cell at the beginning, while spectra F and H are the recorded Deuterium lamp spectrum taken with a pure CaF ₂ sample in the path length. Spectra J and L, are respectively the last two measurement taken after removing the sample into the path length.	76
6.29	Emission spectra of Deuterium lamp with and without sample after subtracting the average intensity of the stray light in the range 115-125 nm from all the data sets.	77
6.30	Room temperature absorption spectra of pure CaF ₂	78
6.31	True absorption spectra of pure and doped calcium fluoride samples recorded with sample cell purge with 1 bar nitrogen 5.0. Subfigures are labelled with the letters A-G corresponding to labels at samples as on page 6.2.4. For large graphs see appendix A.1.1.1.	79
6.32	Resonance curve of the third harmonic generation	80
6.33	Experimental phase matching curve.	81
6.34	Experimental spectrum of sum-frequency.	82
6.35	Sensitivity curves of PMTs	83

6.36	VUV light recorded simultaneously with two PMTs without a sample in the evacuated sample cell. This graph shows the difference between signal magnitudes with two PMTs of which the output intensity signals were perfectly adjusted at the same level using an oscilloscope.	84
6.37	Illustration of the PMT signal normalisation. PMT_1 represent a spectrum of sum-frequency generation recorded with the first PMT while PMT_2 is the spectrum recorded with the second PMT multiplied by the normalisation factor (the ration of the mean signal before normalisation).	85
6.38	VUV spectra of sample E before(in left) and after (in right) performing the PMTs normalisation. The normalisation was done with the multiplication factor equal to 2.57.	86
6.39	Absorption measurements of sample A using the tuneable VUV laser source. Measurements without (I_o) and with sample (I). Absorption spectrum on the right hand side.	87
6.40	Absorption measurements of calcium fluoride samples using the tuneable VUV laser source. Measurements without (I_o) and with sample (I). Absorption spectrum on the right hand side. The graphs are label by the sample labels B-D	88
6.41	Absorption measurements of calcium fluoride samples using the tuneable VUV laser source. Measurements without (I_o) and with sample (I). Absorption spectrum on the right hand side. The graphs are label by the sample labels E-G	89

List of Tables

5.1	Optical specifications of the McPherson Model 225 monochromator	39
6.1	Peak Characteristics for the three sets of measurements. The first, second and third sets represents the three set of measurements. First set: entrance slit 200 μm wide, exit slit varied. Second set: exit slit 200 μm wide, entrance slit width varied. Third set: both slit widths varied together.	52
6.2	Specification Afrox argon Baseline 5.0 and nitrogen Baseline 5.0	55
6.3	Different experimental conditions used during the VUV laser absorption measurements of samples A-G	87

Chapter 1

Introduction and aims

1.1 Introduction

Calcium fluoride (CaF_2) with its large band gap around 12 eV is considered as one of the most important materials for high power laser applications in the ultra violet range since it has an excellent transmission and shows high damage laser thresholds [1, 2]. However, even the so-called high purity calcium fluoride crystal contains minimal traces of impurities which strongly affect its durability and cause a decrease of its transmission under a high VUV irradiation [2]. Therefore the knowledge about defect energy levels, their lifetimes and relaxation mechanisms is necessary.

The degradation of CaF_2 crystal upon high laser irradiation is caused by defect generation and annealing. The process of defect generation in a high purity calcium fluoride crystal is induced by two-photon absorption of UV light (e.g. ArF_2 laser light at 193 nm) and relaxation to self-trapped excitons (STE) [3]. Self trapped excitons in CaF_2 are considered to be the origin of nearly all defect generation processes as it interacts with impurities to form defects [1]. The STE's have energy levels in the band gap. However, to date the exact energy levels of self trapped excitons in CaF_2 are still unknown.

The possible methods for characterising the defect and defect formation in CaF_2 are absorption, excitation and fluorescence emission spectroscopy. A narrow bandwidth tunable VUV laser source has to our knowledge never been used before to do spectroscopy of CaF_2 . Exciting the CaF_2 by a tunable laser source, instead of a fixed wavelength laser may show the energies of the STE energy levels.

The spectroscopy study of CaF_2 can be conducted using tunable vacuum ultraviolet (VUV) laser light with a narrow spectral bandwidth (< 10 ns pulses), which is developed in our

laboratory. This VUV laser source is generated by a third order nonlinear optical process because there is no frequency tunable laser source in the VUV range commercially available. McPherson model 225 vacuum scanning monochromator, which operates with a deuterium lamp McPherson model 632, is also available in our laboratory for absorption measurement over a wider spectral range at a lower spectral resolution. As the VUV light is strongly absorbed by air, the spectroscopy study of CaF_2 in this range are done in vacuum or inert gas atmosphere of high purity.

1.2 Aims

The scientific question in this thesis is the possibility of observing the STE states in the CaF_2 using a narrow-bandwidth tunable VUV laser. This question has been addressed in this thesis by developing techniques to measure absorption spectra of seven pure and doped CaF_2 samples, using a VUV scanning monochromator and a tunable VUV laser, and to do a literature study on the state of knowledge on self-trapped excitons and related defects in crystals.

1.3 Outline of thesis

Chapter 2 is devoted on the theory of the generation of tunable vacuum VUV laser light. The role of resonant enhancement, phase matching and circular polarisation in the optimization of the intensity of the generated sum-frequency are highlighted.

Chapter 3 discusses principles of a grating monochromator. An overview on the theories of dispersion, resolving power, spectral bandpass and stray and scattered light are provided.

The literature study on the state of knowledge on self-trapped excitons and related defects in calcium fluoride crystals are given in Chapter 4.

Chapter 5 is dedicated to the experimental setups used for generating the tunable VUV laser light and for measuring absorption spectra of pure and doped CaF_2 samples with the VUV scanning monochromator and the VUV laser light.

Chapter 6 contained the experimental results and discussion of the absorption measurements of CaF_2 samples obtained with McPherson model 225 vacuum scanning monochromator and tunable VUV laser light.

A final summary and some proposals for future research are presented Chapter 7.

Chapter 2

Theory of the generation of tunable vacuum ultraviolet (VUV) laser light

It is known that a frequency tunable laser that produce a narrow bandwidth beam is a most useful source for applications in laser spectroscopy [4]. These kind of laser sources are available only in the visible, infra-red and near ultraviolet regions. Vacuum ultraviolet lasers that are tunable and produce a narrow bandwidth light are not commercially available. However, tunable narrow-bandwidth laser light can be generated by nonlinear processes, generally by using gaseous nonlinear media, since the nonlinear crystals are usually opaque in the vacuum ultraviolet range [4].

The generation of tunable vacuum ultraviolet laser light is based on the interaction of two incident laser beams at frequencies ω_1 and ω_2 with a nonlinear medium that has a non-zero third order susceptibility. During this interaction a new laser beam at the sum-frequency $\omega_3 = 2\omega_1 + \omega_2$ is generated [4] as illustrated in Figure 2.1. This process is called four-wave sum-frequency mixing.

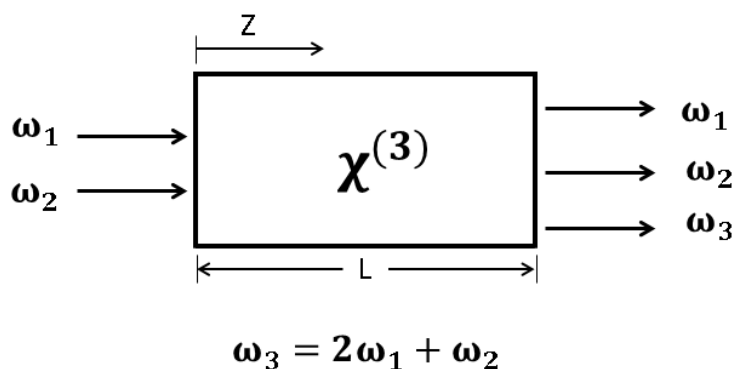


Figure 2.1: Diagrammatic illustration of four-wave sum-frequency mixing.

Apart from the sum-frequency generation, there are other competing processes such as difference-frequency and third harmonic generation, which also take place in the medium. Phase matching and beam polarisation are used to discriminate against the undesired processes.

This chapter emphasizes the optimization of the intensity of the generated sum-frequency wave by resonant enhancement and shows how it can be made the dominant process in the nonlinear medium. More details about the generation of VUV light can be found in [5].

2.1 Third order sum-frequency generation

Consider a nonlinear medium that contains no free charge. Let us assume that this medium is non-magnetic, lossless and isotropic. Nonlinear optical process in this medium is governed by the fundamental equation of nonlinear optics [6]

$$\nabla \times \nabla \times \vec{E}_n(r, t) + \frac{\epsilon^1(\omega_n)}{c^2} \frac{\partial^2 \vec{E}_n(r, t)}{\partial t^2} = \frac{-4\pi}{c^2} \frac{\partial^2 P_n^{\vec{N}L}(r, t)}{\partial t^2} \quad (2.1.1)$$

where $P_n^{\vec{N}L}$ is the nonlinear polarization at the frequency ω_n , $\vec{E}_n(r, t)$ is the electric field at ω_n generated by $P_n^{\vec{N}L}$ and ϵ^1 is the dielectric constant of the nonlinear medium. Note that the cgs units are used throughout this chapter.

It is assumed that this medium is dispersive and isotropic and every electric field involved in this process has a fixed polarization direction and can be described as a plane wave propagating in the z-direction. The consequence is that the three electric fields $\vec{E}_n(r, t)$ (incidents and generated waves) can now be considered as a scalars. Thus :

$$E_n(z, t) = E_n(z) e^{-i\omega_n t} + c.c. = A_n e^{i(k_n z - \omega_n t)} + c.c. \quad \text{for } n = 1, 2, 3 \quad (2.1.2)$$

with $k_n = \frac{n_n \omega_n}{c}$, $n_n = \sqrt{\epsilon^1(\omega)}$. In the equation (2.1.2) c.c. represents the complex conjugate.

The amplitudes $A_n(z)$ are not constant due to the nonlinear interaction which takes place in the medium. However, in the case where the intensities of the incident light beams are high and not influenced significantly by the nonlinear process, the variation of A_1 and A_2 can be ignored. Therefore, we can assume that the expression (2.1.2) is the solution of the

fundamental equation of non linear optics.

Taking into consideration the assumption of plane waves propagating in the z-direction, one can simplify the nonlinear polarization that occurs in the equation (2.1.1) as follows:

$$P_n^{NL}(r, t) \longrightarrow P_n^{(3)}(z, t) = P_n^{(3)} e^{-i\omega_n t} + c.c. \quad (2.1.3)$$

for $n = 1, 2, 3$. P_n^{NL} is replaced by the third order component $P_n^{(3)}$ because that is the lowest non-zero order in an isotropic medium.

For deriving the wave equation for sum-frequency generation, let us consider equation (2.1.1) for $n = 3$. The first term on the left side $\nabla \times \nabla \times \vec{E}$ replaced by $-\nabla^2 \vec{E}$. This is valid since $\nabla \times \nabla \times \vec{E} = \nabla (\nabla \cdot \vec{E}) - \nabla^2 \vec{E}$ and for the conditions considered here [6] it can be shown that $\nabla \cdot \vec{E} = 0$.

Due to the dependence of the field in the z-direction, the operator $-\nabla^2$ can be replaced by $-\frac{\partial^2}{\partial z^2}$. Therefore the fundamental equation of nonlinear optics can be written as:

$$\frac{-\partial^2 [E_n(z) e^{-i\omega_n t}]}{\partial z^2} + \frac{\epsilon^1(\omega_n) \partial^2 [E_n(z) e^{-i\omega_n t}]}{c^2 \partial t^2} + c.c = \frac{-4\pi \partial^2 [P_n^{(3)}(z) e^{-i\omega_n t}]}{c^2 \partial t^2} + c.c \quad (2.1.4)$$

In the above equation $P_n^{(3)}(z)$ is the polarization responsible for the generation of the sum-frequency [6] and is given by :

$$P_3^{(3)}(z) = 3\chi^{(3)}(\omega_3, \omega_1, \omega_1, \omega_2) E_1(z) E_1(z) E_2(z) \quad (2.1.5)$$

$$= 3\chi^{(3)}(\omega_3, \omega_1, \omega_1, \omega_2) [A_1(z)]^2 A_2(z) e^{i(2k_1+k_2)z} \quad (2.1.6)$$

where $\chi^{(3)}(\omega_3, \omega_1, \omega_1, \omega_2)$ is the third order susceptibility responsible for sum-frequency generation $\omega_3 = 2\omega_1 + \omega_2$.

To shorten the above equation, we replace $\chi^{(3)}(\omega_3, \omega_1, \omega_1, \omega_2)$ with $\chi^{(3)}$.

Substituting the expressions (2.1.2), (2.1.3) and (2.1.6) into (2.1.4) and calculating the derivatives for the wave at the frequency ω_3 we get:

$$\begin{aligned} & \left[\frac{\partial^2 A_3}{\partial z^2} + 2ik_3 \frac{\partial A_3}{\partial z} - k_3^2 A_3 + \frac{\epsilon^{(1)}(\omega_3) \omega_3^2 A_3}{c^2} \right] e^{i(k_3 z - \omega_3 t)} + c.c. \\ & = -\frac{12\pi \omega_3^2 \chi^{(3)}}{c^2} [A_1(z)]^2 A_2(z) e^{i(2k_1+k_2)z - \omega_3 t} + c.c. \end{aligned} \quad (2.1.7)$$

Replacing the wave vector k_3 by the expression $k_3^2 = \frac{\epsilon^1(\omega)\omega_3^2}{c^2}$ into the last equation, the 3th and 4th terms of the left side of equation (2.1.7) cancel. In addition, the complex conjugate and the $e^{-i\omega_3 t}$ factor also cancel-out on both sides of equation (2.1.7) without changing its validity. Therefore, the equation (2.1.7) becomes:

$$\left[\frac{\partial^2 A_3}{\partial z^2} + 2ik_3 \frac{\partial A_3}{\partial z} \right] e^{i(k_3 z)} = -\frac{12\pi\omega_3^2 \chi^{(3)}}{c^2} [A_1(z)]^2 A_2(z) e^{i(2k_1+k_2)z} \quad (2.1.8)$$

As the field amplitude depend only on the z-direction, one can replace $\frac{\partial}{\partial z}$ by $\frac{d}{dz}$ without changing the validity of the equation. Thus we obtain the following equation:

$$\left[\frac{d^2 A_3}{dz^2} + 2ik_3 \frac{dA_3}{dz} \right] e^{i(k_3 z)} = -\frac{12\pi\omega_3^2 \chi^{(3)}}{c^2} [A_1(z)]^2 A_2(z) e^{i(2k_1+k_2)z} \quad (2.1.9)$$

Using the so-called slow varying amplitude approximation

$$\left| \frac{d^2 A_3}{dz^2} \right| \ll \left| k_3 \frac{dA_3}{dz} \right|, \quad (2.1.10)$$

the first term in (2.1.9) can be neglected and then (2.1.9) become:

$$\frac{dA_3}{dz} = \frac{i6\pi\omega_3^2 \chi^{(3)}}{k_3 c^2} [A_1(z)]^2 A_2(z) e^{i\Delta k z} \quad (2.1.11)$$

where $\Delta k = 2k_1 + k_2 - k_3$ is the wave vector mismatch.

For accuracy in describing sum-frequency generation in magnesium vapour medium, we must take into account the contribution of the one-photon absorption in the wave equation. According to the Beer-Lambert law, the intensity of the light passing through a medium is given by:

$$I(z) = I_0 e^{-\sigma N z} \quad (2.1.12)$$

where σ , N and z are respectively the absorption cross section, the number density of the gaseous medium and the length of the nonlinear medium.

Equation (2.1.12) can be rewritten in terms of amplitude

$$A(z) = A_0 e^{-\frac{1}{2}\sigma N z} \quad (2.1.13)$$

It follows that the differential of equation (2.1.13) with respect to z -direction is given by the following expression:

$$\frac{dA(z)}{dz} = -\frac{\sigma(\omega)N}{2}A(z) \quad (2.1.14)$$

which describes the influence of the one-photon absorption on amplitude $A(z)$.

Adding the contribution of one-photon absorption into the wave equation (2.1.11) we get:

$$\frac{dA_3}{dz} = \frac{i6\pi\omega_3^2\chi^{(3)}}{k_3c^2} [A_1(z)]^2 A_2(z) e^{i\Delta kz} - \frac{\sigma(\omega_3)N}{2}A_3(z) \quad (2.1.15)$$

It is important to emphasize that the extra term (last term on the right hand side of (2.1.15) equation) describes the attenuation of the wave due to one-photon absorption.

In the case where $|A_3| \ll |A_1|$ or $|A_2|$ (so-called signal limit), one can assume that the amplitudes of the incident laser beams A_1 and A_2 are only influenced significantly by the one-photon absorption and not by the nonlinear process [6]. Related to foregoing considerations, the expressions for A_1 and A_2 are:

$$\frac{dA_1(z)}{dz} = -\frac{\sigma(\omega_1)N}{2}A_1(z) \implies A_1(z) = A_1(z=0) e^{-\frac{\sigma(\omega_1)N}{2}z} \quad (2.1.16)$$

$$\frac{dA_2(z)}{dz} = -\frac{\sigma(\omega_2)N}{2}A_2(z) \implies A_2(z) = A_2(z=0) e^{-\frac{\sigma(\omega_2)N}{2}z} \quad (2.1.17)$$

The substitution of equations (2.1.16) and (2.1.17) into (2.1.15) leads to the following expression

$$\frac{dA_3}{dz} = \frac{i6\pi\omega_3^2\chi^{(3)}}{k_3c^2} [A_1(0)]^2 A_2(0) e^{i\Delta kz} e^{-N[2\sigma(\omega_1)+\sigma(\omega_2)]z/2} - \frac{\sigma(\omega_3)NA_3(z)}{2} \quad (2.1.18)$$

The integration of (2.1.18) with the assumption that the medium density stays constant over the whole length L and is zero outside the length, yields the following expression:

$$A_3(L) = \frac{i6\pi\omega_3^2L\chi^{(3)}}{k_3c^2} [A_1(0)]^2 A_2(0) \frac{e^{-\Gamma_3/2}}{(\Gamma_3 - \Gamma_i)/2 + i\Delta kL} (e^{[(\Gamma_3 - \Gamma_i)/2 + i\Delta kL] - 1}) \quad (2.1.19)$$

with $\Gamma_i = 2\Gamma_1 + \Gamma_2 = [2\sigma(\omega_1) + \sigma(\omega_2)]NL$ is the total optical depth of the medium at the incident frequencies and $\Gamma_3 = \Gamma(\omega_3)$ is the optical depth of the medium at the sum-frequency.

At the end of the medium the intensity of sum-frequency field is given by[6]:

$$I_i = \frac{n_i c}{2\pi} A_i A_i^* \quad (2.1.20)$$

Equation (2.1.20) allowed us to express the generated sum-frequency amplitude in terms of the incident intensities. We get

$$I_3(L) = \frac{144\pi^4 \omega_3^2}{n_1^2 n_2 n_3 c^4} L^2 |\chi^{(3)}|^2 [I_1(0)]^2 I_2(0) \times \frac{e^{-\Gamma_i} + e^{-\Gamma_3} - 2 \exp\left[\left(\frac{-\Gamma_3 - \Gamma_i}{2}\right)\right] \cos(\Delta k L)}{\left(\frac{-\Gamma_3 - \Gamma_i}{2}\right)^2 + (\Delta k L)^2} \quad (2.1.21)$$

Relation (2.1.21) can be rewritten as

$$I_3(L) = \frac{144\pi^4 \omega_3^2}{n_1^2 n_2 n_3 c^4} L^2 |\chi^{(3)}|^2 [I_1(0)]^2 I_2(0) F(\Delta k L, \Gamma_i, \Gamma_3) \quad (2.1.22)$$

where

$$F(\Delta k L, \Gamma_i, \Gamma_3) = \frac{\exp(-\Gamma_i) + \exp(-\Gamma_3) - 2 \exp\left[\left(\frac{-\Gamma_3 - \Gamma_i}{2}\right)\right] \cos(\Delta k L)}{\left(\frac{-\Gamma_3 - \Gamma_i}{2}\right)^2 + (\Delta k L)^2}. \quad (2.1.23)$$

$F(\Delta k L, \Gamma_i, \Gamma_3)$ is called phase matching factor and describes the effect of phase matching on the output of the sum-frequency wave.

The expression (2.1.22) is crucial for the experiment. Since it reveals factors that are indispensable in optimizing the sum-frequency generation. In fact, it can be seen that the intensity of sum-frequency can be optimized by :

- increasing the value of the susceptibility,
- increasing the value of the phase matching factor;
- in the case of the perfect phase matching, by increasing the medium length,
- increasing the incident intensities of beams.

All these optimization factors of the intensity of the generated sum-frequency wave will be discussed in the coming section.

2.2 Resonant enhancement

The value of susceptibility can be enhanced by resonances in order to generate high sum-frequency intensity.

Let us consider the expression of the third order susceptibility derived from the Schrödinger equation given in [6] [see equation (3.7.14), Page 146]

$$\begin{aligned}
 \chi_{kjih}^{(3)}(\omega_p + \omega_q + \omega_r, \omega_p, \omega_q, \omega_r) &= \frac{N}{\hbar^3} P_I \sum_{gmnv} \rho_{gg}^0 \\
 &\left[\frac{\mu_{gv}^k \mu_{vn}^j \mu_{nm}^i \mu_{mg}^h}{[(\omega_{vg} - \omega_p - \omega_q - \omega_r) - i\gamma_{vg}] [(\omega_{ng} - \omega_p - \omega_q) - i\gamma_{ng}] [(\omega_{mg} - \omega_p) - i\gamma_{mg}]} \right. \\
 &+ \frac{\mu_{gv}^h \mu_{vn}^k \mu_{nm}^j \mu_{mg}^i}{[(\omega_{nv} - \omega_p - \omega_q - \omega_r) - i\gamma_{nv}] [(\omega_{mv} - \omega_p - \omega_q) - i\gamma_{mv}] [(\omega_{vg} + \omega_p) + i\gamma_{vg}]} \\
 &+ \frac{\mu_{gv}^i \mu_{vn}^k \mu_{nm}^j \mu_{mg}^h}{[(\omega_{nv} - \omega_p - \omega_q - \omega_r) - i\gamma_{nv}] [(\omega_{vm} + \omega_p + \omega_q) + i\gamma_{vm}] [(\omega_{ml} - \omega_p) - i\gamma_{mg}]} \\
 &+ \frac{\mu_{gv}^h \mu_{vn}^i \mu_{nm}^k \mu_{mg}^j}{[(\omega_{mv} - \omega_p - \omega_q - \omega_r) - i\gamma_{mv}] [(\omega_{ng} + \omega_p + \omega_q) + i\gamma_{ng}] [(\omega_{vg} + \omega_p) + i\gamma_{vg}]} \\
 &+ \frac{\mu_{gv}^j \mu_{vn}^k \mu_{nm}^i \mu_{mg}^h}{[(\omega_{vn} + \omega_p + \omega_q + \omega_r) + i\gamma_{vn}] [(\omega_{mv} - \omega_p - \omega_q) - i\gamma_{mv}] [(\omega_{vg} - \omega_p) - i\gamma_{vg}]} \\
 &+ \frac{\mu_{gv}^h \mu_{vn}^j \mu_{nm}^k \mu_{mg}^i}{[(\omega_{nm} + \omega_p + \omega_q + \omega_r) + i\gamma_{nm}] [(\omega_{ng} - \omega_p - \omega_q) - i\gamma_{ng}] [(\omega_{mg} + \omega_p) + i\gamma_{mg}]} \\
 &+ \frac{\mu_{gv}^i \mu_{vn}^j \mu_{nm}^k \mu_{mg}^h}{[(\omega_{nm} + \omega_p + \omega_q + \omega_r) + i\gamma_{nm}] [(\omega_{vm} + \omega_p + \omega_q) + i\gamma_{vm}] [(\omega_{mg} - \omega_p) - i\gamma_{mg}]} \\
 &\left. + \frac{\mu_{gv}^h \mu_{vn}^i \mu_{nm}^j \mu_{mg}^k}{[(\omega_{mg} + \omega_p + \omega_q + \omega_r) + i\gamma_{mg}] [(\omega_{ng} + \omega_p + \omega_q) + i\gamma_{ng}] [(\omega_{vg} + \omega_p) + i\gamma_{vg}]} \right] \quad (2.2.1)
 \end{aligned}$$

where P_I is the internal permutation operator.

In the above expression of the third order susceptibility, seven last terms are often neglected since their contribution to the susceptibility are much smaller than the first term when resonances are considered.

If the ground state has much higher population than excited states then $\rho_{gg} \approx 1$ for the ground state and $\rho_{gg} \approx 0$ for the excited states. So, sum over g gives only one term. Experimentally the temperature in the heat pipe oven is approximately 760 degree Celsius. At this temperature most of the magnesium atoms in the medium are in their lowest atomic

level state (level g). The expression (2.2.1) can be written now as:

$$\chi_{kjih}^{(3)}(\omega_p + \omega_q + \omega_r, \omega_p, \omega_q, \omega_r) = \frac{N}{\hbar^3} P_I \sum_{mnp} \left[\frac{\mu_{gv}^k \mu_{vn}^j \mu_{nm}^i \mu_{mg}^h}{[(\omega_{vg} - \omega_p - \omega_q - \omega_r) - i\gamma_{vg}] [(\omega_{ng} - \omega_p - \omega_q) - i\gamma_{ng}] [(\omega_{mg} - \omega_p) - i\gamma_{mg}]} \right] \quad (2.2.2)$$

It can be seen clearly that the susceptibility of sum frequency generation can be enhanced by minimizing the denominator of equation (2.2.1). This can be realized by turning the incident waves sufficiently close to the resonance.

The diagrams below, provides different possibilities which can be used for resonant enhancement. Namely one-photon resonance, two-photon resonance and a three-photon resonance.

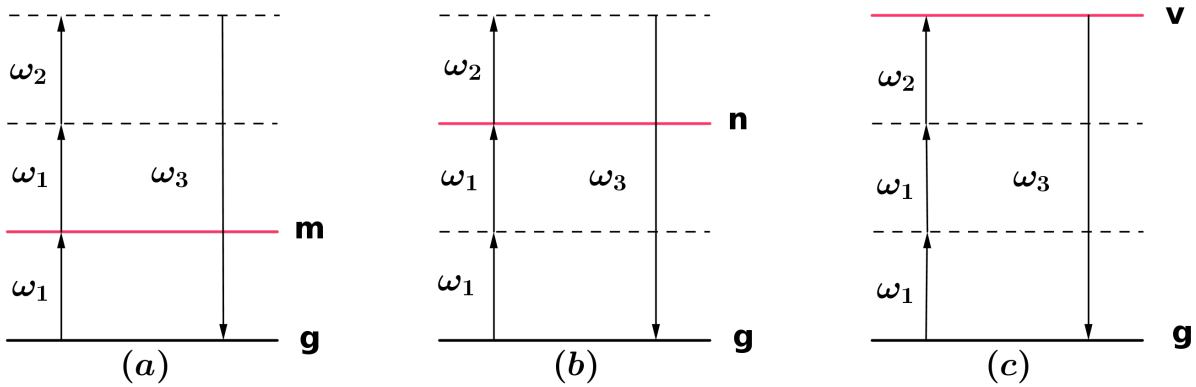


Figure 2.2: Diagrams illustrating the resonances that enhance the sum-frequency generation process. (a) One-photon resonance, (b) Two-photon resonance, and (c) Three-photon resonance.

The susceptibility for sum-frequency generation can be enhanced by these three processes. However, one-photon and three photon resonance are not helpful, because one photon resonance causes a strong absorption of the incident waves and in the case of three-photon resonance the generated wave is absorbed. Thus, the sum-frequency generation is enhanced by two-photon resonance which cause less attenuation in the signal. This two-photon resonance is obtained by adjusting the wave frequencies to the position where the double of the incident frequency equals to the resonance frequency of suitable transition, i.e $2\omega_1 = \omega_{ng}$.

Moreover, by considering the two-photon resonance with a specific state n , we can also neglect the sum over different states labelled n . Therefore, the susceptibility for sum-frequency generation becomes now:

$$\chi_{kjih}^{(3)}(\omega_3, \omega_1, \omega_1, \omega_2) = P_I \frac{N}{\hbar^3} \frac{1}{[(\omega_{ng} + 2\omega_1) - i\gamma_{ng}]} \sum_v \frac{\mu_{gv}^k(\omega_3) \mu_{vn}^j(\omega_2)}{[(\omega_{vg} + 2\omega_1 + \omega_2) - i\gamma_{vg}]} \sum_m \frac{\mu_{nm}^i(\omega_1) \mu_{mg}^h(\omega_1)}{[(\omega_{mg} + \omega_1) - i\gamma_{mg}]} \quad (2.2.3)$$

Note that the process of enhancement of sum-frequency susceptibility by two-photon resonance optimizes also the other competing processes, such as difference-frequency generation ($\omega_{diff} = 2\omega_1 - \omega_2$) and third harmonic generation ($\omega_{Th} = 3\omega_1$).

2.3 Phase matching

Phase matching is utilized for discriminating against other competing processes in the medium, as well as its contribution to the improvement of the intensity of the generated field at the frequency $\omega_3 = 2\omega_1 + \omega_2$ in a two component gaseous nonlinear medium.

Looking at the expression (2.1.22), one can see that the intensity of the generated sum-frequency wave can be improve by increasing the value of phase matching factor. This can only be achieved when the wave vector mismatch $\Delta k = 0$, which is the condition of perfect phase matching [6].

Furthermore, this requirement corresponds to the conservation laws of the linear momentum. In the optical process

$$\vec{k}_i = \frac{1}{\hbar} \vec{p}_i \quad (2.3.1)$$

where \vec{p}_i is the linear momentum. Then

$$\Delta \vec{k} = \vec{k}_3 - \vec{k}_1 - \vec{k}_2 = 0$$

which implies that

$$\vec{k}_3 = \vec{k}_1 + \vec{k}_2 \implies \frac{1}{\hbar} \vec{p}_3 = \frac{1}{\hbar} \vec{p}_1 + \frac{1}{\hbar} \vec{p}_2$$

therefore,

$$\vec{p}_3 = \vec{p}_1 + \vec{p}_2. \quad (2.3.2)$$

Expression (2.3.2) is the conservation of linear momentum in which a new photon with the frequency ω_3 is generated by annihilation of two photons with the respectively frequencies ω_1 and ω_2 .

The minimum value of vector mismatch ($\Delta k = 0$) physically means that the ω_3 waves generated in different volume elements of the nonlinear medium interfere constructively, which is possible only when the fundamental and the generated waves have the same phase velocity.

The phase matching condition for sum-frequency generation in the case where the incident laser beams are collinear is given by

$$\Delta k = 0 = 2k_1 + k_2 - k_3$$

which means that the phase matching can be obtained when the following condition is satisfied.

$$\omega_3 n_3 = 2\omega_1 n_1 + \omega_2 n_2 \quad (2.3.3)$$

In practice there are different methods for achieving phase matching, see [5] for more information see:

In the experimental setup developed in the Laser Research Institute and used in this thesis for generating a tunable pulsed VUV laser light with a narrow spectral bandwidth, a two-component gas-vapour mixture is used as nonlinear medium. The first component is the magnesium vapour and exhibits anomalous dispersion while krypton, the second component, shows normal dispersion. The phase matching is obtained by adjusting the pressure of both gases in order to find the ratio where the indices of the mixture at ω_1, ω_2 and ω_3 satisfies equation (2.3.3).

The refractive index of the magnesium vapour (anomalous dispersion) is given by:

$$n_A(\omega_3) < n_A(\omega_1), n_A(\omega_2). \quad (2.3.4)$$

For krypton gas (normal dispersion), its refractive index is given by:

$$n_B(\omega_3) > n_B(\omega_1), n_B(\omega_2), \quad (2.3.5)$$

where A and B represent magnesium vapour and krypton gas, respectively. The indices of refraction of the gas mixture at frequencies ω_1, ω_2 and ω_3 are given [5] by the following expressions :

$$n_{mixture}(\omega_1) = 1 + 2\pi [2N_A\alpha_A^1(\omega_1) + 2N_B\alpha_B^1(\omega_1)] \quad (2.3.6)$$

$$n_{mixture}(\omega_2) = 1 + 2\pi [N_A\alpha_A^2(\omega_2) + N_B\alpha_B^2(\omega_2)] \quad (2.3.7)$$

$$n_{mixture}(\omega_3) = 1 + 2\pi [N_A\alpha_A^3(\omega_3) + N_B\alpha_B^3(\omega_3)] \quad (2.3.8)$$

where N_A and N_B are the gas densities, and $\alpha'_x(\omega_i)$ is the atomic polarisability of gas x' at frequency ω_i .

For obtaining phase matching in the case of sum-frequency generation, the following condition is required (following from expression 2.3.3):

$$\omega_3 n_{mixture}(\omega_3) = 2\omega_1 n_{mixture}(\omega_1) + \omega_2 n_{mixture}(\omega_2) \quad (2.3.9)$$

Replacing different components of equation (2.3.9) by their expressions obtained in equations 2.3.6, 2.3.7 and 2.3.8, we get:

$$\begin{aligned} \omega_3 [N_A\alpha_A^3(\omega_3) + N_B\alpha_B^3(\omega_3)] &= \omega_1 [2N_A\alpha_A^1(\omega_1) + 2N_B\alpha_B^1(\omega_1)] \\ &\quad + \omega_2 [N_A\alpha_A^2(\omega_2) + N_B\alpha_B^2(\omega_2)] \\ N_A [\omega_3\alpha_A^3(\omega_3) - 2\omega_1\alpha_A^1(\omega_1) - \omega_2\alpha_A^2(\omega_2)] &= N_B [2\omega_1\alpha_B^1(\omega_1) + \omega_2\alpha_B^2(\omega_2) \\ &\quad - \omega_3\alpha_B^3(\omega_3)] \\ \implies \frac{N_A}{N_B} &= \frac{[2\omega_1\alpha_B^1(\omega_1) + \omega_2\alpha_B^2(\omega_2) - \omega_3\alpha_B^3(\omega_3)]}{[\omega_3\alpha_A^3(\omega_3) - 2\omega_1\alpha_A^1(\omega_1) - \omega_2\alpha_A^2(\omega_2)]} \end{aligned} \quad (2.3.10)$$

Equation(2.3.10) shows that it is the density ratio (or pressure ratio) of Mg vapour and Kr gas that has to be adjusted to achieve phase matching. As the atomic polarisabilities are frequency dependent, the pressure ratio for phase matching is also frequency dependent. Equation (2.3.10) represents a condition that must be satisfied over the whole path length of the laser beam in the gaseous medium that requires a high homogeneous medium. In the experiment the homogeneity of magnesium vapour krypton gas mixture is achieved by using a heat pipe oven.

Phase matching the medium for sum-frequency generation also helps to suppress the difference-frequency generation ($\omega_{diff} = 2\omega_1 - \omega_2$). However, the third-harmonic generation is not suppressed much because the condition for phase matching of sum-frequency and third-harmonic are very similar.

2.4 Beam polarisation

Third harmonic generation in the medium can be suppressed by the polarisation of the incident beams to leave the sum-frequency generation as the dominant process.

Utilization of beam polarisation for suppressing the third harmonic generation is based on the quantum mechanical angular momentum conservation principle. In the numerator of equation (2.2.3), $\mu_{xy}^l(\omega_i)$ represents the electric dipole moment, which is given by $\mu_{xy}^l(\omega_i) = \langle \psi_x | \hat{\mu}^l(\omega_i) | \psi_y \rangle$, where l is the orientation of the polarisation producing the dipole transition. ψ_x and ψ_y are respectively the energy states of the magnesium atoms characterised by the magnetic quantum numbers m_x and m_y .

Applying the Wigner-Eckart theorem of the quantum mechanics to this magnetic quantum numbers obtained in the equation (2.2.3), gives the following selection rule [5]:

$$\Delta m_1 + \Delta m_1 + \Delta m_2 + \Delta m_3 = 0 \quad (2.4.1)$$

where Δm_i represents the change in the magnetic quantum number related to the electric dipole moment operator $\hat{\mu}^l(\omega_i)$.

When the incident beams are perfectly circular polarised, this selection rule (2.4.1) allows only the sum-frequency generation to take place in the medium. When a laser beam at the frequency ω_i is circularly polarised, the change in magnetic quantum number that it can produce is $\Delta m_i = \pm 1$, where the sign depends on the direction of the rotation of the electric field. Therefore, by polarizing the incident beams in the such a way that ω_1 is clockwise circularly polarised ($\Delta m_1 = +1$) and ω_2 is anti-clockwise circularly polarised ($\Delta m_2 = -1$), the condition (2.4.1) will be satisfied and the generated wave will also be circularly polarised with $\Delta m_3 = -1$.

The third harmonic generation process can not take place in the medium when the incident beams have a circular polarisation, since the condition for third harmonic generation at the frequency $3\omega_1$ is

$$3\Delta m_1 + \Delta m_3 = 0. \quad (2.4.2)$$

This can only be satisfied for $\Delta m_3 = \pm 3$ which is physically impossible. This is because, according to the quantum mechanics, a photon cannot carry an angular momentum larger than 1.

Perfect circularly polarisation (in opposite rotational directions) of incident beams suppress the third harmonic generation in the medium and makes the sum-frequency as the dominant process.

Chapter 3

Principles of a grating monochromator

Monochromator is the most common optical device used in the emission and absorption spectroscopy . It is usually constituted with an entrance slit, collimator mirror, a diffraction grating and an exit slit. Furthermore, its efficiency is based on the dispersion and the resolving power of its grating. In this section, an overview of these spectroscopy quantities are provided.

3.1 Grating theory

Consider an incident beam of the white light striking a grating surface at point B as shown in figure 3.1. This beam will be diffracted along different discrete paths and different directions [7]. The relationship between the incident angle, the diffracted angle and the diffracted wavelength is given by the grating equation [8].

$$m\lambda = d(\sin \alpha + \sin \beta), \quad (3.1.1)$$

where m is the diffraction order, λ represents the diffracted wavelength and d is the groove spacing of the grating. α and β are the incident and the diffracted angles respectively. α is considered to be positive and β negative angle as α and β are on opposite sides of the grating normal.

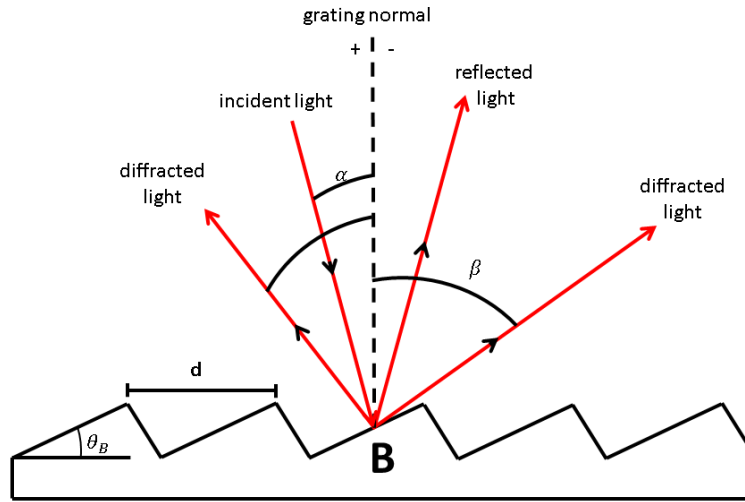


Figure 3.1: Illustration of diffraction by a plane grating.

Expression 3.1.1 is crucial in the characterisation of a monochromator since most of the useful spectroscopy quantities, such as dispersion and resolving power are derived from it.

The dispersion of a monochromator can be defined as its capability to separate different wavelengths present in the light from the source [8]. Dispersion can be quantified as angular dispersion or linear dispersion.

The differentiation of the grating equation with respect to the wavelength by assuming the incident angle α is constant leads to the following expression for the angular dispersion D :

$$D = \frac{d\beta}{d\lambda} = \frac{m}{d \cos \beta} = \frac{m}{d} \sec \beta. \quad (3.1.2)$$

Considering the groove frequency G with $G = \frac{1}{d}$, equation (3.1.2) becomes:

$$D = \frac{d\beta}{d\lambda} = Gm \sec \beta. \quad (3.1.3)$$

The angular dispersion D represents the change of the diffraction angle per unit wavelength. One can notice that for a given wavelength λ , the angular dispersion depends only on the incident and diffracted angles. This can be visualized by its general form which is obtained

by the substituting the expression of m from the grating equation (3.1.1) in the equation (3.1.3).

$$D = \frac{d\beta}{d\lambda} = \frac{\sin \alpha + \sin \beta}{\lambda \cos \beta} \quad (3.1.4)$$

The linear dispersion can be defined as the measure of the change of the linear distance L along the image plane of the monochromator with the wavelength as illustrated in Figure 3.2.

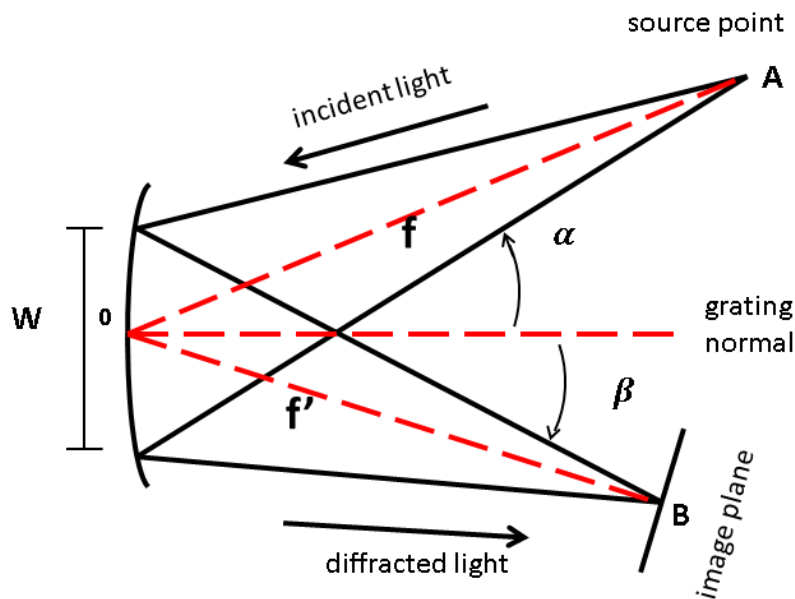


Figure 3.2: Sketch of the optical path length of a monochromator.

In other word, it is the product of the angular dispersion D and the effective focal length f' :

$$\frac{dL}{d\lambda} = f' \times \frac{d\beta}{d\lambda} = \frac{mf'}{d \cos \beta} \quad (3.1.5)$$

where f' is the focal length of the focusing element.

In practice, the linear dispersion is preferred because it is more convenient to use a linear scale than an angular scale. The inverse of the linear dispersion, called reciprocal dispersion, is usually expressed in nm/mm [7]

$$P = \frac{d\lambda}{dL} = \frac{d \cos \beta}{m f'} \quad (3.1.6)$$

where P is the reciprocal linear dispersion and shows the change in the wavelength corresponding to a change in location along the focal plane.

It is important to notice that the validity of equations (3.1.5) and (3.1.6) is limited to the case where the angle between the focal plane and the diffracted ray is 90 degrees. Otherwise, they should be multiplied by the so called obliquity factor which is given by:

$$F = \frac{1}{\sin \theta}, \quad (3.1.7)$$

where θ is the angle between the focal plane and the diffracted light. Therefore, the general equation of the reciprocal linear dispersion is given by the following equation:

$$P = F \times \frac{d \cos \beta}{m f'}. \quad (3.1.8)$$

3.1.1 Resolving power

The resolving power is a dimensionless quantity which measure the ability of a grating to separate adjacent spectral lines. Considering two neighbouring wavelengths λ and $\lambda + \Delta\lambda$ that still allows the two lines to be resolved, the resolving power R is simply the the ratio:

$$R = \frac{\lambda}{\Delta\lambda}. \quad (3.1.9)$$

Here $\Delta\lambda$ is the smallest difference in wavelength between two adjacent spectral lines that can be distinguished. It is called the limit of the resolution.

The theoretical limit of the resolving power can also be obtained theoretically under the assumption that the slits are very narrow by the product of the diffraction order m and the total number of grooves N illuminated on the surface of the grating.

$$R = mN \quad (3.1.10)$$

The substitution of the expression of the diffraction order m in the equation (3.1.10) yields another form of the resolving power.

$$R = \frac{Nd(\sin \alpha + \sin \beta)}{\lambda} \quad (3.1.11)$$

The quantity Nd can be replaced by the illuminated width W of the grating in the case where the groove spacing d is uniform over the surface of the grating. This leads to another equation, which shows that for a given wavelength λ , the resolving power is also dependent on the incident and refracted angles.

$$R = \frac{W(\sin \alpha + \sin \beta)}{\lambda} \quad (3.1.12)$$

It is important to emphasize that the experimental resolving power does not only depend on the incident and refracted angles. Other parameters, such as the slits width, the uniformity of the grating and the quality of associated optics can also affect the resolution power of a grating [7].

3.1.2 The spectral bandpass

The spectral bandpass of a monochromator can be defined as the wavelengths range of light that passes through the exit slit [7]. For a given optical system, where the entrance slit is in theory infinitely small and in practice much smaller than the exit slit the spectral bandpass B can be estimated by the product of the reciprocal linear dispersion P and the exit slit width W' .

$$B \approx P \times W' \quad (3.1.13)$$

So, the spectral bandpass is not a property of the diffraction grating itself but a property of the spectroscopic system [7].

3.1.3 Stray and Scattered light

It has been shown that the grating equation (3.1.1) governs the diffraction of the light in the spectroscopic system and the grating diffracts light in such a way that for a particular angle of the grating only a specific wavelength can pass through the exit slit and reach the detector.

In practice there are often stray and scattered light which may also reach the detector. Stray light is defined as all light other than the wavelength of interest that reaches the detector from anywhere other than the grating itself. While the scattered light is simply unwanted light originating from the grating itself.

Stray and scattered light are usually produced by the imperfections in the shape and spacing of the grooves and roughness on the surface of the grating [7]. Moreover, the higher-order light diffraction (any order other than the primary diffraction order of use) contributes also to the stray light [9].

This unwanted light is a background signal that has to be taken into account when absorption spectroscopy are done.

Chapter 4

Literature study on VUV spectroscopy of CaF_2 crystals

4.1 Properties of CaF_2 crystals

The calcium fluoride crystal has a cubic face-centered crystal structure wherein the Ca^{2+} ions occupy the vertices and centers of the cube faces [10, 11]. Atoms are arranged so that each Ca^{2+} ion is linked to eight F^- ion [12], occupying the vertices of a cube. Each F^- ion is surrounded by four Ca^{2+} ions occupying the vertices of a tetrahedron. The crystal lattice structure of Ca^{2+} is illustrated in Figure 4.1 [13].

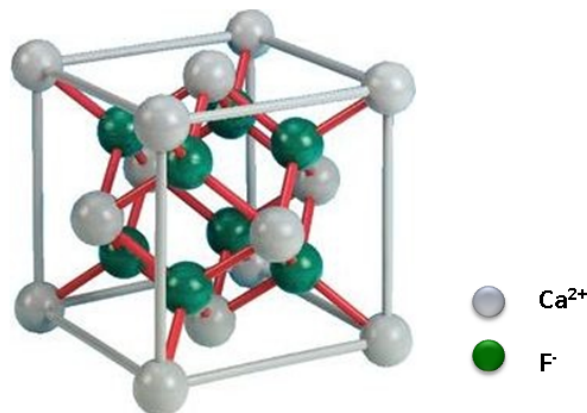


Figure 4.1: *The crystal lattice structure of Calcium Fluoride.*

Excellent transmission of crystalline calcium fluoride in the ultraviolet (UV) and vacuum ultraviolet (VUV) range [3] and its wide band gap of about 12 eV (103 nm) place it among the most important materials for optics for laser applications in the UV [1, 2]. In addition,

calcium fluoride has a high thermal conductivity which gives it an advantage when used for high power laser optics [2]. Due to its cubic crystalline structure, calcium fluoride can be doped with rare earth elements, such as Nd³⁺ and Yb³⁺ [14].

A disadvantage of CaF₂ as optical material is that it suffers from decreasing of transmission under prolonged high power UV irradiation [1, 15]. This is seen for example at 193 nm where the visible coloration in a CaF₂ sample of high purity has been observed after prolonged ArF laser irradiation [15]. However, it has been reported that the highest purity CaF₂ samples show the lowest absorption coefficients values compared to the values of samples containing impurities. The experiment has shown that the fast degradation in the calcium fluoride upon high laser irradiation are related to impurities in CaF₂ crystals [1, 15].

Furthermore, it is found that the degradation is temperature dependent. This was experimentally observed by Mühlig et al. [1]. The results of their experiment show that the fluorescence intensity associated with Na defects (M_{Na} centres) was double for the sample heated to 80 K compared to its room temperature value, and it almost vanished when the sample was cooled to 20 K below room temperature.

Exact knowledge of the influence of impurities or defects on the durability of calcium fluoride is very important for optical applications. [1, 15, 2].

4.2 Steady state spectra of pure and doped CaF₂

Due to its internal structure, the virgin (non-irradiated) crystalline calcium fluoride has two main defects, which are commonly called intrinsic defects: F centers and M centers. F center means a fluorine vacancy occupied by an electron and M center is the agglomeration of two F centers. Both intrinsic defects are very unstable at room temperature [1] and can only be stabilized when they are in the presence of some impurity such as an alkaline metal or oxygen. These defects thus formed by the F and M centers combined with metal alkaline (or oxygen) are characterized by their absorption and fluorescence spectra. It is the case of F_{Na} and M_{Na} , which are the F and M centers respectively, stabilized by sodium (Na). F_{Na} and M_{Na} are characterized by an absorption band around 322, 385, 600 nm and show a fluorescence at 740 nm when excited with 193 nm [1, 2].

It has been reported by several authors [16, 11] that even the so-called pure calcium fluoride crystal contains impurities such as: Al³⁺, Si³⁺, Y³⁺ and O²⁻. These impurities are in order of p.p.m but still cause absorption and affects the durability of the material. Oboth et

al [17] reported that the CaF_2 samples doped by Pb^{2+} show strong absorption bands (so-called A and B) at 204.5 nm (6.08 eV) and 154.4 nm (8.05 eV), and a small absorption band (Band C) at 165.1 (7.53 eV). However, the CaF_2 samples doped by Bi^{3+} , show double structures at 213.6 nm (5.82 eV) and 200.8 (6.19 eV) which were attributed to the A band. Another structure was found at 135 nm (9.17 eV) and was interpreted as D band.

Sastry and Kennedy [18] also observed several optical absorption bands in the $D_y : \text{Pb} : \text{CaF}_2$ single crystal respectively at 718.6, 453.7, 268.5, 260.6 and 241.4 nm. These bands were attributed to D_y^{2+} absorption. According to these authors, D_y^{2+} absorption in the UV region is due to $4f^{10} \rightarrow 4f^9 5d$. Other absorption bands were observed by Kaczmarek et al. [11] at 360, 315, 271, 260, 227 and 214 nm in Y^{3+} doped CaF_2 samples which were heated in hydrogen gas at 1323 K for one hour. Those band structures were attributed to Y^{2+} as well as to Y^{2+} -associated centres and were also observed by many researchers in diverse host materials [11].

In their study of some optical and dielectric properties of PbF_2 -doped and x-ray irradiated CaF_2 crystals, Nicoara et al. [19, 20] found that PbF_2 -doped CaF_2 crystals had peaks only in the UV region, respectively at 306, 243, 205 and 215 nm. These absorption bands were attributed to Pb^{2+} . However some other bands structure at 375, 402 510 and 771 nm appeared after 1 hour X-ray irradiation. These authors attributed the band at 771 nm to the diverse aggregate types centres, for example $\text{Pb}^+(1) - \text{Pb}^{2+}$, since it was also observed in PbF_2 -doped SrF_2 [21].

Its worth mentioning that most of the spectroscopy studies of calcium fluoride in the UV range were performed using discharge lamps.

4.3 Pulsed laser spectroscopy of CaF_2

Transmission and laser induced fluorescence measurements performed with nanosecond (ns) and femtosecond (fs) pulses of similar wavelength allowed to investigate the influence of M_{Na} centers on the absorption of CaF_2 crystals [1, 2]. Different results regarding the two-photon absorption (TPA) coefficient were obtained depending on whether the sample was irradiated by nanosecond or femtosecond pulses. The two-photon absorption coefficients obtained with the nanosecond pulses shows an increase when the sodium concentration increases while the one obtained with femtosecond pulses is not a function of the Na concentration [1, 2]. It was also found that the constant two-photon absorption coefficient in high purity CaF_2 samples obtained with femtosecond pulses was approximately 1/3 of the lowest two-photon absorption coefficient obtained with the nanosecond pulses [2].

In order to find a physical reason about the two-photon absorption behaviour observed in CaF_2 doped Na, an experiment was carried out by Karras et al. [15] for determining the fast non-radiative transitions between the highly excited M_{Na}^{**} states to the fluorescent M_{Na}^* state in CaF_2 . This is achieved by using Laser-Induced Fluorescence (LIF) together with fs Laser-Induced Depletion technique (LID). This method consists of pumping the M_{Na}^{**} state with 2^{nd} (392 nm) or 3^{rd} (262 nm) harmonics. Thereafter, the fundamental fs laser pulses (785 nm) is used at variable delay times relative to the UV laser pulses to deplete the fluorescence M_{Na}^* state.

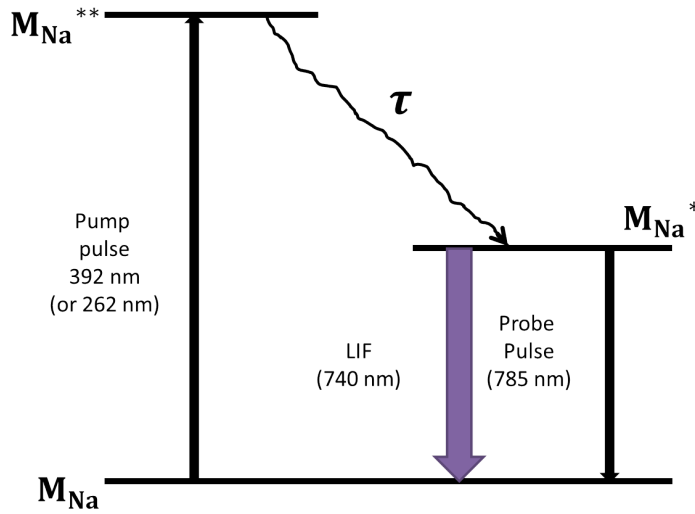


Figure 4.2: Illustration of the optical excitation and the non-radiative and fluorescing (LIF) relaxation pathways.

The related time constants for the excited state M_{Na}^{**} to the fluorescence state M_{Na}^* were 1.0 ± 0.14 ps and 3.0 ± 0.3 ps upon 2^{nd} and 3^{rd} harmonics excitation respectively [15].

From these relaxation rates, the two-photon absorption behaviour in CaF_2 samples obtained with ArF ns laser pulses and UV fs laser pulses can be understood.

For nanosecond pulses, the M_{Na} centers can be excited by a single photon absorption into the M_{Na}^{**} states. Due to the fact that the non-radiative relaxation (1.0 ± 0.14 ps or 3.0 ± 0.3 ps) is fast compare to the pulse duration, the M_{Na}^{**} state can decay to the fluorescence state M_{Na}^* within the same laser pulse and then the M_{Na}^* can be also excited within the same laser pulse [15, 14]. The single photon absorption here has the same characteristic as the two-photon absorption therefore affect the two-absorption coefficients. However this cannot be the case for a femtosecond laser pulses, since its shorter compare to the non-radiative relaxation and then the fluorescence state M_{Na}^* cannot be excited by the laser

pulse. Therefore, the M_{Na} do not affect the two-photon absorption coefficients recorded with a femtosecond pulses [14].

These results lead to the development of the model for M_{Na} center formation and annealing in CaF_2 .

4.4 Model of M_{Na} center formation and annealing

In this section we review the results as well as the model for generation and annealing of the M_{Na} center obtained by Mühlig et al published in [1, 2] in order to understand the generation and the annealing of the M_{Na} center of calcium fluoride. In this work, we have written it out completely showing all calculations of the model that were not shown in [1, 2].

This is relevant in our study because sodium is a common impurity in calcium fluoride, present in high purity commercial samples and it serves as an example of how self trapped exciton leads to permanent defects. The model has been developed to describe the generation and the annealing of defects by ArF laser light (193 nm, pulse duration 30 ns and repetition rate 60 Hz) and the fourth harmonic of Ti Sa laser (197 nm, 350 fs pulse duration, repetition rate 50 Hz) [1, 2]. The model is illustrated in Figure 4.3.

The generation and annealing of M_{Na} centers can be treated separately, due to the fact that the generation of M_{Na} center occurs within the dark period between the ArF laser pulses while annealing of M_{Na} center takes place during the laser duration.

4.4.1 Generation of self trapped excitations (STE's)

Calcium fluoride sample contains Na^+ and initial densities of F_{Na} and M_{Na} centers from its production. The CaF_2 will make a transition to CaF_2^{**} , a highly excited state in the conduction band, after being irradiated by ArF laser pulse. Due to the wide band gap of CaF_2 , that transition process can only be achieved by intrinsic two-photon absorption.

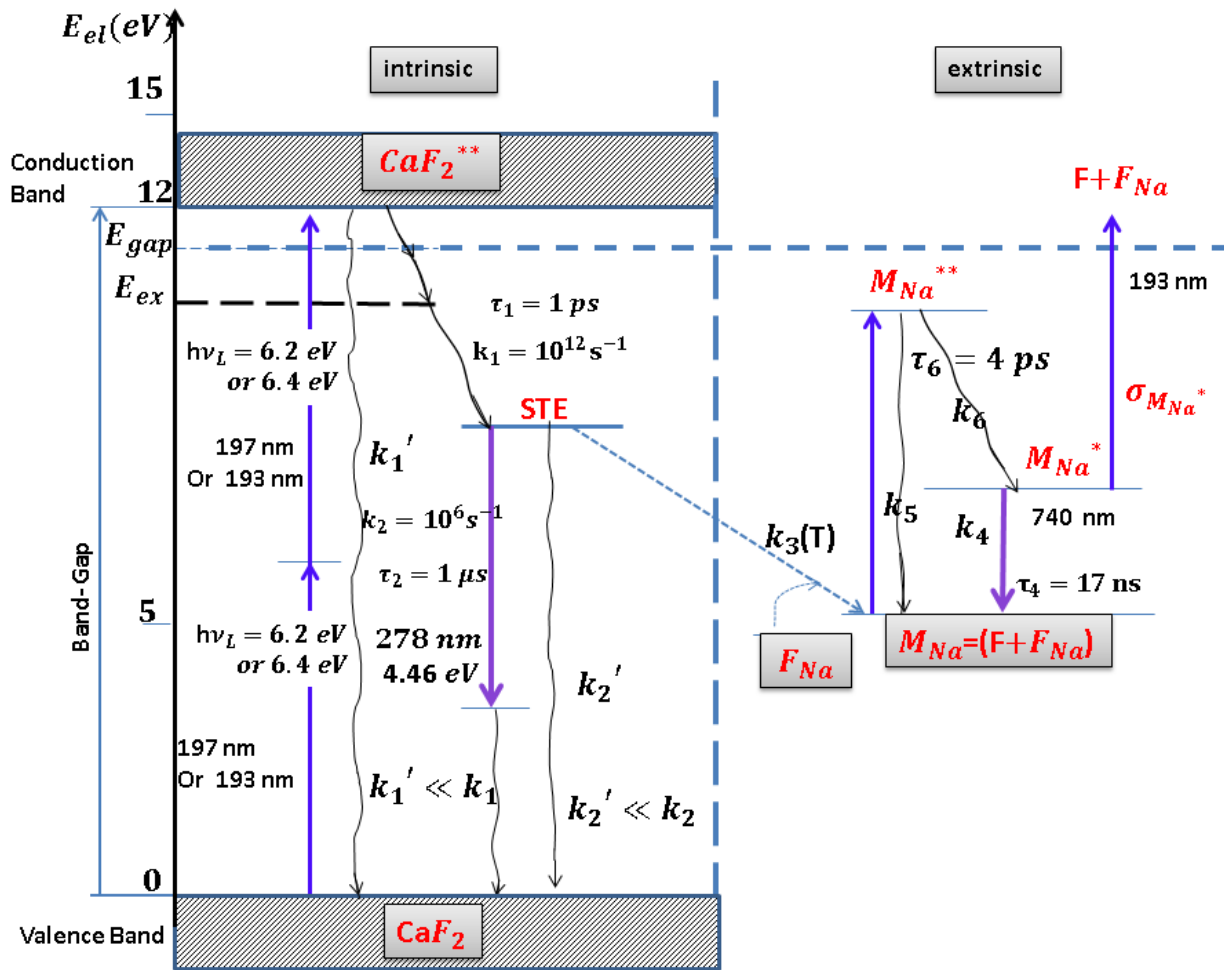


Figure 4.3: Diagram of laser induced generation and annealing of M_{Na} centers in CaF_2 [1].

CaF_2 transition from a ground state to a highly excited state causes generation of free pairs of electrons and holes. The created excitons, pairs of H and F centers, will relax into the mobile exciton state at E_{ex} , before forming the STE by the rate constant $k_1 = 10^{12} s^{-1}$.

Self trapped exciton is described as a bound electron-hole pair involving a strong coupling of electron or hole into a crystal lattice.

Due to the relative inefficient electron-phonon coupling for the large energy gap of calcium fluoride (11.5-12.1eV), the chance of electron returning to ground state by converting its electron energy to vibrational energy of crystal lattice is small. Thus, most of the excitons do form STE's and the remaining will directly decay to the ground states ($k_1' \ll k_1$).

The STE relaxation is performed by three following processes:

- The first relaxation process k'_2 is considered as the purely radiationless deactivation of the STE to the CaF_2 ground state. It is assumed to be negligible due fact that $k'_2 \ll k_2$.
- The second radiationless process $k_3(T) [F_{Na}]$ is the one in which the M_N generation comes from. This process occurs after the thermal activation ($E_a = 0.4\text{eV}$ [1]) that causes the dissociation of F and H centers. Thereafter, F center can combine with F_{Na} and form M_{Na} center, by $F + F_{Na} \longrightarrow M_{Na}$.
- The third STE relaxation process k_2 takes place by the photon emission at 278 nm, 4.46 eV $k_2 = 10^6\text{s}^{-1}$ [1]. This emission is followed by a radiationless deactivation to the ground state.

The sum of all these above relaxation processes gives the STE relaxation which is expressed by the following equation:

$$k_{\text{STE}} = k_2 + k'_2 + k_3(T) [F_{Na}].$$

Considering the rate constant value of STE formation $k_1 = 10^{12}\text{s}^{-1}$ ($\tau_1 = 1\text{ps}$) and the laser pulse duration which is approximately 30 ns $\tau_L \approx 30\text{ ns}$, it is clear that the STE generation takes place essentially during the laser pulse only. The density of the STE's at the end of a laser pulse is calculated by the following rate equation:

$$[\text{STE}] (\tau) = \sigma^{(2)} [\text{CaF}_2] I^2 \tau_L \quad (4.4.1)$$

In the (4.4.1), $\sigma^{(2)}$ represent two photon absorption cross section, I is the intensity of the laser irradiation and τ_L is the laser pulse duration.

4.4.2 Generation of M_{Na} centers

The M_{Na} generation takes place dominantly in the dark period τ_{dp} between the laser pulses [valid for $\tau_{dp} > 1/k_2$; i.e up to repetition rates of 100 kHz]. Consequently, the change of $[\text{STE}] (t)$ and $[M_{Na}] (t)$ within τ_{dp} are given by the following rate equations:

$$\frac{d[\text{STE}] (t)}{dt} = - (k_2 + k_3(T) [F_{Na}]) [\text{STE}] (t) \quad (4.4.2)$$

$$\frac{d[M_{Na}] (t)}{dt} = k_3(T) [F_{Na}] [\text{STE}] (t) \quad (4.4.3)$$

Equation (4.4.2) can be rearranged as follows:

$$\frac{d[\text{STE}](t)}{[\text{STE}](t)} = -(k_2 + k_3(T) [F_{Na}]) dt \quad (4.4.4)$$

In the case of high initial F_{Na} center concentrations, we are assuming that any change that may have occurred in F_{Na} during the formation of M_{Na} center is negligible, which means that F_{Na} is constant ($[F_{Na}] = [F_{Na}]_{initial}$).

Equation (4.4.4) can now be integrated from τ_L to t , due to the fact that the STE generation takes place only during the laser pulses. Therefore:

$$\begin{aligned} \int_{\tau_L}^t \frac{d[\text{STE}](t)}{[\text{STE}](t)} &= - \int_{\tau_L}^t (k_2 + k_3(T) [F_{Na}]) dt \\ \ln [\text{STE}](t) - \ln [\text{STE}](\tau_L) &= -(k_2 + k_3(T) [F_{Na}]) (t - \tau_L) \\ \ln \left(\frac{[\text{STE}](t)}{[\text{STE}](\tau_L)} \right) &= -(k_2 + k_3(T) [F_{Na}]) (t - \tau_L) \\ [\text{STE}](t) &= [\text{STE}](\tau_L) e^{-(k_2 + k_3(T) [F_{Na}]) (t - \tau_L)} \end{aligned} \quad (4.4.5)$$

Equation (4.4.5) express the STE density at the end of the laser pulse.

By replacing the expression for $[\text{STE}]$ in (4.4.5) into the equation (4.4.3), we get:

$$\frac{d[M_{Na}](t)}{dt} = k_3(T) [F_{Na}] [\text{STE}](\tau_L) e^{-(k_2 + k_3(T) [F_{Na}]) (t - \tau_L)}. \quad (4.4.6)$$

Which implies:

$$d[M_{Na}](t) = k_3(T) [F_{Na}] [\text{STE}](\tau_L) e^{-(k_2 + k_3(T) [F_{Na}]) (t - \tau_L)} dt \quad (4.4.7)$$

Equation (4.4.7) can be integrated from τ_L to τ_{dp} , since the M_{Na} generation only takes place during the dark period between two laser pulses.

Therefore:

$$\int_{\tau_L}^{\tau_{dp}} d[M_{Na}](t) = \int_{\tau_L}^{\tau_{dp}} k_3(T) [F_{Na}] [STE](\tau_L) e^{-(k_2+k_3(T)[F_{Na}]) (t-\tau_L)} dt$$

$$\implies [M_{Na}](\tau_{dp}) - [M_{Na}](\tau_L) = k_3(T) [F_{Na}] [STE](\tau_L) \int_{\tau_L}^{\tau_{dp}} e^{-(k_2+k_3(T)[F_{Na}]) (t-\tau_L)} dt$$

When calculating the M_{Na} concentration that is generated during one laser pulse the second term of the left side in equation above is equal to zero, since at the begin of the laser pulse duration the STE density is assumed to be zero. Thus :

$$[M_{Na}](\tau_{dp}) = k_3(T) [F_{Na}] [STE](\tau_L) e^{(k_2+k_3(T)[F_{Na}]) (\tau_L)} \int_{\tau_L}^{\tau_{dp}} e^{-(k_2+k_3(T)[F_{Na}]) (t)} dt$$

$$= -\frac{k_3(T) [F_{Na}] [STE](\tau_L) e^{(k_2+k_3(T)[F_{Na}]) (\tau_L)}}{(k_2 + k_3(T) [F_{Na}])} \left[e^{-(k_2+k_3(T)[F_{Na}]) (\tau_{dp})} - e^{-(k_2+k_3(T)[F_{Na}]) (\tau_L)} \right]$$

$$[M_{Na}](\tau_{dp}) = -\frac{k_3(T) [F_{Na}] [STE](\tau_L)}{(k_2 + k_3(T) [F_{Na}])} \left[e^{(k_2+k_3(T)[F_{Na}]) (\tau_L)} e^{-(k_2+k_3(T)[F_{Na}]) (\tau_{dp})} - 1 \right] \quad (4.4.8)$$

Considering that $(k_2 + k_3(T) [F_{Na}]) \gg 1/\tau_{dp}$, we have $\exp[-(k_2 + k_3(T) [F_{Na}]) (\tau_{dp})] \approx 0$ in equation (4.4.8).

Hence :

$$[M_{Na}](\tau_{dp}) = \left(\frac{k_3(T) [F_{Na}]}{k_2 + k_3(T) [F_{Na}]} \right) \sigma^2 [CaF_2] I^2 \tau_L,$$

$$= \left(\frac{k_3(T) [F_{Na}]}{k_2 + k_3(T) [F_{Na}]} \right) [STE](\tau_L). \quad (4.4.9)$$

.

Equation (4.4.9) tell us about M_{Na} concentration generated within a single dark period τ_{dp} .

4.4.3 Annealing of M_{Na} centers

Dissociation of M_{Na} centers into pairs of F and F_{Na} centers is the mechanism for the annealing of M_{Na} defect centers. This dissociation is caused by two consecutive 1-photon absorption process during a single laser pulse.

During the first photon absorption, the M_{Na} will make a transition to an highly excited state M_{Na}^{**} . Thereafter the population of M_{Na}^{**} will relax rapidly to the fluorescence state

M_{Na}^* via k_6 ($\frac{1}{k_6} = \tau_6 = 4\text{ps}$) and the remaining part will decay to the M_{Na} ground state via k_5 .

Depopulation of M_{Na}^* state is made via the fluorescence emission at 740 nm ($\tau_{fl} = \frac{1}{k_4} = 17\text{ ns}$) or by the second one photon absorption which will lead the dissociation of F and F_{Na} .

Therefore the M_{Na} annealing takes place during the laser pulse. The following equations are the associated simplified rate equations for laser pulse number N:

$$d[M_{Na}](t)/dt \approx 0, \quad (4.4.10)$$

$$d[M_{Na}^{**}](t)/dt = \sigma_{M_{Na}} [M_{Na}]_N(0) I - (k_5 + k_6) [M_{Na}^{**}](t), \quad (4.4.11)$$

$$d[M_{Na}^*]/dt = k_6 [M_{Na}^{**}](t) - (k_4 + \sigma_{M_{Na}}^* I) [M_{Na}^*](t), \quad (4.4.12)$$

$$d[F + F_{Na}]/dt = \sigma_{M_{Na}^*} I [M_{Na}^*](t). \quad (4.4.13)$$

Equation (4.4.10) shows that the change of $[M_{Na}]$ by one-photon absorption within one laser pulse is negligible when calculating (4.4.11), therefore $[M_{Na}] \approx [M_{Na}]_N(0)$, where $[M_{Na}]_N(0)$ represent the M_{Na} density at the onset of laser pulse N.

From the rate equation (4.4.11), we can derive the density population of the highly excited state M_{Na}^{**} .

Equation (4.4.11) can be rearranged as follows:

$$\frac{d[M_{Na}^{**}](t)}{dt} + (k_5 + k_6) [M_{Na}^{**}](t) = \sigma_{M_{Na}} [M_{Na}]_N(0) I \quad (4.4.14)$$

which is the first order linear differential equation of form:

$$\frac{dy}{dx} + yP(x) = Q(x),$$

The easier way to solve it, is to use an integrating factor which can be find by:

$$\mu(x) = e^{\int P(x)dx}$$

thereafter, multiply the differential equation by the integrating factor as follows:

$$\mu(x) \frac{dy}{dx} + \mu(x) yP(x) = \mu(x) Q(x).$$

The left side gives the derivative of product of $\mu(x)$ and y .

$$\frac{d}{dx} \left[e^{\int P(x)dx} y \right] = e^{\int P(x)dx} Q(x).$$

Finally, we can now integrate both sides of the differential equation.

Hence, it follows that the integrating factor of equation (4.4.14) can be found as:

$$\begin{aligned} \mu(t) &= e^{\int_0^t (k_5+k_6)d\tau_L} \\ &= e^{(k_5+k_6)t} \end{aligned} \quad (4.4.15)$$

By multiplying equation (4.4.14) by the integrating factor (4.4.18), we get:

$$e^{(k_5+k_6)t} \frac{d[M_{Na}^{**}](t)}{dt} + e^{(k_5+k_6)t} (k_5 + k_6) [M_{Na}^{**}](t) = e^{(k_5+k_6)t} \sigma_{M_{Na}} [M_{Na}]_N(0) I$$

The left side of the above equation is can be rewritten as :

$$\frac{d}{dt} \left[e^{(k_5+k_6)t} [M_{Na}^{**}](t) \right] = e^{(k_5+k_6)t} \sigma_{M_{Na}} [M_{Na}]_N(0) I \quad (4.4.16)$$

Now we can integrating equation (4.4.16) over a single laser pulse duration by knowing that at the onset of laser pulse, the density of the highly excited state M_{Na}^{**} is assumed to be zero. We obtain:

$$\begin{aligned} e^{(k_5+k_6)\tau_L} [M_{Na}^{**}](t) &= \sigma_{M_{Na}} [M_{Na}]_N(0) I \int_0^{\tau_L} e^{(k_5+k_6)t} dt \\ &= \frac{\sigma_{M_{Na}} [M_{Na}]_N(0) I}{(k_5 + k_6)} \left[e^{(k_5+k_6)\tau_L} - 1 \right] \end{aligned}$$

$$[M_{Na}^{**}](t) = \frac{\sigma_{M_{Na}} [M_{Na}]_N(0) I}{(k_5 + k_6)} \left[1 - \frac{1}{e^{(k_5+k_6)\tau_L}} \right] \quad (4.4.17)$$

Considering that $(k_5 + k_6) \gg 1/\tau_L$, the last term in the bracket becomes approximately zero. Therefore

$$[M_{Na}^{**}](t) = \frac{\sigma_{M_{Na}} [M_{Na}]_N(0) I}{(k_5 + k_6)} \quad (4.4.18)$$

We are going to use now equation (4.4.18) to find the population of the fluorescence state M_{Na}^* at the end of laser pulse N.

Substituting equation (4.4.18) into the rate equation (4.4.12), we get:

$$\frac{d[M_{Na}^*](t)}{dt} = \left(\frac{k_6}{k_5 + k_6} \right) \sigma_{M_{Na}} [M_{Na}]_N(0) I - (k_4 + \sigma_{M_{Na}}^* I) [M_{Na}^*](t)$$

It can be rearranged as follows:

$$\frac{d[M_{Na}^*](t)}{dt} + (k_4 + \sigma_{M_{Na}}^* I) [M_{Na}^*](t) = \left(\frac{k_6}{k_5 + k_6} \right) \sigma_{M_{Na}} [M_{Na}]_N(0) I, \quad (4.4.19)$$

which is the first order linear differential equation of form :

$$\frac{dy}{dt} + yP(t) = Q(t),$$

with: $y = [M_{Na}^*](t)$, $P(t) = (k_4 + \sigma_{M_{Na}}^* I)$, $Q(t) = \left(\frac{k_6}{k_5 + k_6} \right) \sigma_{M_{Na}} [M_{Na}]_N(0) I$.

The integrating factor of equation (4.4.19) can be obtained as follows:

$$\begin{aligned} \mu(t) &= e^{\int_0^t (k_4 + \sigma_{M_{Na}}^* I) dt} \\ \text{Hence : } \mu(t) &= e^{(k_4 + \sigma_{M_{Na}}^* I)t} \end{aligned} \quad (4.4.20)$$

Multiplying both side of equation (4.4.19) by the integrating factor (4.4.20) and rewrite the left side as the derivative of product of $\mu(t)$ and $[M_{Na}^*](t)$, we obtain the flowing equation:

$$\frac{d}{dt} \left[e^{(k_4 + \sigma_{M_{Na}}^* I)t} [M_{Na}^*](t) \right] = e^{(k_4 + \sigma_{M_{Na}}^* I)t} \left(\frac{k_6}{k_5 + k_6} \right) \sigma_{M_{Na}} [M_{Na}]_N(0) I \quad (4.4.21)$$

Integrating the above equation over the whole laser pulse duration, it follows that

$$\int_0^{\tau_L} d \left[e^{(k_4 + \sigma_{M_{Na}^*} I)t} [M_{Na}^*] (t) \right] = \int_0^{\tau_L} \left(\frac{k_6}{k_5 + k_6} \right) \sigma_{M_{Na}} [M_{Na}]_N (0) I e^{(k_4 + \sigma_{M_{Na}^*} I)t} dt$$

$$\left[e^{(k_4 + \sigma_{M_{Na}^*} I)t} [M_{Na}^*] (t) \right]_0^{\tau_L} = \left(\frac{k_6}{k_5 + k_6} \right) \sigma_{M_{Na}} [M_{Na}]_N (0) I \int_0^{\tau_L} e^{(k_4 + \sigma_{M_{Na}^*} I)t} dt$$

We are assuming that $[M_{Na}^*]_N (0) = 0$, since $\tau_{fl} = \frac{1}{k_4} \ll \tau_{dp}$ so that at the onset of laser pulse, the density of the fluorescent state is zero. Hence :

$$e^{(k_4 + \sigma_{M_{Na}^*} I)\tau_L} [M_{Na}^*] (\tau_L) = \left(\frac{k_6}{k_5 + k_6} \right) \frac{\sigma_{M_{Na}} [M_{Na}]_N (0) I}{(k_4 + \sigma_{M_{Na}^*} I)} \left[e^{(k_4 + \sigma_{M_{Na}^*} I)\tau_L} - 1 \right]$$

$$e^{(k_4 + \sigma_{M_{Na}^*} I)\tau_L} [M_{Na}^*] (\tau_L) = \left(\frac{k_6}{k_5 + k_6} \right) \frac{\sigma_{M_{Na}} [M_{Na}]_N (0) I}{(k_4 + \sigma_{M_{Na}^*} I)} \left[e^{(k_4 + \sigma_{M_{Na}^*} I)\tau_L} - 1 \right]$$

$$[M_{Na}^*] (\tau_L) = \left(\frac{k_6}{k_5 + k_6} \right) \frac{\sigma_{M_{Na}} [M_{Na}]_N (0) I}{(k_4 + \sigma_{M_{Na}^*} I)} \left[1 - e^{-(k_4 + \sigma_{M_{Na}^*} I)\tau_L} \right] \quad (4.4.22)$$

By taking into account that $(k_4 + \sigma_{M_{Na}^*} I) \gg \frac{1}{\tau_L}$, implied that the last term of the right side of equation (4.4.22) is negligible. Hence:

$$[M_{Na}^*] (\tau_L) = \left(\frac{k_6}{k_5 + k_6} \right) \frac{\sigma_{M_{Na}} [M_{Na}]_N (0) I}{(k_4 + \sigma_{M_{Na}^*} I)} \quad (4.4.23)$$

Equation (4.4.23) tells us about the density of population of the fluorescent state $[M_{Na}^*] (\tau_L)$ at the end of laser pulse N.

By writing (4.4.23) in terms of t and inserted t into (4.4.13), we obtain:

$$\frac{d[F + F_{Na}]}{dt} = \sigma_{M_{Na}^*} I \left(\left(\frac{k_6}{k_5 + k_6} \right) \frac{\sigma_{M_{Na}} [M_{Na}]_N (0) I}{(k_4 + \sigma_{M_{Na}^*} I)} \right) \quad (4.4.24)$$

Integrating the above equation over laser pulse duration and having in mind that $[F + F_{Na}] (0) = 0$ if only the change during one laser pulse is calculated, we get the following expression:

$$[F + F_{Na}] (\tau_L) = \sigma_{M_{Na}^*} \sigma_{M_{Na}} I^2 \left(\frac{k_6}{k_5 + k_6} \right) \left(\frac{[M_{Na}]_N (0) \tau_L}{k_4 + \sigma_{M_{Na}^*} I} \right), \quad (4.4.25)$$

which is equivalent to the density decrease of the M_{Na} centers by photo dissociation.

At the end of the laser pulse duration , the remaining M_{Na} density is given by:

$$[M_{Na}]_N(\tau_L) = [M_{Na}]_N(0) - [F + F_{Na}](\tau_L) \quad (4.4.26)$$

Therefore:

$$\begin{aligned} [M_{Na}]_N(\tau_L) &= [M_{Na}]_N(0) - \sigma_{M_{Na}^*} \sigma_{M_{Na}} I^2 \left(\frac{k_6}{k_5 + k_6} \right) \left(\frac{[M_{Na}]_N(0) \tau_L}{k_4 + \sigma_{M_{Na}^*} I} \right) \\ &= [M_{Na}]_N(0) \left[1 - \sigma_{M_{Na}^*} \sigma_{M_{Na}} I^2 \left(\frac{k_6}{k_5 + k_6} \right) \left(\frac{\tau_L}{k_4 + \sigma_{M_{Na}^*} I} \right) \right] \end{aligned}$$

Hence:

$$[M_{Na}]_N(\tau_L) = [M_{Na}]_N(0) \varepsilon, \varepsilon < 1, \quad (4.4.27)$$

where $\varepsilon = 1 - \sigma_{M_{Na}^*} \sigma_{M_{Na}} I^2 \left(\frac{k_6}{k_5 + k_6} \right) \left(\frac{\tau_L}{k_4 + \sigma_{M_{Na}^*} I} \right)$.

4.4.4 Results of the model

The first result of this model is the possibility of calculation of the steady state density M_{Na} for a large laser pulse series. Taking into consideration a large laser pulse series at constant fluence H and τ_{dp} for each dark period between two laser pulses. The density $[M_{Na}]_N(\tau_L)$ at the end of N laser pulses can be obtained by the following geometric series [1]:

$$[M_{Na}]_N(\tau_L) = \varepsilon^N [M_{Na}]_0(0) + [M_{Na}]_N(\tau_{dp}) \frac{1 - \varepsilon^N}{1 - \varepsilon}. \quad (4.4.28)$$

In the equation above $[M_{Na}]_0(0)$ denote the initial $[M_{Na}]_N$ density of the virgin non-irradiated sample.

In steady state for $N \gg 1$ implies that $\varepsilon^N \ll 1$, which implies that the first term in the right side of equation (4.4.28) become approximately zero. Thus,

$$[M_{Na}]^{st} = [M_{Na}]_N(\tau_{dp}) \frac{1}{1 - \varepsilon}. \quad (4.4.29)$$

Inserting the value of $[M_{Na}]$ (τ_{dp}) from equation (4.4.9) into (4.4.29) and replacing ε by its value, we get:

$$[M_{Na}]^{st} = \left(\frac{k_6 + k_5}{k_6} \right) \left(\frac{k_3(T) [F_{Na}]}{k_2 + k_3(T) [F_{Na}]} \right) \frac{\sigma^{(2)} [CaF_2] (k_4 + \sigma_{M_{Na}^*} I)}{\sigma_{M_{Na}} \sigma_{M_{Na}^*}}, \quad (4.4.30)$$

which is the density population of $[M_{Na}]$ at the steady state.

We can now obtain the steady state population of the fluorescent state M_{Na}^* via the substitution of $[M_{Na}]_N(0)$ in (4.4.23) by $[M_{Na}]^{st}$, Hence:

$$[M_{Na}^*]^{st} = \left(\frac{k_3(T) [F_{Na}]}{k_2 + k_3(T) [F_{Na}]} \right) \frac{\sigma^{(2)} [CaF_2] I}{\sigma_{M_{Na}^*}}. \quad (4.4.31)$$

The two additional contributions to the steady state absorption coefficient α^{st} ($H = I\tau_L$) from the M_{Na} center are given by :

$$\begin{aligned} \alpha_{M_{Na}}^{st}(H) &= \sigma_{M_{Na}} [M_{Na}]^{st} \\ &= \left(\frac{k_3(T) [F_{Na}]}{k_2 + k_3(T) [F_{Na}]} \right) \times \left(\frac{k_6 + k_5}{k_6} \right) \frac{\beta^{int}}{\sigma_{M_{Na}^*}} \left(k_4 + \sigma_{M_{Na}^*} \frac{H}{\tau_L} \right), \end{aligned} \quad (4.4.32)$$

which is the absorption $\alpha_{M_{Na}}^{st}(H)$ from the ground state M_{Na} and

$$\begin{aligned} \alpha_{M_{Na}^*}^{st}(H) &= \sigma_{M_{Na}^*} [M_{Na}^*]^{st} \\ &= \left(\frac{k_3(T) [F_{Na}]}{k_2 + k_3(T) [F_{Na}]} \right) \times \left(\frac{k_6 + k_5}{k_6} \right) \frac{\beta^{int}}{\tau_L} H, \end{aligned} \quad (4.4.33)$$

which is the absorption $\alpha_{M_{Na}^*}^{st}(H)$ from the fluorescence state M_{Na}^* , where $\beta^{int} = \sigma^{(2)} [CaF_2]$ is the intrinsic two-photon absorption coefficient of CaF_2 .

$\alpha^{st}(H)$ can be expressed as the sum of effective one-photon and two-photon coefficients :

$$\alpha^{st}(H) = \alpha^{eff} + \beta^{eff} \left(\frac{H}{\tau_L} \right).$$

$\alpha_{M_{Na}}^{st}(H)$ in equation (4.4.32) contributes both to α^{eff} and β^{eff} while $\alpha_{M_{Na}^*}^{st}(H)$ in equation (4.4.33) contributes to β^{eff} .

The effective one and two-photon absorption coefficients for those samples which contain the M_{Na} centers are now obtained by using the following formula :

$$\alpha^{eff} = \alpha^{int} + \alpha^{add} \quad \text{and} \quad \beta^{eff} = \beta^{int} + \beta^{add},$$

with α^{int} and β^{int} the intrinsic values of high pure calcium fluoride samples. α^{add} and β^{add} are the contributions from $\alpha_{M_{Na}}^{st}(H)$ and $\alpha_{M_{Na}^*}^{st}(H)$:

$$\alpha^{add} = \left(\frac{k_3(T) [F_{Na}]}{k_2 + k_3(T) [F_{Na}]} \right) \left(\frac{k_6 + k_5}{k_6} \right) \frac{\beta^{int}}{\sigma_{M_{Na}^*}} k_4, \quad (4.4.34)$$

$$\beta^{add} = \left(\frac{k_3(T) [F_{Na}]}{k_2 + k_3(T) [F_{Na}]} \right) \left(1 + \frac{k_6 + k_5}{k_6} \right) \beta^{int}. \quad (4.4.35)$$

The model of generation and annealing of M_{Na} center provides valuable information about the spectroscopy of CaF_2 . Among these useful informations, it is important to emphasize the dependency of the M_{Na} defect on the applied laser pulse duration as well as its temperature dependency. Because M_{Na} state is formed after a thermal activation when H center diffuses away from the F center. In addition, we must keep in mind that due to its large band gap, CaF_2 crystal can only be excited by two-photon absorption, so the energy quantity of the incident beam is also a crucial factor in the investigation of impurities and defect in CaF_2 crystal.

Chapter 5

Experimental Setups

5.1 Experimental setup of McPherson Model 225 monochromator

The experiment setup of McPherson Model 225 monochromator used in this thesis for doing absorption measurements of CaF_2 samples over a wider spectral range at a lower spectral resolution is illustrated in Figure 5.1.

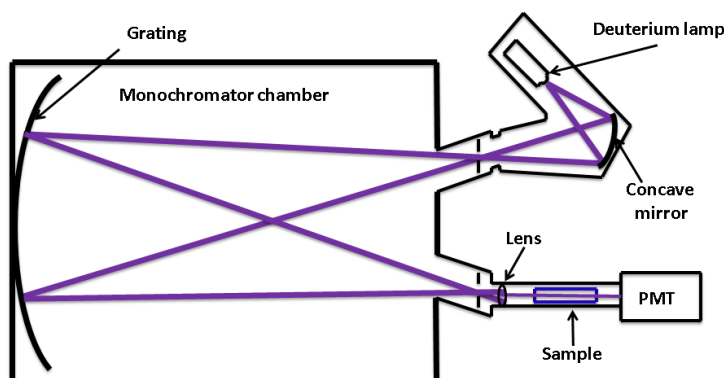


Figure 5.1: Schematic illustration of the experimental setup for absorption measurements of CaF_2 with a McPherson Model 225 monochromator. Components are not drawn to scale. The vacuum system is not shown.

UV light emitted by Model 632 Deuterium lamp is focused onto the entrance slit of the McPherson 225 monochromator via a concave mirror ($f = 175$ mm). The incoming UV light is diffracted by the grating according to the wavelengths and then passes through the exit slit. A sample cell (130 mm long) is mounted directly after the exit slit.

A focussing lens (ϕ 32 mm) is inserted between the exit slit of the monochromator and the sample cell in order to converge the UV light on the center of cell. A photomultiplier tube (PMT) Hamamatsu R6836 (sensitivity : 115-380 nm) is used to detect the light transmitted through the sample cell. The signal from the PMT is amplified by the amplifier (Keithley 427 current amplifier) and digitalised by a computer interface (Stanford Research Systems, SR 245). A custom program is used for saving the measurements in the computer. A boxcar (Stanford Research Systems, SR 245) was used to provide a trigger signal for the acquisition of data by the computer interface.

McPherson 225 monochromator contains a scanning motor which by rotating the grating scans the wavelengths from about 30 nm up to 300 nm. The optical specification of McPherson 225 monochromator is shown in Table 5.1.

Concave grating focal length	995.4 mm
Grating	Grooves : 1200 lines/mm Blaze wavelength : 1200Å Ruled area : 96 rule width Resolving power: +75 % of theoretical
Reciprocal Linear Dispersion	0.83 nm/mm

Table 5.1: *Optical specifications of the McPherson Model 225 monochromator*

The monochromator (up to the D_2 lamp window) and the sample cell are evacuated or purged separately.

The evacuation of the monochromator is done by a pre-vacuum pump (rotary) and a turbo-molecular pump (Pfeiffer Balzers, TPU 240, 230 l/s) and with these pumps in operation, the pressure in the monochromator reaches 10^{-6} mbar even less.

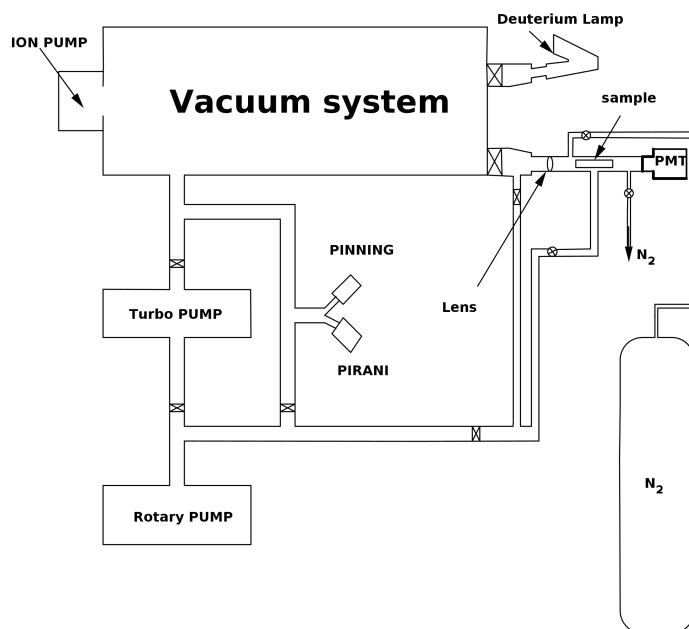


Figure 5.2: Schematic illustration of the McPherson 225 monochromator vacuum system

For initial experiments the sample cell was evacuated by the pre-vacuum pump and then continuously purge with high purity nitrogen gas (Afrox, N_2 Baseline 5.0).

5.1.1 Experimental setup of monochromator with sample cell under vacuum

A new setup was made in order to carry out the experiment with both monochromator and sample cell under vacuum. The motivation was to verify whether the structures found using a sample cell purge by nitrogen in all our CaF_2 samples around 120-125 nm (see section 6.3.3.1) were actually bands absorption of CaF_2 samples or just an absorption due to the residual amount of oxygen from the sample cell and the nitrogen itself. To achieve this, one added a turbo-molecular pump (Alcatel Adixen ATH 200) and a rotary pump (Alcatel Adixen Pascal Series 2015SD) for pumping out only the sample cell in order to obtain a good vacuum which will reduce the effect of the out-gassing on the measurements. With these two pumps operating, we did obtain a pressure around 3×10^{-6} mbar in the sample cell. The monochromator was evacuated by its vacuum system. Other components of this experiment were the same as in shown in Figure 5.1.

The experimental setup of monochromator with sample cell under vacuum is illustrated in Figure 5.3.

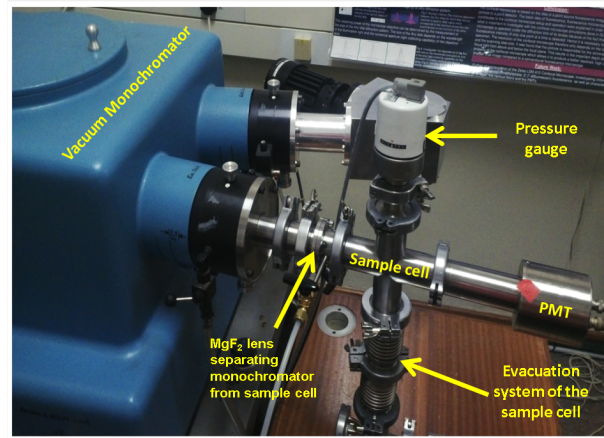


Figure 5.3: *Photo of the new setup in which the sample cell is under vacuum.*

5.1.2 Setup for wavelength calibration of the McPherson Model 225 monochromator using Mercury lamp

The setup for the wavelength calibration of McPherson Model 225 monochromator is sketched in Figure 5.4. A mercury lamp was used as light source. A PMT (Hamamatsu, R106) was mounted at the exit slit in order to detect the light from the monochromator. This wavelength calibration was done in air at atmospheric pressure.

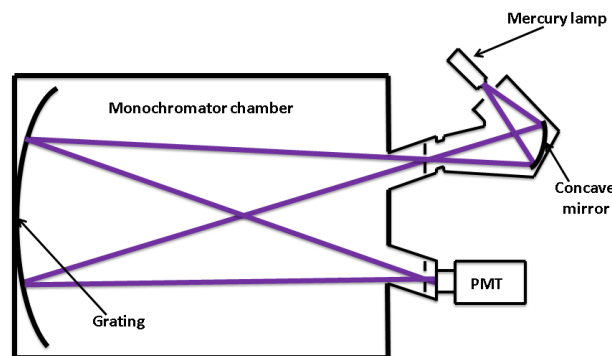


Figure 5.4: *Schematic illustration of the setup for wavelength calibration.*

5.2 Experimental setup of the VUV laser source

The experimental setup for the generation of tunable vacuum ultraviolet laser light with a narrow spectral bandwidth by four-wave frequency mixing is illustrated in Figure 5.5.

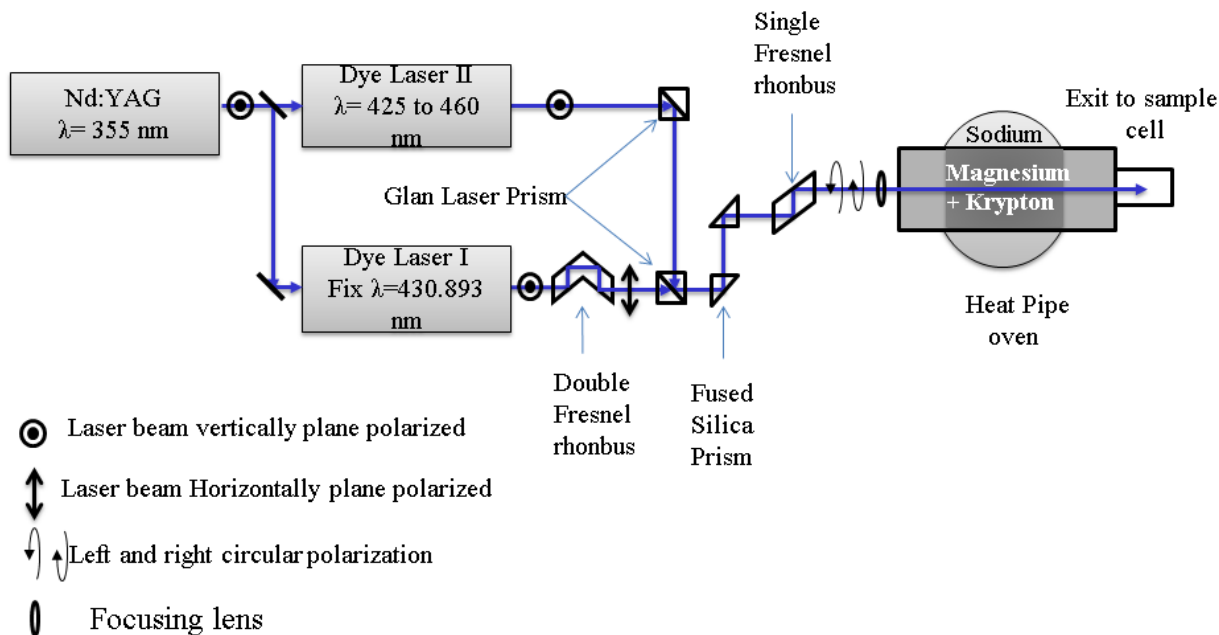


Figure 5.5: Diagram of the experimental setup for the generation of tunable VUV by sum-frequency mixing. Details of the heat pipe oven setup are not shown.

In this setup, we used two dye lasers (both using Coumarine 440 dye dissolved in ethanol). Dye laser I in the Figure 5.5 is a FL 3001X Dye Laser of lambda physik and dye laser II is Cobra Stretch Dye Laser of Sirale. The FL3001X Dye laser has been converted so that it can be pumped by 355 nm. Both Dye laser are pumped by the same Nd:YAG laser (Spectra Physics) Quanta Ray with a pulse energies at 500 mJ/pulse and pulse duration 10 ns in order to have a good temporal overlap. Dye laser I (pulse energies 15 mJ) provides the two-photon resonant wavelength at 430.949 nm. Dye laser II is tuned from 425 nm to 455 nm with a pulse energies equal to 15 mJ at 440 nm.

The beam from dye laser II is reflected by the first Glan laser prism to be combined with the beam from the dye laser I at the second Glan laser prism.

The polarisation of the beam from dye laser I is changed from vertical to horizontal polarisation when passing through the Double Fresnel Rhombus (DFR). The fused silica prisms are used for bringing the beams on the correct height and alignment.

In order to suppress the generation of the third harmonic of the resonance laser light which takes place in the non linear medium (see section 2.4), these beams have to be correctly circular polarized. This is done by using the single Fresnel Rhombus (FR) which changes the polarization of the beams from the vertical and horizontal polarizations to left and right circular polarisation respectively. The lens (L) is used for focussing the light in the

center of the heat pipe oven, where the incident light interacts with the magnesium vapour krypton gas medium to generate the sum-frequency VUV light. More details about the heat pipe oven can be found here [22].

In the Mg-Kr medium the sum frequency $\omega_{SF} = 2\omega_1 + \omega_2$ is generated, where ω_1 is the two-photon resonant frequency of the dye laser I and ω_2 is the tunable frequency of dye laser II. This process is illustrated in Figure 2.2(b).

5.3 Experimental setup for absorption measurements of CaF_2 using the VUV laser source

For achieving our purpose of doing an absorption spectroscopy of CaF_2 using the tunable sum-frequency VUV laser light, a new setup illustrated in Figure 5.6 was built and mounted onto the existing setup shown in Figure 5.5. In order to measure simultaneously the intensity of the VUV beam with and without the sample for the calculation of the absorbance, a fraction of the VUV beam is split off before and after the sample. Two solarblind photomultiplier tubes (Hamamatsu R6836, sensitivity : 115-380 nm) are used to detect the laser pulses. The signal (average over 10 pulses) of each laser pulse is integrated by a boxcar integrator (Stanford Research System SR 250). The signal was visualized using an oscilloscope (Tektronix TDS 2014) in order to adjust the boxcar (SR 250) gate. The digitalisation of the integrated signal from the PMT is done by a National Instruments multifunction data acquisition device (DAQ NI USB-6211). The data is saved in the computer by a customer program written with LabView code.

As the VUV light is strongly absorbed by the oxygen, this experiment was done under vacuum. The evacuation of the sample cell was done by a rotary pump (Alcatel Adixen Pascal Series 2015SD) and turbo-molecular pump (Alcatel Adixen ATH 200).

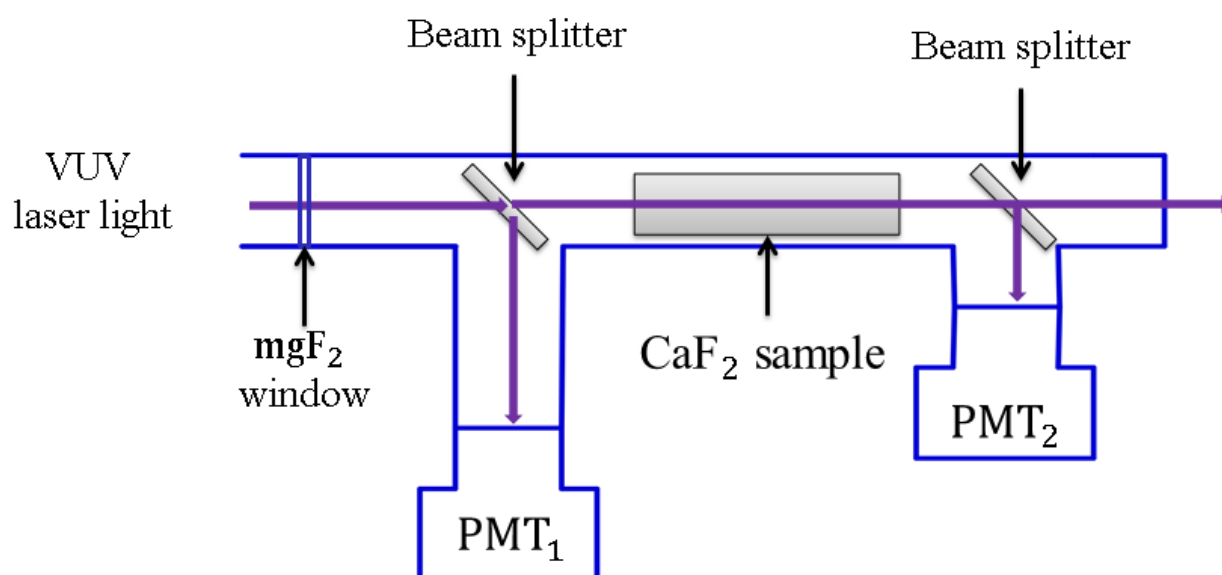


Figure 5.6: Setup of absorption measurements of CaF_2 using the VUV laser source. The vacuum pumps and gauges are not shown.

Chapter 6

Results and discussion

Two setups for absorption spectroscopy has been developed and applied in this thesis. Firstly a setup using a monochromator (McPherson 225 monochromator) operating with a deuterium lamp McPherson model 632 is used for doing the absorption measurements over a wider spectral range at a lower spectral resolution. Secondly a setup using a narrow-bandwidth tuneable VUV laser is used for doing absorption measurements in 143.5 to 146.7 nm range. This setup operates with two photomultiplier tubes which record simultaneously the intensity of the incident light before and after the sample.

6.1 Characterisation of the McPherson 225 monochromator

6.1.1 Wavelengths calibration of the McPherson 225 monochromator

A McPherson 225 monochromator is used in this thesis for doing absorption measurements of CaF_2 samples over a wider spectral range at a lower spectral resolution. It is known that the optical device, such as a monochromator needs to be calibrated before it can be used. To achieve this, a mercury lamp was utilised for wavelengths calibration since its emission peaks are well known. The setup illustrated in Figure 5.4 was used.

Figure 6.1 shows the experimental spectrum of the mercury lamp. The wavelength in nanometre is approximately given by half of the counter reading of the instrument.

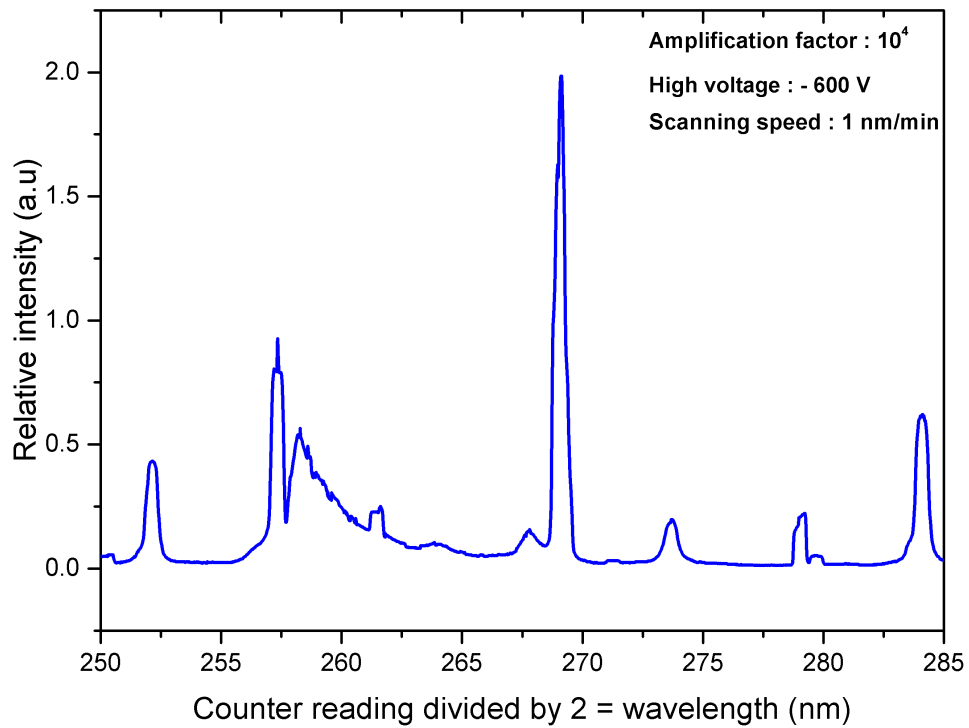


Figure 6.1: Emission spectrum of mercury lamp recorded with PMT R106.

Several wavelengths peaks of our experimental spectrum of mercury lamp are compared with the well-known mercury lines from NIST tables [23] which is plotted in Figure 6.2 in order to find the linear regression for the calibration of the monochromator.

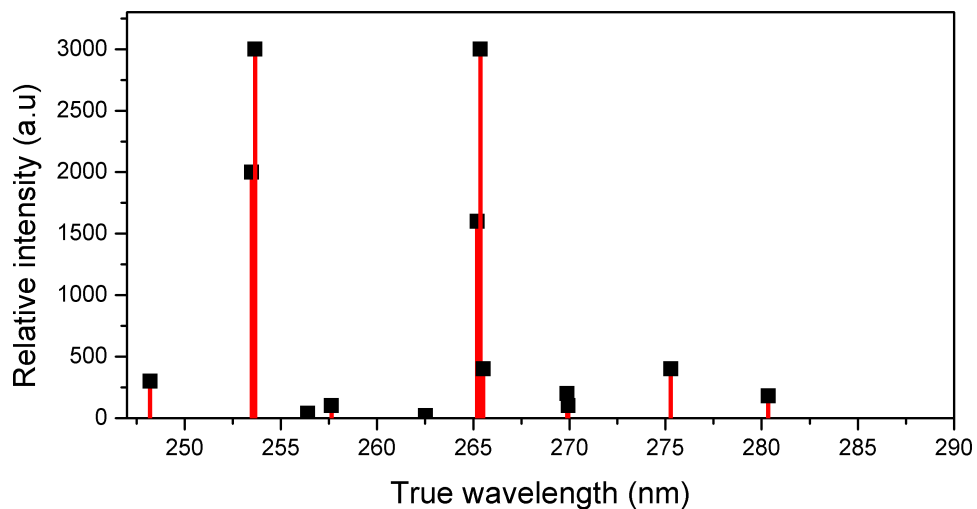


Figure 6.2: Plot of mercury lines from NIST tables

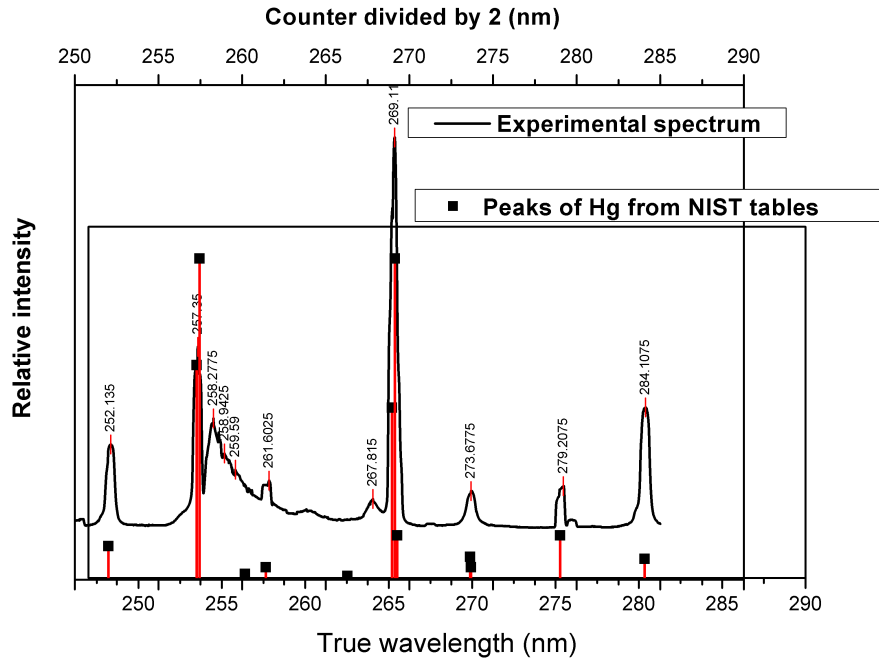


Figure 6.3: Comparison of the experimental spectrum against the plot of the mercury lines from NIST tables.

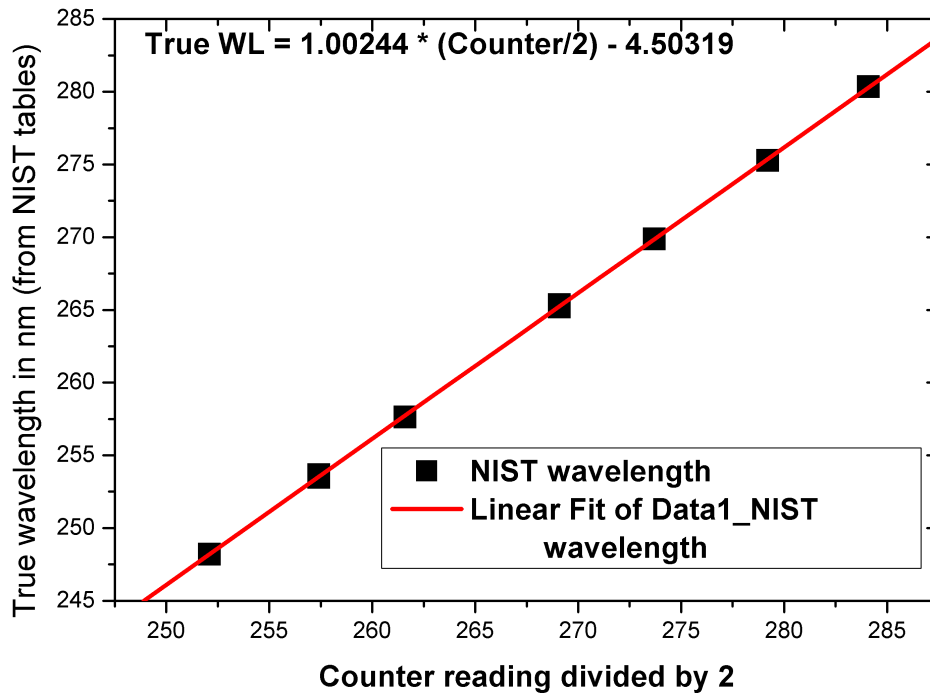


Figure 6.4: Plot of mercury line wavelengths from NIST tables against the counter reading divided by 2.

The result of the linear fit of the mercury wavelengths from the NIST tables against the measured counter reading of the monochromator divided by 2 show in Figure 6.4 reveals that for a given counter reading, the true wavelength values is obtained by :

$$\text{True wavelength} = 1.00244 \times \left(\frac{\text{counter reading}}{2} \right) - 4.50319 \quad (6.1.1)$$

We used (6.1.1) as approximate calibration for futures scans, but we also used the Deuterium lamp lines for more accurate calibration as described in 6.2.3.

6.1.2 Investigation of the effect of the slit widths of the of the monochromator

The slit width is a crucial parameter in the experiment for absorption spectroscopy since it determines the spectral resolution. Therefore, the choice of slit widths is important in the optimization of the monochromator. This section will be devoted to the influence of slit widths on the resolution and intensity of the output signal of the monochromator.

In order to find optimum slit widths for our purpose, which is doing absorption spectroscopy of calcium fluoride, several deuterium lamp spectra were recorded with different slit widths. Deuterium lamp (model 632 McPherson) was used as light source and was focused onto the entrance slit of the monochromator. The detector (Photomultiplier tube Hamamatsu R6836, sensitive at 115 to 320 nm) was mounted directly after the exit slit. The monochromator was filled with 1 bar N₂ (nitrogen 5.0).

For this investigation, three different sets of measurement were recorded.

The first measurements were performed with a constant entrance slit width set at 20 micrometer while the exit slit width was changed successively at 200, 400, 600, 800 and 1000 micrometer (Figure 6.5). The first result of this investigation is plotted in Figure 6.5.

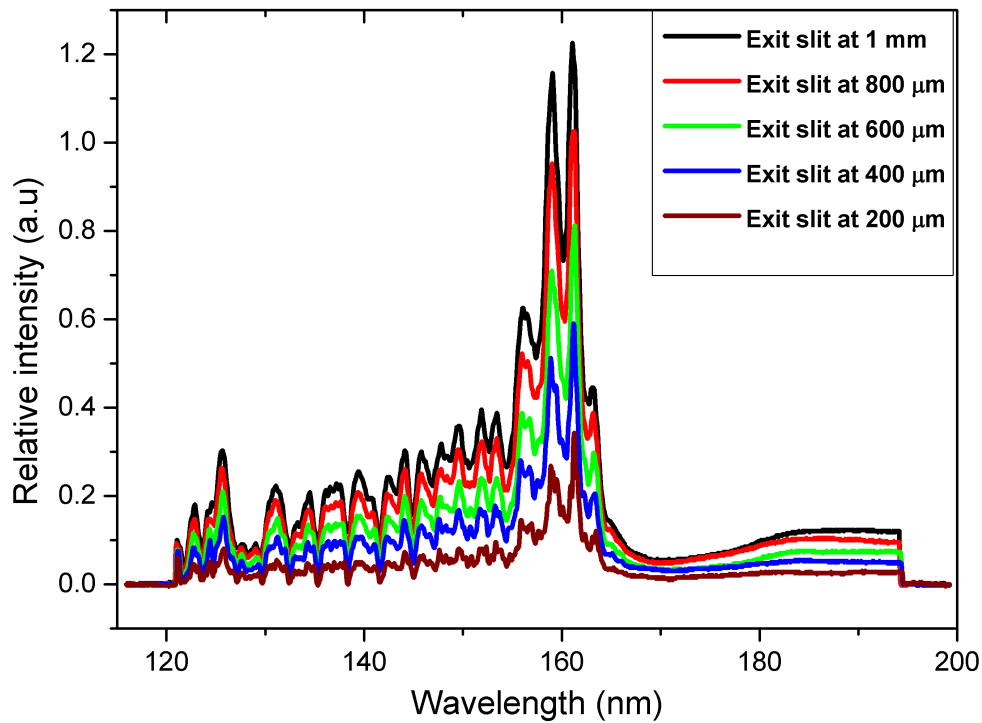


Figure 6.5: Deuterium lamp spectra recorded in 1 bar N_2 , with an entrance slit fixed at 200 μm while the exit slits were successively changed to 200, 400, 600, 800 and 1000 micrometers.

From Figure 6.5 it can be observed that the intensities of the spectrum increase according to the slit width. This can be visualised in the following figures where the height and width of the peaks are plotted against the slit widths.

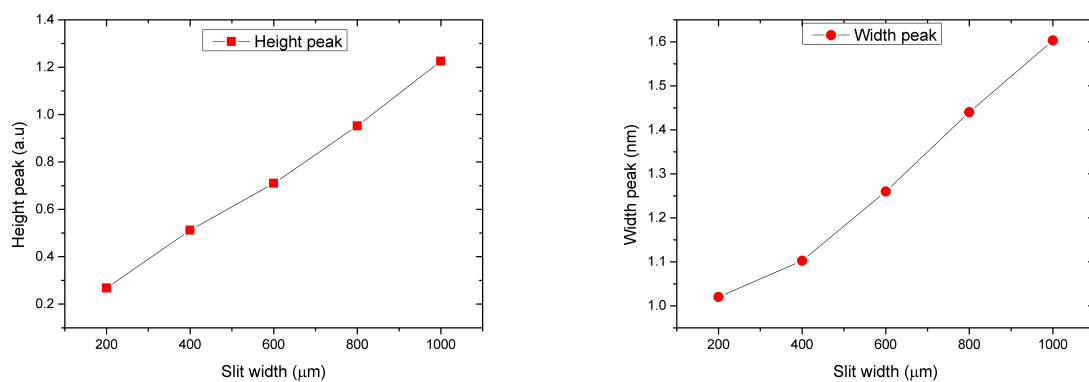


Figure 6.6: Plot of the height and width of the peaks of the first set of measurements against the slit width. For this example the peak at 160 nm was considered and its width is determined by the full width at 3/4 maximum.

Figure 6.6 shows that the height of peaks increase with the same factor as the exit slit width (if the slit width doubles, then the peak height also double). This can be explained by the fact that the amount of light that is transmitted through the monochromator increases with the increase of the exit slit width. The widths of the peaks also increase linearly with the slit width, due to the increase in spectral bandpass with increased exit slit width.

For the second set of measurements the spectrum is shown in Figure 6.7. The exit slit was fixed at 200 μm for all the measurement while the entrance slit was changed successively at 200, 400, 600, 800 and 1000 micrometer.

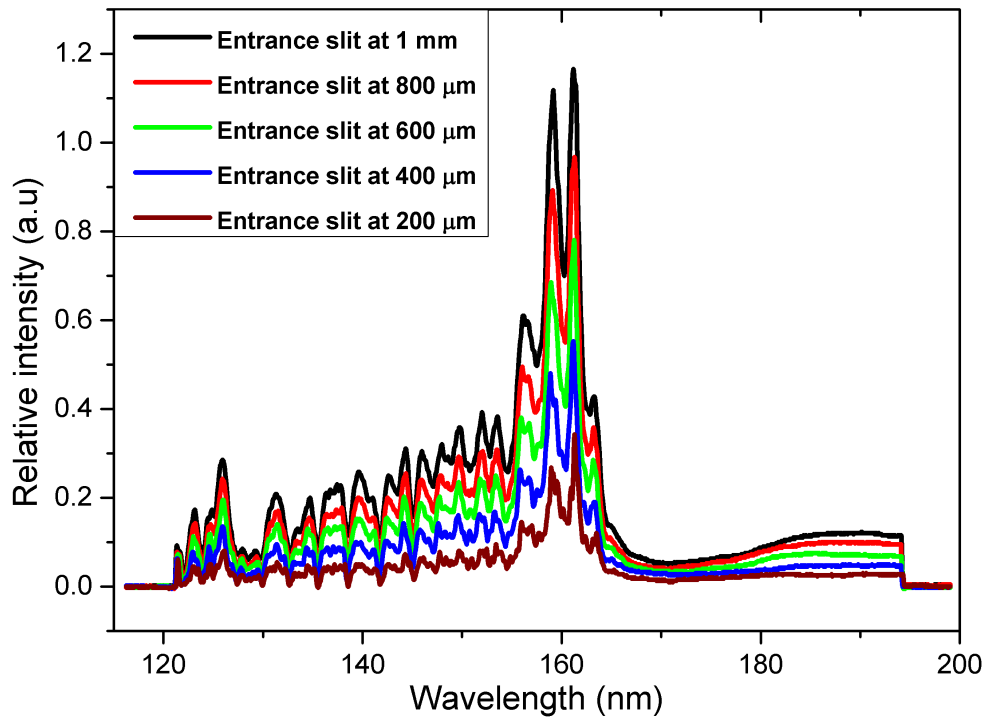


Figure 6.7: Deuterium lamp spectra recorded in 1 bar N_2 , with the exit slit fixed at 200 μm while the entrance slits were successively changed to 200, 400, 600, 800 and 1000 micrometer.

Figure 6.7 shows that the intensity of the spectrum increases with the same factor as the entrance slit. This can be verified in Figure 6.8 where the height and width of peaks are plotted against the slit widths in order to quantify the increase of the intensity of the spectrum with slit width. The peak width increases linearly with slit width in Figure 6.8 similar to Figure 6.6.

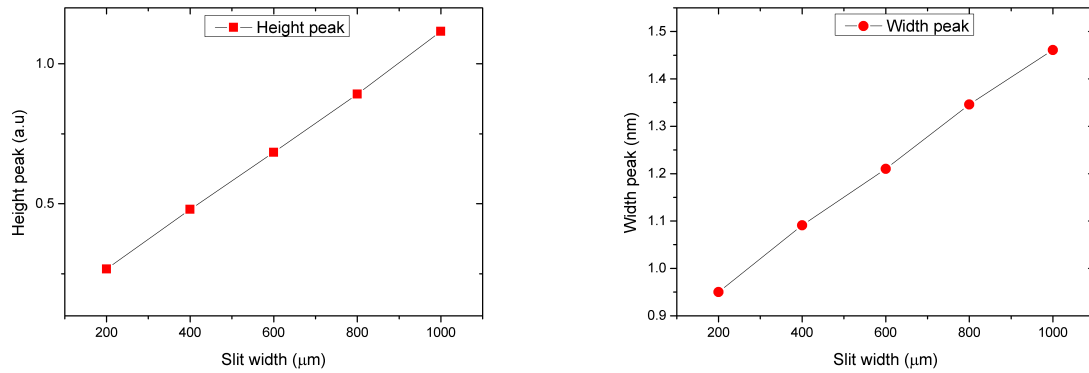


Figure 6.8: Plot of the height and width of peaks of the second set of measurements against the slit width. For this example the peak at 160 nm was considered and the width is determined by the full width at 3/4 maximum.

The last measurements shown in Figure 6.9 were performed with both entrance and exit slit set at the same value. The increase of the intensity of the spectrum with respect to slit widths can be also observed here. This is because of the amount of light which enters into and exits from the monochromator increase with the increases of the slit widths.

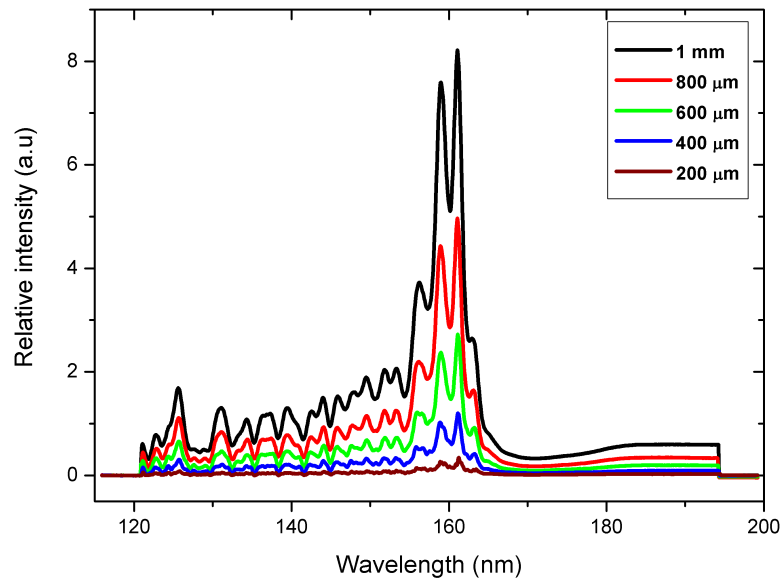


Figure 6.9: Deuterium lamp spectra recorded in 1 bar N_2 , with both entrance and exit slits in the same width.

Figure 6.10 shown the increase of the height and width of peaks with the slit widths. The increase of the peak height with slit width is not linear any more. If slit width increase with factor x , then peak height increases by approximately x^2

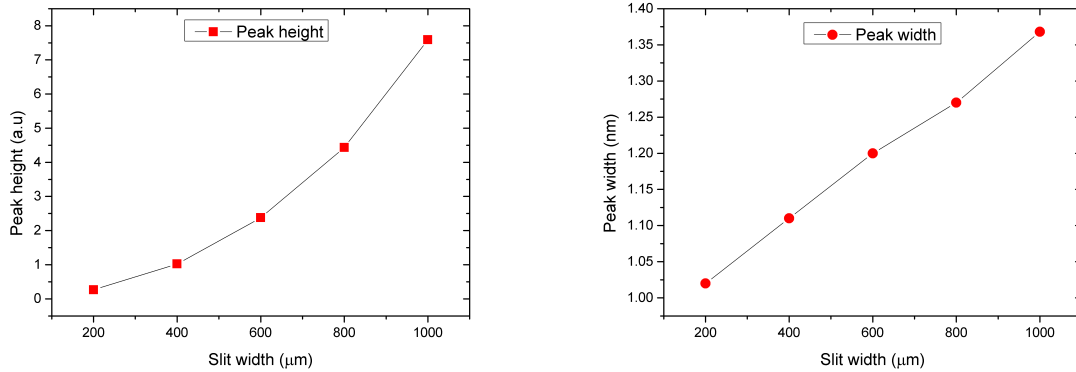


Figure 6.10: Plot of the height and width of peaks of the third set of measurements against the slit width. For this example the peak at 160 nm was considered and the width is determining by the full width at 3/4 maximum.

Comparing now the three highest intensity spectrum from Figures 6.5, 6.7 and 6.9, one can easily see that the highest intensity spectrum is obtained when both entrance and exit slits are adjusted at the maximum values (1mm). Furthermore, comparing the peak widths of approximately same size for a spectrum recorded with these three setups, it can be noticed that for the same peak width the highest intensity is obtained when both slits are set at the same values (Third setup). This can be verified in the table 6.1 where the height and width of one specific peak (peak at 160 nm) of each spectrum of these three set of measurements are shown.

Slit width (μm)	First set		Second set		Third set	
	Height (nm)	Width (nm)	Height (nm)	Width (nm)	Height (nm)	Width (nm)
200	0.26	0.87	0.26	0.95	0.26	1.02
400	0.51	1.02	0.47	1.09	1.02	1.11
600	0.70	1.26	0.68	1.21	2.37	1.2
800	0.95	1.44	0.89	1.34	4.43	1.27
1000	1.22	1.60	1.11	1.46	7.59	1.36

Table 6.1: Peak Characteristics for the three sets of measurements. The first, second and third sets represents the three set of measurements. First set: entrance slit 200 μm wide, exit slit varied. Second set: exit slit 200 μm wide, entrance slit width varied. Third set: both slit widths varied together.

The results shown in Table 6.1 indicate to us that for 1000, 800 and 600 μm of slit width used, the spectrum obtained with the third setup have the highest and narrowest peaks compared to the peaks of other setups.

In addition, for the same setup it is seen that taking a large slit width increase the light intensity of the spectrum but reduce directly its resolution. This can be explained by the fact that by increasing the slit width of the monochromator, we directly increase its band-pass which leads to the reduction of the resolution.

To illustrate this, we can compare for example the peaks height and peaks width for the same setup in the Table 6.1. This can be also pictured in Figure 6.11 where two spectra recorded at different slit widths are compared.

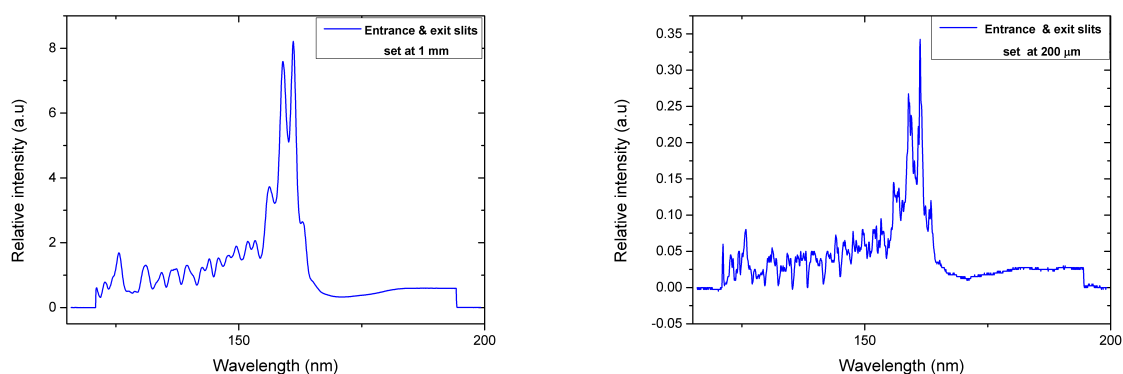


Figure 6.11: Comparison of two Deuterium lamp spectrum recorded with different slit widths. Both entrance and exit slit widths are set to 1000 μm (left hand graph) and 200 μm (right hand graph)

As observed experimentally, a small slit width increases the spectral resolution but unfortunately reduced the intensity of the signal. So, for our purpose of doing absorption spectroscopy of CaF_2 , it is necessary to reach a balance between a good resolution and a sufficient intensity of light.

6.1.3 Choice of purging gas for the sample cell

It is known that within the vacuum spectrometer there are always molecular contaminants which mostly arise from the residual air containing molecular oxygen and the out-gassing from chamber walls (hydrocarbon or silicone oils used to lubricate mechanisms, epoxies

used to mount optical components, paints)[24, 25, 26]. It is also known that when a contaminated optic is exposed for long period to an intense VUV radiation, this contaminant becomes fixed to the optic surface and contributed to the transmission degradation of this optic [26].

Taking into account the risk of molecular contaminants present in the spectrometer which strongly absorb the VUV light, purging with an inert VUV transparent gas is needed in the sample cell in order to avoid any contamination on the surface of the sample. Flushing continuously with an inert gas in the sample cell during the experiment reduces the effect of the residual impurity in the sample cell. This is because the remaining impurities (which has not be evacuated by the pumping) in the sample cell are now flushed away with the gas.

An investigation was made in order to find a suitable gas for this study. The setup illustrated in Figure 5.1 was used, and the empty sample cell was purged with gas. Measurements were recorded with nitrogen (Afrox, nitrogen Baseline 5.0), argon (Afrox, argon Baseline 5.0)(see Table 6.2 for gas properties) and under vacuum. Thereafter, their spectrum were compared in Figure 6.12 in order to find the most efficiently gas to use for our purpose. In other words we want to have a inert gas which can give us a good signal intensity compared to the signal obtained under vacuum.

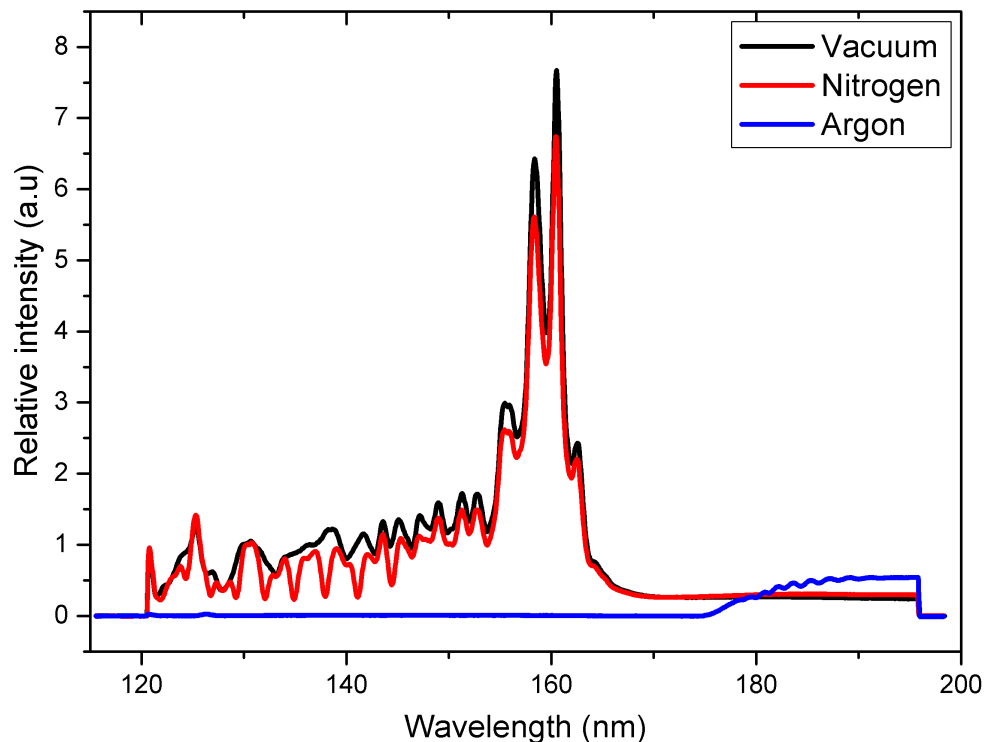


Figure 6.12: Deuterium lamp spectra recorded in vacuum, 1 bar N_2 and Ar.

From Figure 6.12, it can be observed that the argon absorbs practically all light in the range 120-180 nm. The nitrogen gas shows absorption features that correspond with the absorption bands of oxygen, present as impurity in the nitrogen. Therefore, the nitrogen will be used as purge gas in the sample cell for this study.

Specification	argon 5.0	nitrogen 5.0
Purity	≥ 99.999 vol%	≥ 99.999 vol% (incl.rare gases)
Impurity	O ₂ < 5 ppm H ₂ O < 5 ppm C _x H _y < 0.2 ppm	O ₂ < 5 ppm H ₂ O < 5 ppm C _x H _y < 0.2 ppm
Physical Properties		
Molecular weight(kg/kmol)	39.95	28.01
Density gas (kg/m ³ at 1.013 bar and 0°C)	1.784	1.251
Relative density (air=1)	1.380	0.967
Boiling point (K)	87.3	77.3
Critical temperature (K)	151.0	126.2

Table 6.2: *Specification Afrox argon Baseline 5.0 and nitrogen Baseline 5.0*

6.1.4 Calculation of residual molecular oxygen within the monochromator.

In this section, we want to investigate the concentration of oxygen in the nitrogen 5.0 based on the measurements. To achieve this, PMT was attached directly to the exit slit. Measurements taken with monochromator under vacuum (I_o) and the monochromator purged with nitrogen (I). The path length of the light through the monochromator is ≈ 2 m. Beer-Lambert law was used for obtaining the absorbance shows in Figure 6.13.

It can be seen from Figure 6.13 that there is oxygen absorption around 141 nm. So, for this investigation we will consider the absorption peak at wavelength approximately 141 nm as example for calculating the density of oxygen in the light path as molecules per cubic cm. The ideal gas law can be used to convert this to a pressure and then calculate how many part per million this is when compared to 1 bar nitrogen 5.0.

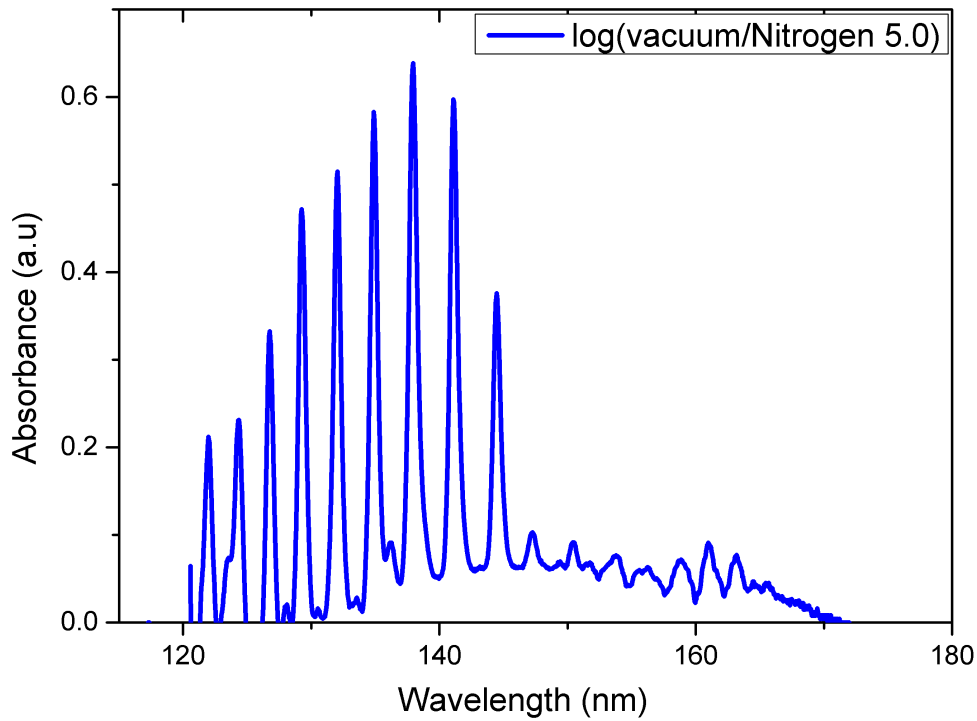


Figure 6.13: Residual oxygen absorption in the monochromator.

The Beer-Lambert law is given by

$$I = I_o \exp(-\sigma \rho l), \quad (6.1.2)$$

where I_o is the intensity of measurement in vacuum, I represents the intensity of measurement taken with nitrogen, σ is the absorption cross section of oxygen, l is the path length of the light in the spectrometer for the vacuum and nitrogen measurements and ρ is the density of the oxygen in the light path.

Considering the absorption peak at wavelength approximately 141 nm, we have the following experimental values :

- $I_o = 1.00324$
- $I = 0.29788$
- $\sigma = 2.5 \times 10^{-17} \text{cm}^2 \text{molecule}^{-1}$ according to Ogawa (1970).
- $l = 200 \text{cm}$

Equation 6.1.2 can be rewritten as follows:

$$\frac{I}{I_0} = \exp(-\sigma\rho l) \implies \ln I_0 - \ln I = \sigma\rho l$$

Finally, we have: $\rho = \frac{\ln I_0 - \ln I}{\sigma\rho l}$ (6.1.3)

Substituting the values of I and I_0 into expression (6.1.3) gives the density of oxygen in the light path.

$$\rho = \frac{\ln(1.00324) - \ln(0.29788)}{2.5 \times 10^{-17} \times 200} = 2.428 \times 10^{14} \text{ molecules cm}^{-3} \quad (6.1.4)$$

Using Avogadro's law, the density ρ can be expressed in terms of moles cm^{-3} as follows :

$$\rho = \frac{2.428 \times 10^{20} \text{ m}^{-3}}{6.02 \times 10^{23} \text{ mol}^{-1}} = 4.0 \times 10^{-4} \text{ mol m}^{-3} \quad (6.1.5)$$

Expression (6.1.5) gives the density of oxygen in the light path per unit of volume.

From the Ideal gas law, the pressure can be expressed in terms of density of the oxygen:

$$P_{O_2} = \rho \cdot R \cdot T, \quad (6.1.6)$$

where $T = 293.15 \text{ K}$ and $R = 8.3144621 \text{ J mol}^{-1}\text{K}^{-1}$ are the room temperature and the ideal gas constant, respectively.

Substituting the values of R and T in the equation (6.1.6) gives the pressure of the oxygen in the path light.

$$P_{O_2} = 4.0 \times 10^{-4} \times 8.3144 \text{ JK}^{-1} \text{ mol}^{-1} \times 293.15 = 0.97 \text{ Pa} \quad (6.1.7)$$

So, the pressure of oxygen in the path of the light is $P_{O_2} = 0.97 \text{ Pa}$ and the pressure of the nitrogen P_{N_2} within the spectrometer is $1.013 \times 10^5 \text{ Pa}$.

According to the Dalton's Law of Partial Pressure, the concentration of oxygen in the path of the light can be calculated as follows:

$$C_{iO_2} = \frac{P_{O_2}}{P_{N_2}}, \quad (6.1.8)$$

where C_{iO_2} represents the concentration of the oxygen expressed in ppm (parts per million).

Therefore, equation (6.1.8) gives $C_{\text{iO}_2} = 9.6$ ppm which is approximately the concentration of oxygen in the nitrogen 5.0 within the monochromator based in the measurements. According to the specifications of nitrogen (see Table 6.2), the 9.6 ppm of oxygen found in the light path is greater than the amount of oxygen impurity ($\gg 2$ ppm) contained in the nitrogen 5.0. This tells us that there is still some oxygen impurities in the spectrometer even after the spectrometer was evacuated for several hours and purged with N_2 for 45 min. Note: if the vacuum system was open to air before the air molecules are adsorbed to its walls. Pumping does not remove these. During purging with nitrogen the oxygen that is adsorbed to the walls is constantly outgassing and this way increasing the impurities in the nitrogen.

6.1.5 Change of lamp intensity over time

As mentioned earlier, when a contaminated optics is exposed for long times to an intense VUV radiation, this contaminant becomes fixed to the optics surface and contributed to the degradation in the transmission or reflectance of this optics.

This is observed using the Model 632 Deuterium lamp. Since it has a magnesium fluoride front window and contaminants, such as out-gassing from the wall or silicone oils used to lubricate mechanisms which accumulate on the outside surface of the window over time. This leads to the degradation of the lamp output which is often severe in the short wavelength range and becomes weak, and therefore impossible to be used.

The decrease of lamp intensity over time can be visualised in Figure 6.14 where the deuterium lamp spectra measured during an interval of a month are plotted.

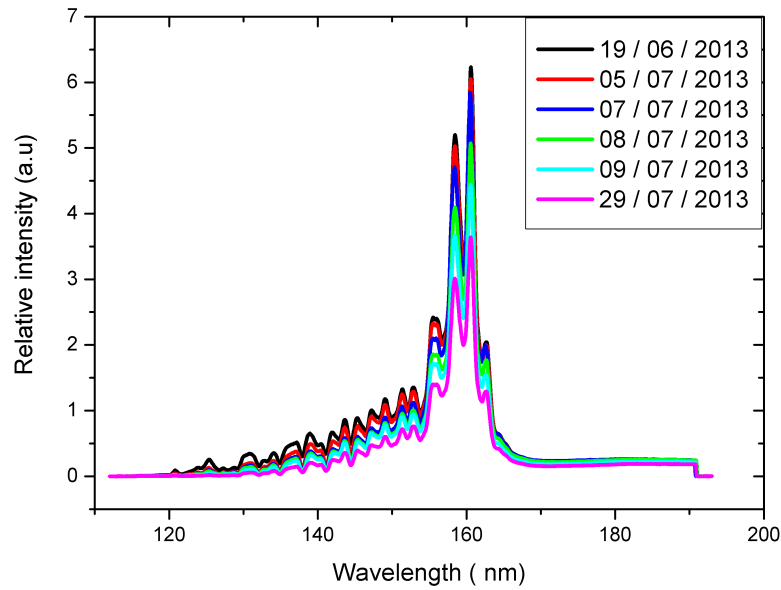


Figure 6.14: *Decrease of lamp intensity over time.*

The labels on Figure 6.14 are the dates on which these spectra were measured. It can be seen that the lamp output decreases over time due to the accumulation of contaminants on the outside surface of the magnesium fluoride window of the lamp. This decrease of the output signal is about 90 percent for the shorter wavelengths (125 nm) and 20 percent for longer wavelengths (170 nm) over a month as seen in Figure 6.15.

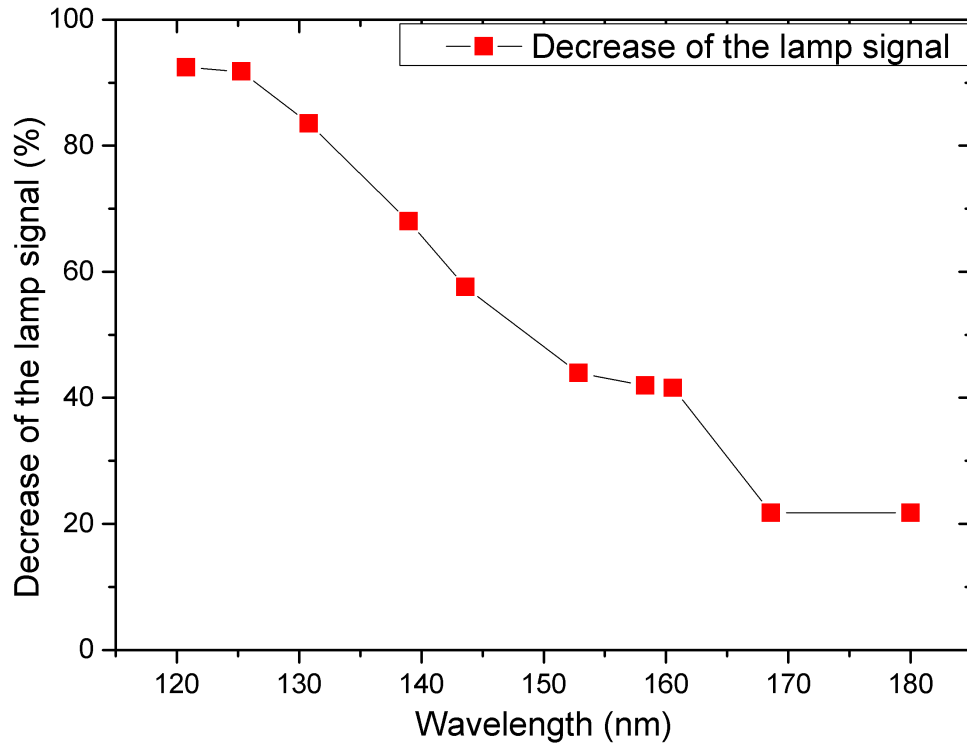


Figure 6.15: *Decrease of lamp intensity over time over a month.*

The problem of accumulation of contaminants on the outside surface of the lamp window can be avoided either by setting up the source with a small flow of pure argon to buffer the outside surface of the window and a differential pumping system between the lamp and the vacuum system [27], or the contaminants can be removed by polishing the outside of the windows. The second possibility was chosen for this work. The magnesium fluoride window of our deuterium lamp was cleaned by polishing with polishing powder and flushed with ethanol. Thereafter, a new alignment was made in order to optimize the output signal.

Figure 6.16 shows three spectra in which the first is the spectrum recorded when we started our investigation, the second and the third are the spectrum measured before and after cleaning, respectively.

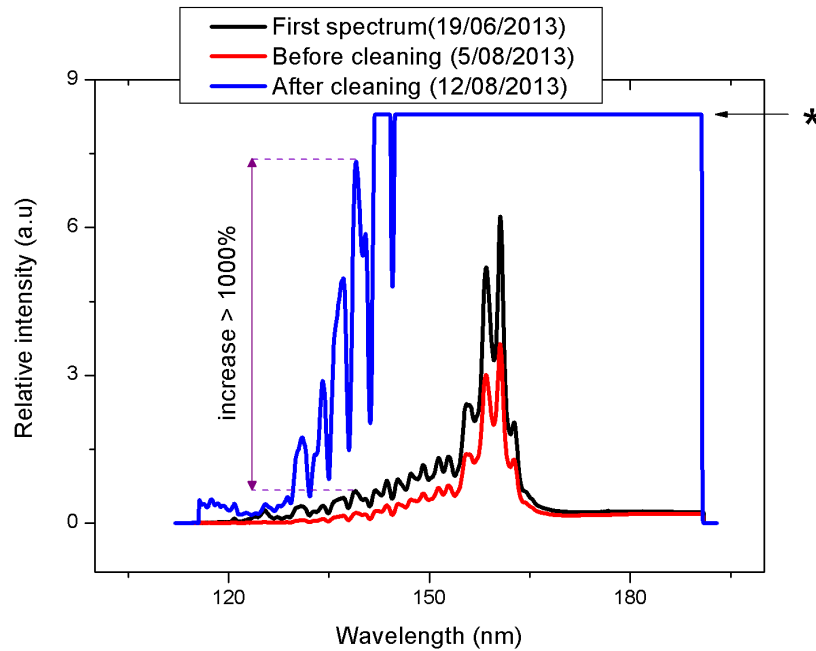


Figure 6.16: *Decrease of lamp intensity over time and the effect of window cleaning. The horizontal line at * is due to the signal being larger than the upper limit of the analogue to digital converter*

The lamp intensity obtained after cleaning the lamp was higher by several orders of magnitude so that for the same experimental conditions (same entrance and exit slit and amplification of signal) the spectrum recorded after cleaning was above the upper limit of the analogue to digital converter. This increase in the output of the lamp can be quantified by considering for example the intensity of the signal at 139 nm. We can observe that the intensity at 139 nm increased by a factor of 11.29 and it can be estimate over 1000 percent increase relative to the intensity before cleaning.

6.2 Measurement procedures and data processing with the monochromator

In this section we will be discussing how the measurements were done and the processing which were performed on the measurements in order to calculate absorption spectra (absorption vs wavelength) from the measured intensity spectra.

6.2.1 Measurement procedure with a gas purged sample cell

In preparation for measurements the monochromator was evacuated continuously. The cell was evacuated briefly and then continuously purged with nitrogen having through the cell.

The measurements process started once the pressure in the monochromator reached approximately 8.5×10^{-6} mbar and the sample cell was sufficiently purged with the nitrogen for 45 minutes.

First of all two spectra are measured successively with an empty sample cell, i.e, without any samples in the light path (see appendix for more details). This is done one after the other with all settings exactly the same. Thereafter, the sample is inserted into the cell and two other measurements are taken with the sample. At the end, we record the last two spectra after having removed the sample from the cell. The empty-cell measurement at the end is a safety measure that shows if anything changed with time during the measurements. At the start and end of each measurement, a dark-background measurement is done by closing a valve in the monochromator to block all the light. The dark-background is subtracted from the measurement.

The absorbance can be calculated by using well-known Beer-Lambert law as follows :

$$A = \log(I_0/I) \quad (6.2.1)$$

where I and I_0 are respectively the intensity of the lamp spectrum taken with and without sample in the light path.

An example of two spectra taken with and without sample in the light path is shown in Figure 6.17.

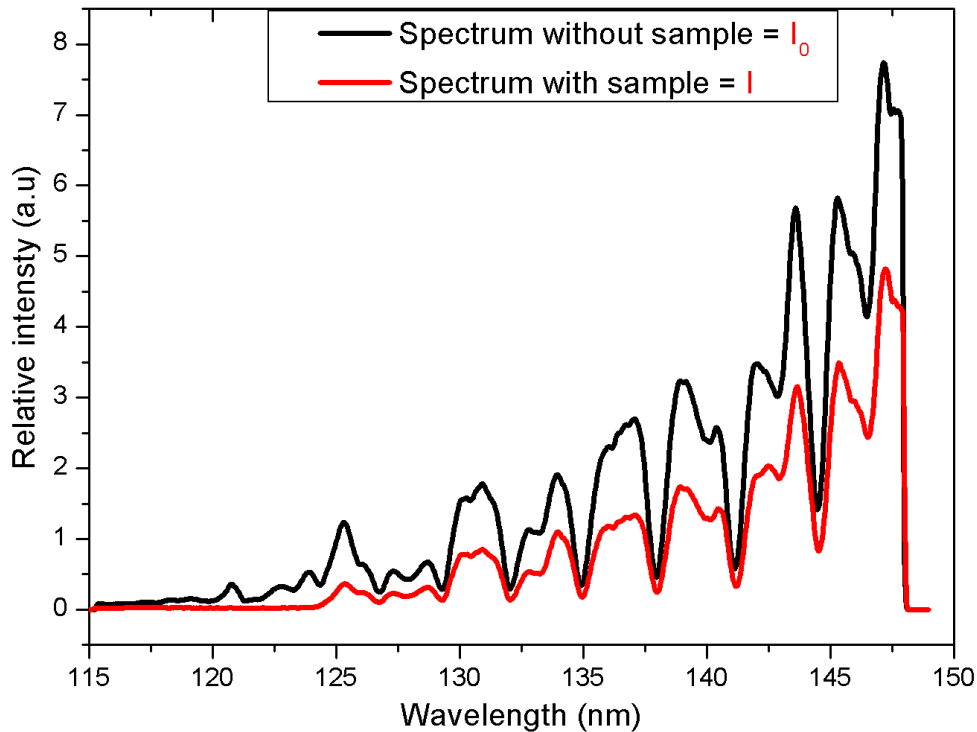


Figure 6.17: Example of two deuterium lamp spectra (115-150 nm) measured with and without the sample in the light path.

6.2.2 Measurement procedure with an evacuated sample cell

All spectra were recorded when the pressure into the monochromator was approximately at 8.5×10^{-6} mbar, while the pressure into sample cell was at 3×10^{-6} mbar. The spectra were recorded as follows: first, we are measuring successively two spectra with an empty sample cell. This is done one after the other with all settings exactly the same. Thereafter, the sample is inserted into the cell and two other measurements are taken with the sample. At the end, we record the last two spectra after having removed the sample from the cell. At the start and end of each measurement a dark-background measurement is done by closing a valve in the monochromator to block all the light.

The calculation of the absorbance is performed by using equation (6.2.1). However, as the pressure in the monochromator and the sample cell keep on decreasing slowly during the measurements, the second one of each pair of measurements were chosen in the calculations of the absorbance.

6.2.3 Calibration of the wavelength scale

Due to mechanical reasons, wavelength scans done with exactly the same settings do not cover exactly the same wavelength range. Therefore, when the uncalibrated spectra are compared peaks of the recorded spectra do not seem to occur at exactly the same wavelengths (see Figure 6.18). Therefore, a careful refinement of the wavelength scale of all graphs is necessary before further analysis (calculation of the absorbance). To achieve this, it is necessary to consider one specific spectrum as standard spectrum and then use it for calibration of all other spectra. In this thesis, a spectrum of the output of the Deuterium lamp model 632 obtained from McPherson was used as standard spectrum for the calibration of the wavelength scale of all our experimental spectra.

To illustrate the calibration process, let us assume that spectrum A is our standard spectrum and we want to recalibrate spectrum B. This is done by following these above steps.

1. Plot each spectrum separately and determine the wavelengths of its peaks.
2. Plot a graph where the X-axis is the peak wavelengths of the spectra that need to be calibrated (spectrum B) while the Y-axis is the peak wavelengths of the standard spectrum (spectrum A). Do a linear fit to this graph.
3. use the equation $Y = C + M \times X$ from the linear fit to calibrate the spectrum B, where X is the original wavelength of spectrum B, Y is the calibrated wavelength for B. C and M are intercept and gradient of the linear fit, respectively.

Plotting now A and B on the same graph with the new B-wavelengths. The peaks should be exactly at the same wavelengths.

An example of deuterium lamp spectra before and after the calibration of wavelengths scale was performed is shown in Figure 6.18.

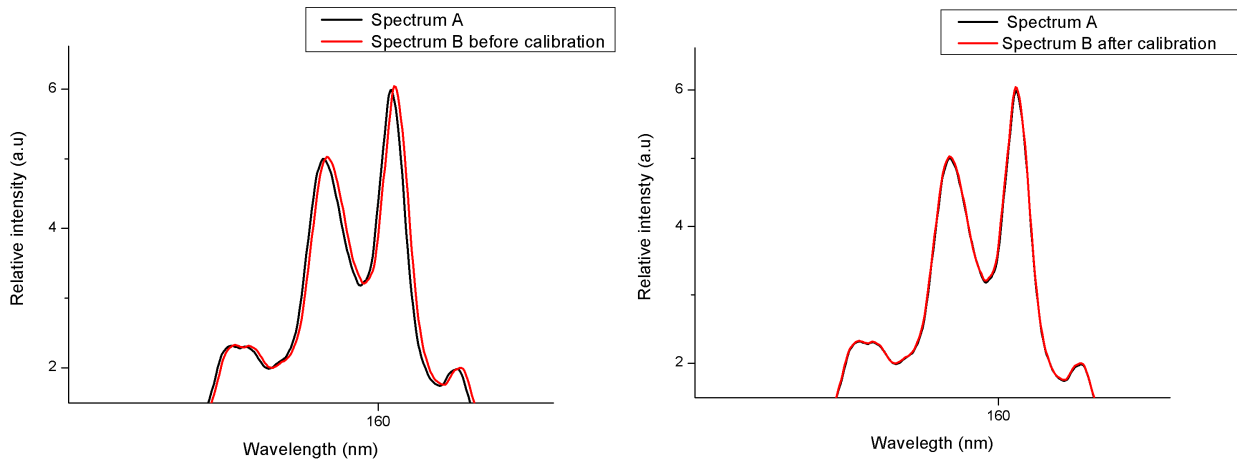


Figure 6.18: A small part of spectra A and B. Before (left hand side) calibration and after (right hand side) of B relative to A.

6.2.4 Interpolation

The re-calibration of the wavelengths scales of all the experimental spectra leads to the change of the wavelengths of the data points for each spectrum. This makes the data analysis difficult: it becomes complicated to calculate the absorbance of each wavelength due to the fact that the data points of different spectra are not longer at the same wavelengths as illustrated in the left graph of Figure 6.19. Therefore, an interpolation of the spectra is necessary in order to have the spectra in which each data point should match to the corresponding data point in others spectra as illustrated in the right graph of Figure 6.19.

The interpolation was done with more data points than the initial spectra in order to not reduce the resolution. The number of data points was obtained using the following formula:

$$\frac{X_{\max} - X_{\min}}{0.04}$$

where X_{\max} and X_{\min} are respectively the maximum and the minimum wavelength of the initial spectrum. The factor 0.04 is the interval between the interpolated data points in nanometre. The interval between data points in the original measurement was typically 0.043 nm.

A typical example of data points before and after interpolation is shown in Figure 6.19.

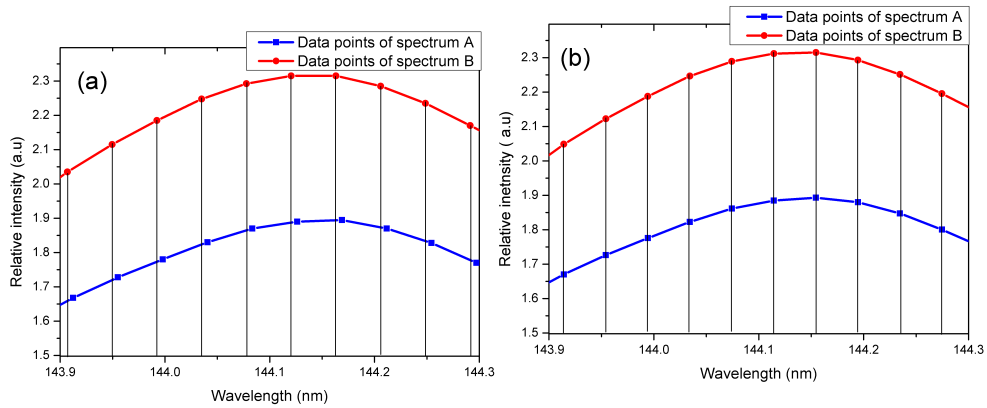


Figure 6.19: Illustration of data points of two spectra before (a) and after (b) interpolation.

The graph (a) in Figure 6.19 shows the example of data points of two spectra before interpolation, it can be observed that the wavelengths of the data points of spectrum A do not match with the data points of spectrum B. In graph (b) of Figure 6.19 we can now see the effect of the interpolation on the data points. These two spectra now have their data points at approximately the same wavelengths. This allows us to calculate the absorbance easily for each wavelength.

6.3 Absorption spectra of CaF_2 using the monochromator

In this section, the results of our investigation on the absorption spectroscopy of calcium fluoride samples is presented. Seven samples ($25 \times 25 \times 100 \text{ mm}^3$) were used. The descriptions given below were provided by the manufacturer (Schott Lithotech AG, Jena, Germany) and refers to the fluorescence emission spectrum when the sample is excited by UV laser light.

1. Sample A : A pure calcium fluoride crystal which emits fluorescence at 278 nm, the characteristic fluorescence of STE's.
2. Sample B : A sample containing *Na* and has a fluorescence emission peak at 740 nm.
3. Sample C : A sample containing *Na* and has a fluorescence emission at 740 nm.
4. Sample D : A fluorescence of the sample shows a double peak at unknown wavelengths.
5. Sample E : A sample doped by Pb and has a fluorescence emission peaks at 225 and 796 nm when excited at 157 nm.
6. Sample F : A sample doped by Pb which has its fluorescence emission at 225 nm and it excited at 157 nm.
7. Sample G : A sample which has a fluorescence emission peak at 450 nm.

6.3.1 Effect of oxygen absorption on the measurement

The calculation performed in the previous section 6.1.4 about the possible concentration of oxygen in the nitrogen 5.0 within the monochromator shows that even though the sample cell is evacuated and thereafter flushed with nitrogen 5.0, there is still some residual oxygen impurities in the path length. In this section, the effect of this oxygen impurity on the measurements and how it can be suppressed will be discussed.

The concentration of the residual oxygen in the path length was calculated as equal to = 9.6 ppm. Nevertheless, this small amount of oxygen can influence the experimental results negatively. This can be visualised in Figure 6.20 where absorbance is calculated using equation (6.2.1).

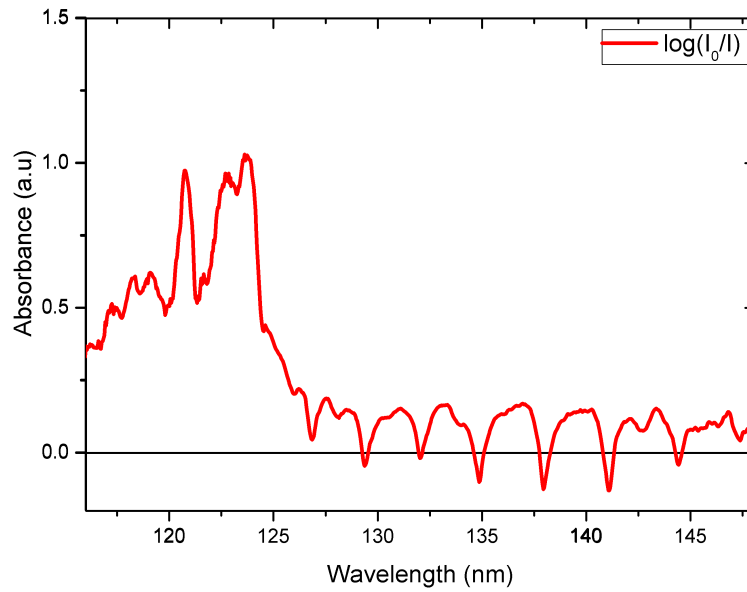


Figure 6.20: Absorption spectrum of the pure calcium fluoride sample (sample A) in the VUV range

Figure 6.20 shows clearly a structure in the range of 115-125 nm. The origin of this band structure will be discussed in section the 6.3.3.

The absorption features from 125 nm to 145 nm correspond to the characteristics peaks of the oxygen absorption in VUV range. This is verified in Figure 6.21 where the absorption spectrum of a pure calcium fluoride sample is superposed with the peaks of Figure 6.13 that shows the oxygen absorption in the VUV range.

This comparison shows that the absorption features observed at 125-145 nm range in the absorption spectrum is caused by the residual molecular oxygen in optical path. The subsequent question is how the effect of this residual oxygen absorption can be suppressed in the measurements. This can be done by looking at the amount of oxygen in the light path.

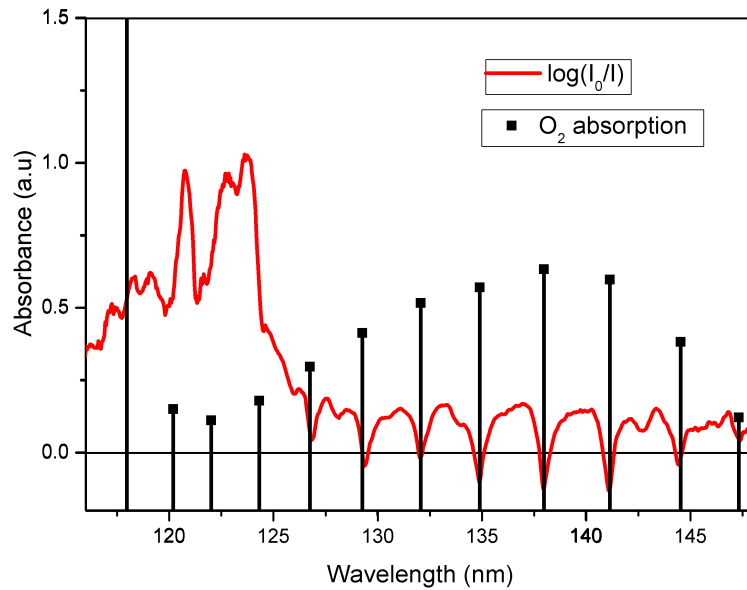


Figure 6.21: Superposition of the absorption spectrum of the pure calcium fluoride sample (sample A) with the graph which contains peaks of oxygen absorption in the VUV range.

It has been shown (equation 6.1.3) that the oxygen absorption in a spectrum depends on the path length of the light through the gas. Crystalline calcium fluoride samples used for this study are 100 mm long. When a sample is inserted the path length of the light through the gas is 100 mm shorter. Therefore spectrum I_o (without sample) shows more O_2 absorption than spectrum I (spectrum taken with sample). So, in the calculation of the absorbance (equation 6.2.1) where the ratio of the spectra taken with and without the sample is calculated, it is expected to observe these absorption features. The reason of that is the amount of oxygen in the light path is not equal for the two spectra.

Therefore, it is necessary to balance the amount oxygen absorption in the spectra (with and without sample) in order to reduce the effect of oxygen absorption in the absorbance. To achieve this, an extra vacuum tube which has exactly the same length as the sample, should be added before the detector when the sample is inserted in the light path. When this is done, the path lengths of the light in the gas are equal for a measurement with and without sample and therefore the effect of the oxygen absorption in the absorption spectra is directly reduced. This can be visualized in Figure 6.22 where the absorption spectra measured with and without adding the extra tube are plotted.

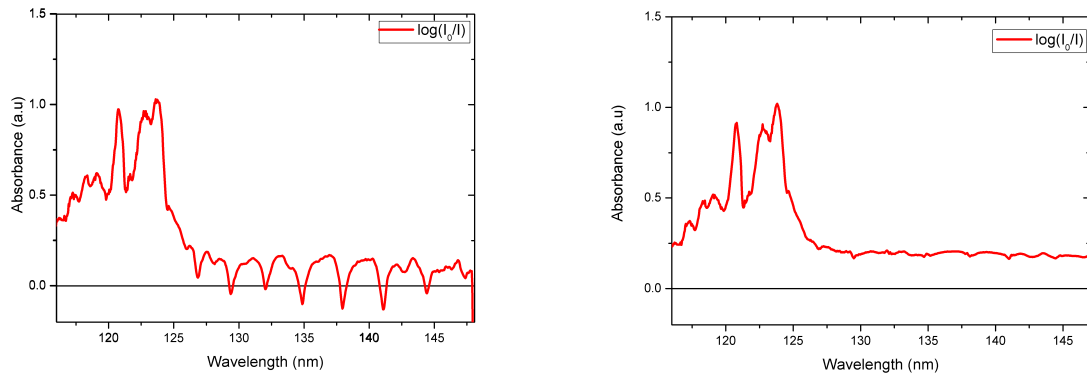


Figure 6.22: Illustration of two absorption spectra of a same CaF_2 sample measured with (right hand side) and without (left hand side) the extra tube.

6.3.2 Absorption measurements of CaF_2 samples in 130-180 nm range

Two sets of absorption spectra of CaF_2 samples in the 130-180 nm range are reported here. Firstly, the spectra of the measurements recorded with a setup in which the sample cell is purged with 1 bar nitrogen are presented. These spectra were taken without the extra tube that reduces the effect of oxygen absorption. Secondly, the absorption spectra of CaF_2 samples recorded with the sample cell under vacuum are presented. These measurements were done with the same entrance and exit slit set at $600 \mu\text{m}$. But the high voltage (HV) on the PMT was different. The first set of measurements was recorded with high voltage set -1500V while for the second set of measurements the high voltage was set at -1100V . The amplification factor for the PMT signal was 10^5 .

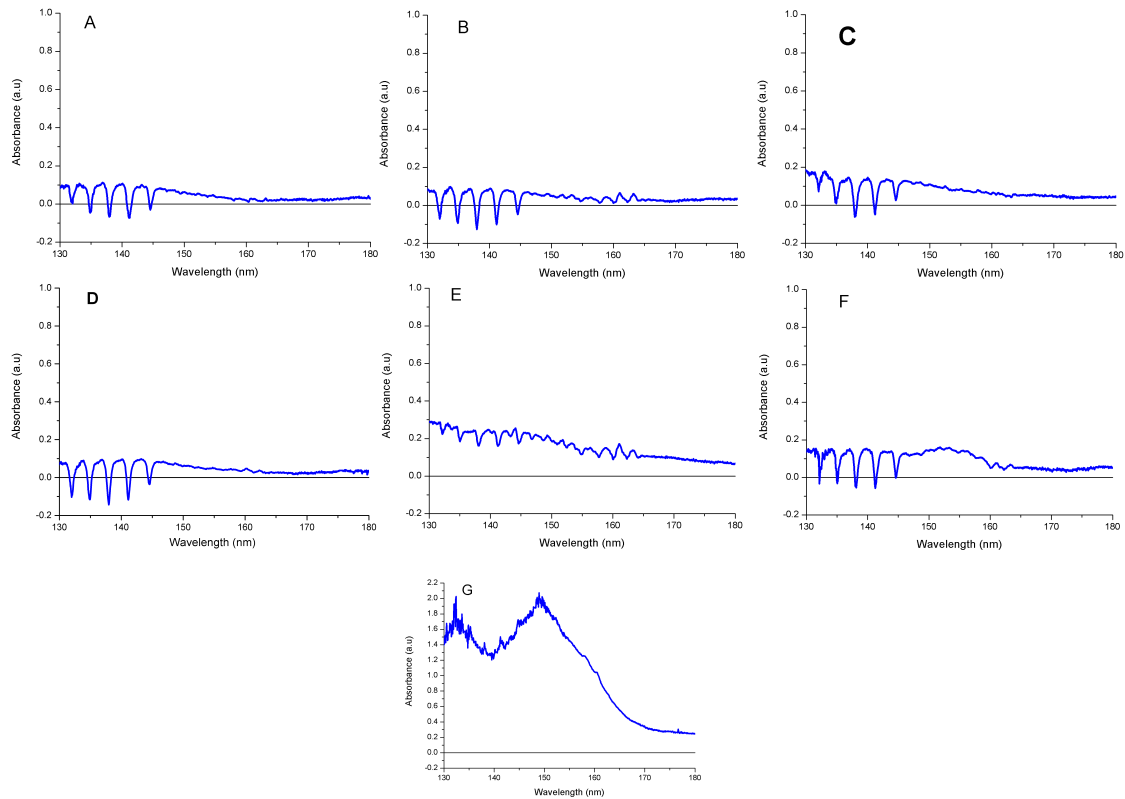
6.3. Absorption spectra of CaF_2 using the monochromator6.3.2.1 Absorption measurements of CaF_2 samples recorded with sample cell purge with 1 bar nitrogen 5.0

Figure 6.23: Absorption measurements (130-180 nm) of pure and doped calcium fluoride samples recorded with sample cell purge with 1 bar nitrogen 5.0. The spectra were taken without the use of the extra tube to keep the optical path length in the gas the same. The graphs are label by the sample labels A-G. For the larger graph see appendix A.1.0.2.

In Figure 6.23, observed absorption features in each spectrum around 130-150 nm is observed. These absorption structures should be attributed to the molecular oxygen present in the nitrogen and from the out-gassing within the monochromator and sample cell.

Absorption caused by the molecular oxygen can be suppressed by adding an extra tube (same length as the sample) during the measurement taken with sample in the beam path (see section 6.3.1). However, the measurements resulting in Figure 6.23 were done without using the extra tube.

Despite the oxygen absorption, characteristic features of the sample are observed. Samples A, B, C and D have similar spectra. It can be deduced that sample D may also be a sample containing Na as impurity. The lead doped samples E and F show similar spectra broad

6.3. Absorption spectra of CaF_2 using the monochromator

absorption feature at approximately 155 nm. Sample G shows a stronger absorption than others sample in the range 130-160 nm.

6.3.2.2 Absorption measurements of pure and doped calcium fluoride samples recorded with sample cell under vacuum

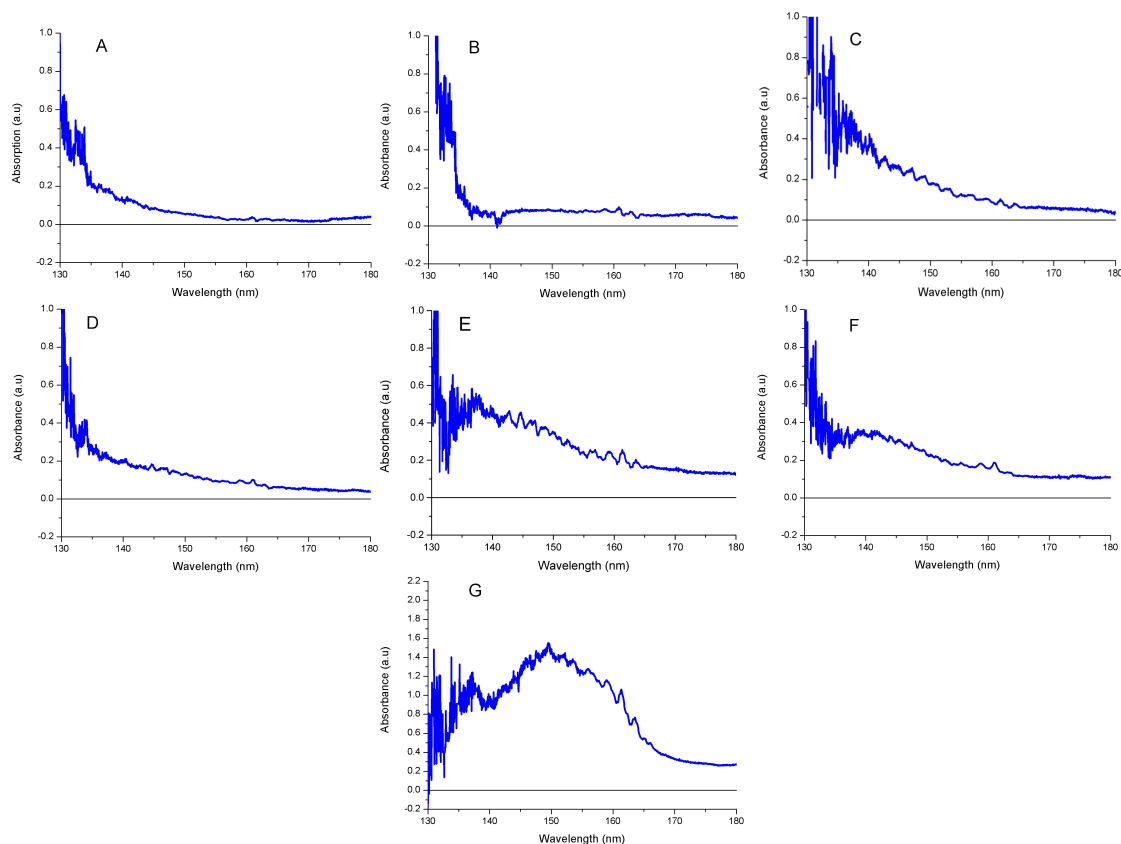


Figure 6.24: Absorption measurements (130-180 nm) of CaF_2 samples recorded with sample cell under vacuum. The graphs are labeled by the sample labels A-G. For larger graphs see appendix [A.1.0.3](#).

From the results recorded with sample cell under vacuum, a strong increase of the absorption in all spectrum towards 130 nm can be seen. These increase of absorption is due to the fact that we are approaching band edge of CaF_2 which is around 103 nm.

However the absorbance signal in the range 130-140 nm shows much noise. This is due to the very low intensity of the deuterium lamp in this range that was very close to the detection limit with the PMT high voltage and amplification used. Therefore, the absorbance in the range 130- 140 nm has large uncertainty and the true absorption features cannot be observed.

Looking at the absorption spectrum of all the samples, the following observation can be made:

1. Despite the fact that sample A shows less absorption than sample D, it can be seen that their absorption spectrum are similar.
2. The absorption spectra of sample E and F are also similar as in the measurement recorded with sample cell purge with nitrogen. A broad absorption feature in the range 130 -155 nm is seen with these Pb doped samples. This feature is not in samples A-D.
3. It is difficult to see the similarity in the absorption spectrum of sample B and C (both Na doped samples) since sample B shows less absorption than sample C.
4. As in the previous measurements, sample G shows a much stronger absorption than the other samples. This may be due to high concentration Pb doping, or doping with another impurity.

These observations lead to the conclusion that the absorption features in the 130-180 nm range vary in different samples and this variation correlates with information from the supplier. The spectra in this section were shown only for $\lambda > 130$ nm since the intensity of the deuterium lamp was below the detection limit for shorter wavelengths.

6.3.3 Absorption measurements of CaF_2 samples in 115-130 nm range

Due to the fact that the signal intensity at wavelengths below 140 nm was weak during the previous experiments, it was difficult to see the absorption features close to the band edge. Therefore, to overcome this issue, the outside of the Deuterium lamp window was cleaned (see section 6.1.5). Thereafter, a experiment was performed in the range of 116-130 nm with a stronger light output from the Deuterium lamp. This experiment was carried out with the sample cell purged with the nitrogen. The slit widths were set at 600 μm and the high voltage on the PMT was -1500 V. The amplification factor of the PMT signal was 10^5 .

The results of the absorption measurement of our samples in 116-130 nm range are plotted in Figure 6.25. More details on the spectrum of sample A are shown in Figure 6.26

6.3. Absorption spectra of CaF_2 using the monochromator

74

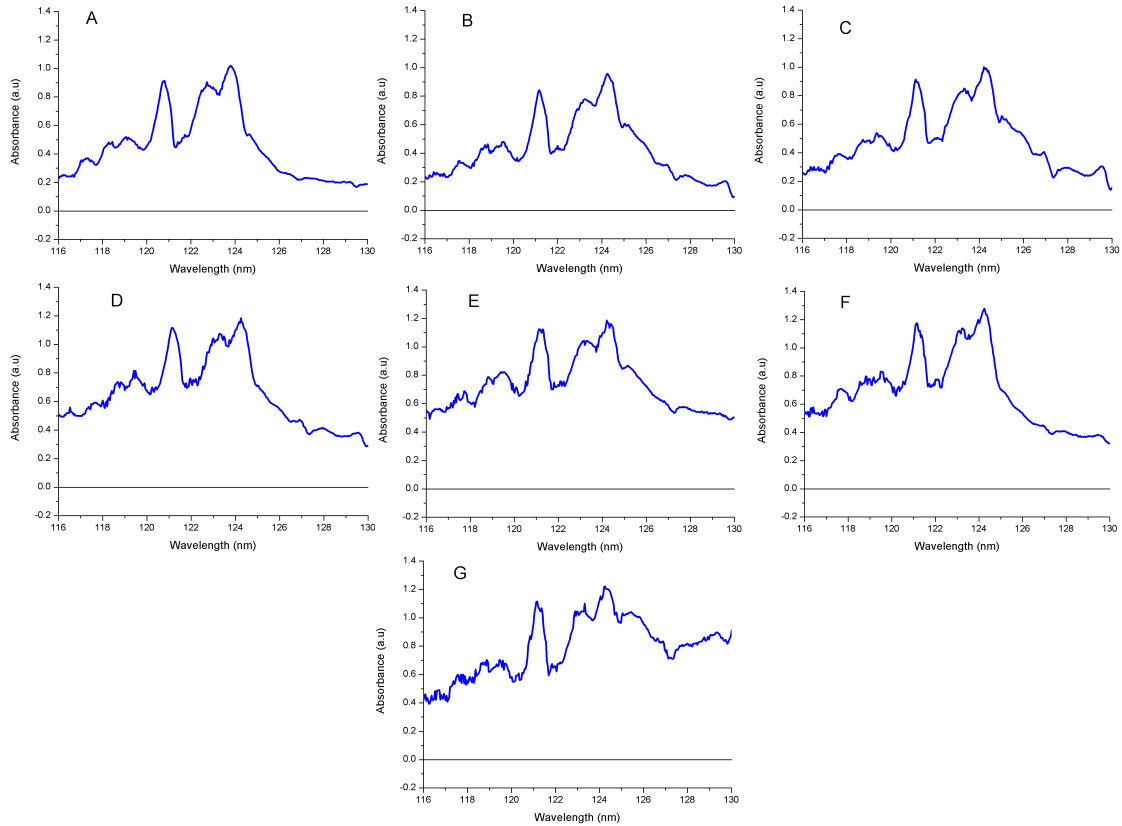


Figure 6.25: Absorption measurements of pure and doped calcium fluoride samples recorded with sample cell purge with 1 bar nitrogen 5.0. Subfigures are labelled with the letters A-G corresponding to labels at samples as on page 6.2.4. For larger graphs see appendix A.1.1.

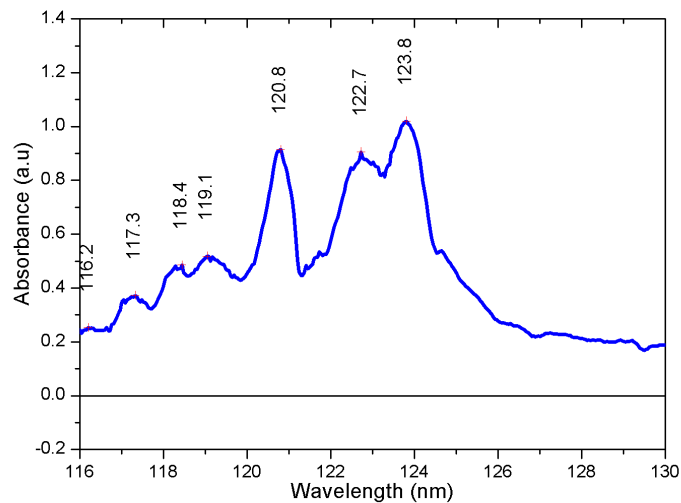


Figure 6.26: Broadband absorption spectra of pure CaF_2 sample (sample A) at the room temperature.

6.3.3.1 Physical reason for peaks at 116-126 nm

In Figure 6.25, five significant absorption features can be observed in all samples. These observed peaks should be due to crystal structure of CaF_2 samples and not to a dopant, since it is observed in each sample. One can also think that these peaks could be caused by molecular oxygen present in the nitrogen and from the out-gassing, since these structures are similar to the vacuum UV spectra of molecular oxygen in this relevant VUV spectral region found by several authors [28, 29, 30, 31]. These two hypotheses lead us to perform a new experiment with the sample cell under high vacuum in order to verify whether these peaks are actually bands absorption of CaF_2 samples or just an absorption due to the residual amount of oxygen from the sample cell and the nitrogen itself.

Sample A was used for this experiment and the result is plotted in Figure 6.27.

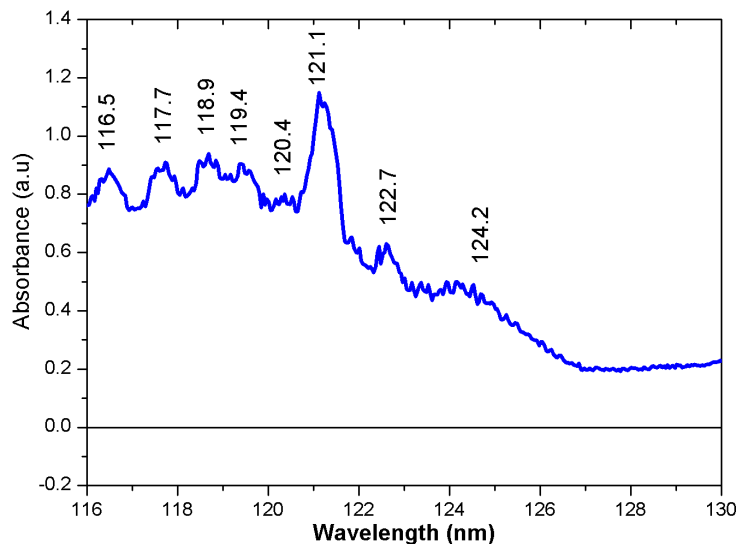


Figure 6.27: Absorption spectra of pure CaF_2 sample (sample A) at the room temperature. Measurement were done with an evacuated sample cell (Pressure: 3×10^{-6} mbar).

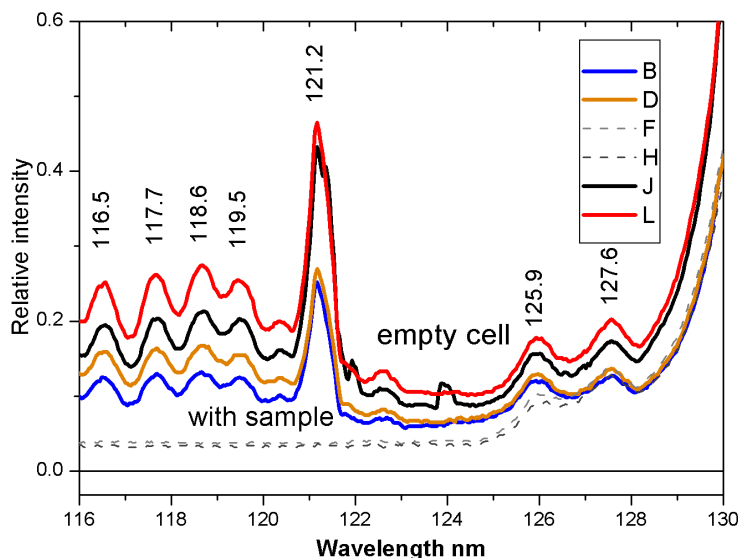


Figure 6.28: Emission spectra of Deuterium lamp in vacuum, recorded with and without CaF_2 sample in the path length. Spectra B and D are two Deuterium lamp spectrum taken with the empty sample cell at the beginning, while spectra F and H are the recorded Deuterium lamp spectrum taken with a pure CaF_2 sample in the path length. Spectra J and L, are respectively the last two measurement taken after removing the sample into the path length.

Figure 6.27 shows strong absorption features below 125 nm as found previously when the sample cell was continuously purged with nitrogen. As before, the wavelengths at the absorption peaks are 116.5, 117.7, 118.7, 121.1, 122.7, 124.7 nm. The relative intensities of the peaks are different from Figure 6.26 as the peaks at 122.7 and 124.7 are less than prominent in the vacuum measurement. However, the fact that we observe the absorption features under vacuum conditions shows that the features are not due to residual Oxygen in the N_2 gas.

The origin of these features are established by carefully looking at Figure 6.28 which shows the intensity spectra that were used to calculate the absorbance in Figure 6.27. Comparing the lamp spectra taken with and without sample, one notices that the sample transmits a constant but non-zero light intensity in the range 115 -125 nm. Therefore, the absorption features observed in figure 6.27 represent only the peaks characteristic of Deuterium lamp emission in this range. This can be verified by comparing several peaks on Figure 6.28 to the peaks on Figure 6.27. These peaks have approximately the same wavelengths.

The subsequent question is why the sample transmits a non-zero but constant light intensity in the 115- 125 nm range? Our conclusion is that calcium fluoride samples absorbs practically all the vacuum ultraviolet light in the 115-125 nm range. This in agreement with

the optical manufacturers' literature [32, 33]. If the incident light from the monochromator onto the sample was monochromatic vacuum ultraviolet light, we expected the transmission of VUV light through the sample to be zero in this range. However, this is not the case.

The non-zero constant sample transmission in the 115 -125 nm range can be explained by assuming that light transmitted by the monochromator consists of monochromatic vacuum ultraviolet light together with a background of broadband light.

The imperfections in the shape and spacing of the grooves and roughness on the surface of the grating cause scattering of light other than the wavelength of interest. This is called instrumental stray light. This stray light passes through the exit slit of the monochromator in addition to the desired wavelength [7].

The fact that the stray light is present in the output of the monochromator, can lead to the wrong interpretation of the measurement. Therefore, it is necessary to suppress it in all recorded measurements. This can be done by subtracting the average of the stray light intensity in the region 115-125 nm from the measured intensity of each spectrum.

A typical example of spectra where the stray light is suppressed is shown in the Figure 6.29.

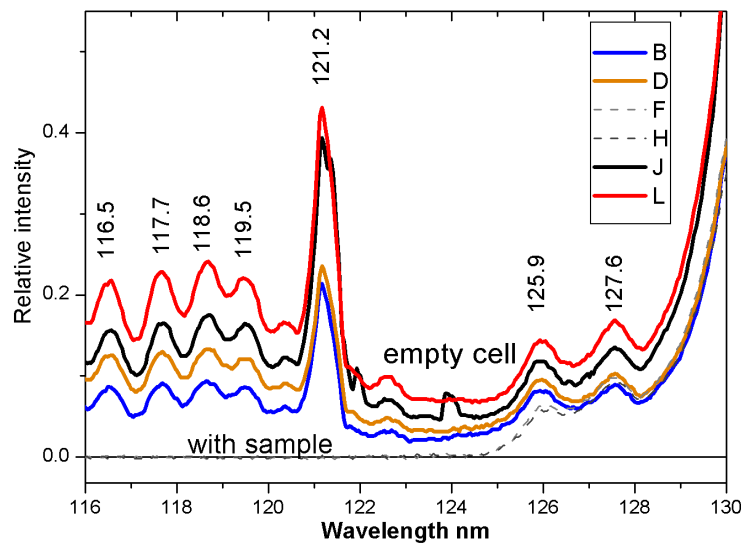


Figure 6.29: Emission spectra of Deuterium lamp with and without sample after subtracting the average intensity of the stray light in the range 115-125 nm from all the data sets.

Figure 6.29 above represents the spectra of sample A plotted previously in the Figure 6.27 but now the light background due to the stray light has been subtracted. It is clearly seen

now that the calcium fluoride sample absorb all the light below 125 nm as reported in the literature. The absorbance of sample A is plotted now in Figure 6.29, using the spectra in which the stray light background has been subtracted.

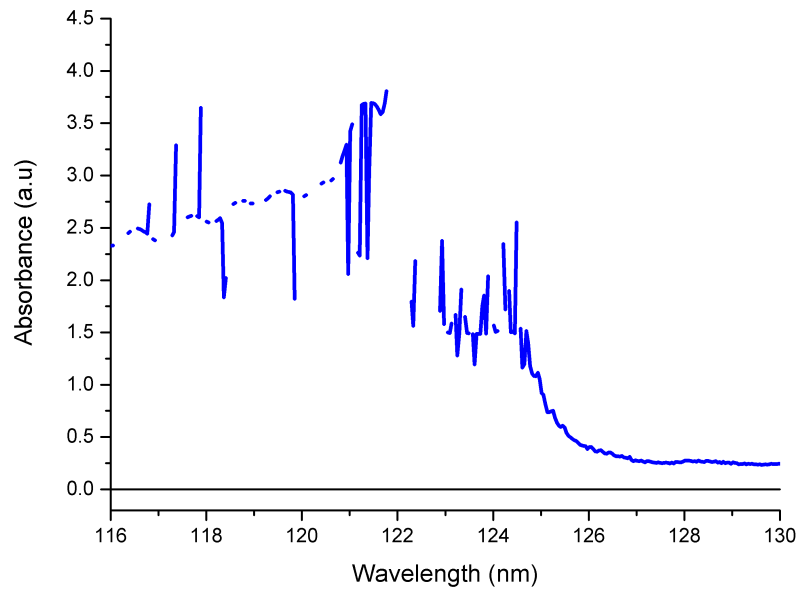


Figure 6.30: Room temperature absorption spectra of pure CaF_2 .

This is the true absorbance spectrum of CaF_2 . The artifacts due to the lamp emission and light background are gone. Absorption increases gradually towards the short wavelengths. Below 125 nm sample transmits too little light to allow detection and absorbance values below 125 nm are not accurate. This is an agreement with the literature that reports sharp rises in absorption at 125 nm.

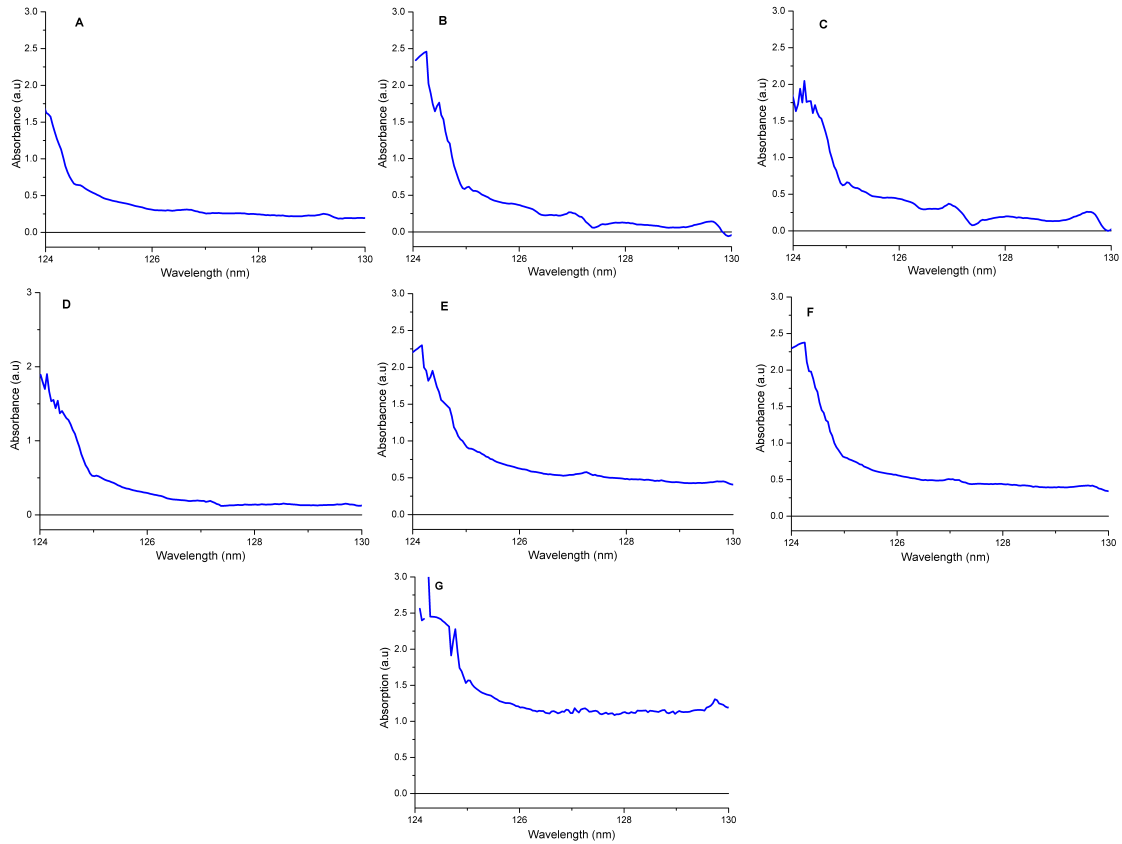


Figure 6.31: True absorption spectra of pure and doped calcium fluoride samples recorded with sample cell purge with 1 bar nitrogen 5.0. Subfigures are labelled with the letters A-G corresponding to labels at samples as on page 6.2.4. For large graphs see appendix A.1.1.1.

Figure 6.31 shows the true absorption spectra of all CaF_2 crystals used in this study. No absorption features are observed that could be due to the STE states. This was expected since the intensity of a discharge lamp is not high enough to allow significant two-photon absorption that can excite electrons into the conduction band leading to the formation of STE states in the band gap.

6.4 Characterisation of the VUV laser source

The two-photon resonance in magnesium vapour and a correct krypton magnesium pressure ratio in the medium for phase matching are the most important conditions that must be met observing any output VUV light in the heat pipe.

6.4.1 Effect of two-photon resonance

It has been discussed theoretically in section 2.2 how the susceptibility of sum frequency generation can be enhanced by minimizing the denominator of equation (2.2.1). This is achieved experimentally by turning the incident beams sufficiently close to the resonance. The wavelength transition of the two-photon absorption in a magnesium vapour is about 430.889 nm. The effect of the resonance enhancement can be seen by blocking the beam from dye laser I (see section 5.2, Figure 5.5) while dye laser II is tuned continuously from 430.5 to 431 nm. The typical experimental curve of the resonance is shown in Figure 6.32.

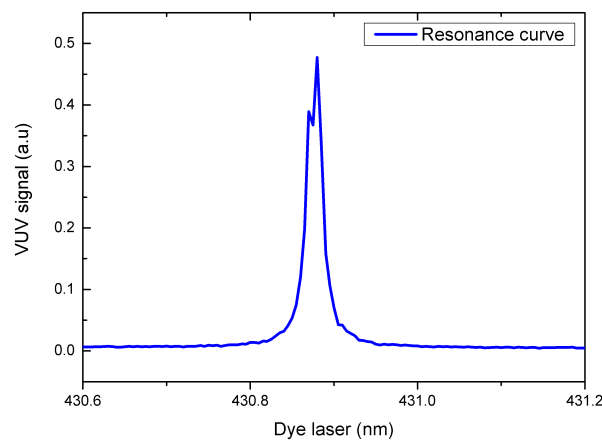


Figure 6.32: *Resonance curve of the third harmonic generation*

Figure 6.32 shows how the intensity of the generated third harmonic light can be enhanced when the incident beams are tuned close to the resonance. The VUV signal is increased by a factor 13665.7 at the resonance. The increase of the generated VUV signal is due to the fact that at the resonance the denominator of equation (2.2.1) is close to zero and therefore optimizes the value of the susceptibility of the nonlinear medium.

6.4.2 Effect of phase matching

Phase matching is one of the most important conditions for the generation of the VUV light since it is used for suppressing other competing processes and contributes to the efficiency improvement of the intensity of the generated VUV in two component gaseous nonlinear medium. The theoretical part of phase matching has been discussed in section 2.3. In practice phase matching condition is achieved by adjusting the pressure ratio of the magnesium vapour and krypton gas. Figure 6.33 shows an experimental phase matching

curve obtained by keeping the pressure of magnesium vapour in the heat pipe constant while the krypton pressure was adjusted from 21 kPa to 30 kPa in steps of 0.1 kPa. The constant mg pressure was approximately 2.10 kPa.

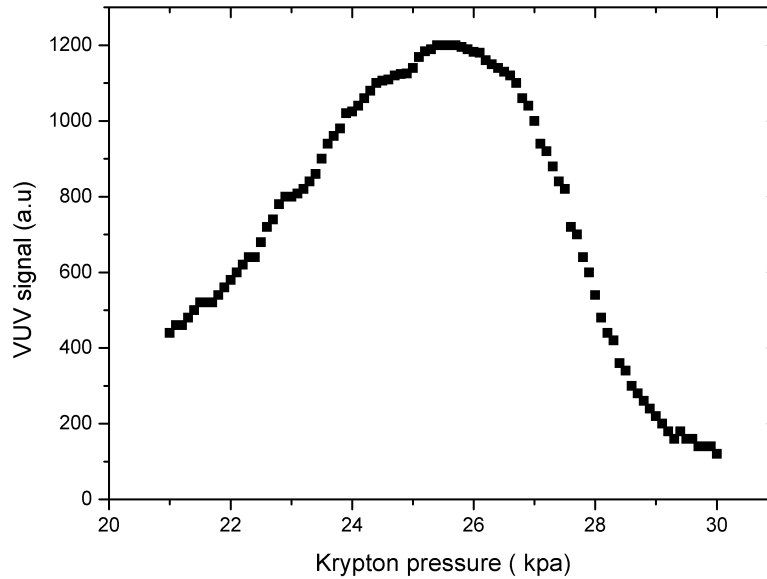


Figure 6.33: *Experimental phase matching curve.*

From Figure 6.33 one can observe that the phase matching of the third harmonic is optimum at 25.65 nm. This corresponds to a ratio $P_{\text{Kr}}/P_{\text{Mg}} \approx 12.2$ compared to a ratio of 12.8 found previously [34]. Theoretically this may correspond to the value of the wave vector mismatch Δk which is approximately zero.

6.4.3 Spectrum of sum-frequency generation

After optimizing the susceptibility of the medium by the resonance and correctly adjusting the magnesium krypton pressure ratio to phase matching, a sum-frequency signal was observed on the oscilloscope. The intensity of the generated sum-frequency was strong enough to be detected by the PMT without using any amplification.

A recorded spectrum of the sum-frequency generated laser light is shown in Figure 6.34. This spectrum was measured when the energy was 2.5 mJ at the dye laser I and 14.5 mJ at dye laser II. The pressure on the krypton gauge was at 25.65 kPa.

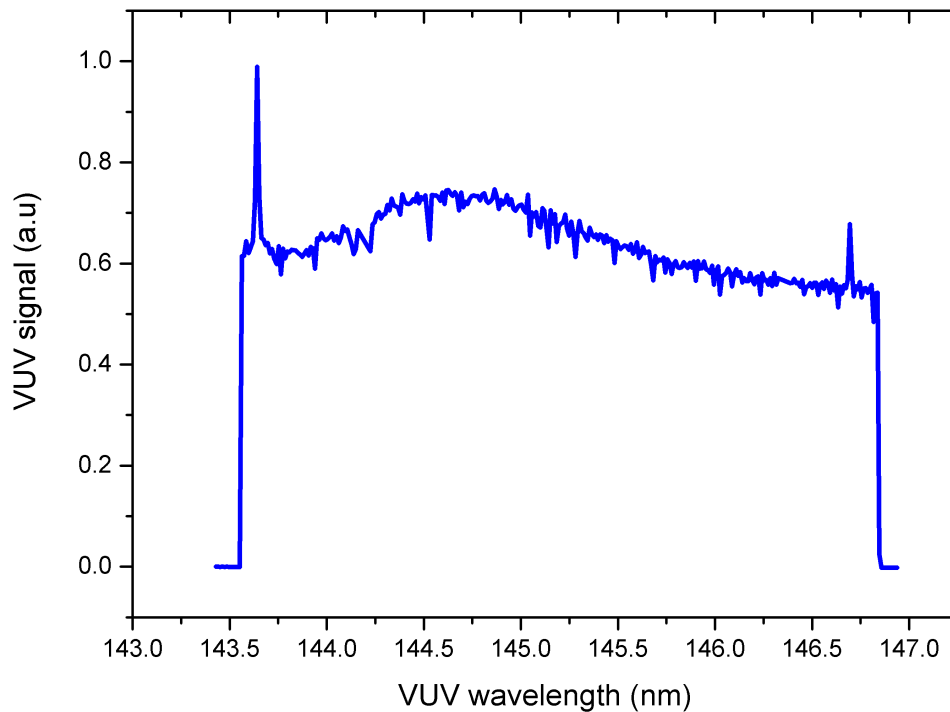


Figure 6.34: *Experimental spectrum of sum-frequency.*

In Figure 6.34 the prominent peak observed at 143.64 nm represents the two-photon resonance in the medium. The full width at half maximum of the peak is 0.0153 nm. Another peak at 146.69 nm was also observed.

6.5 Absorption spectra of CaF_2 using VUV laser source

One of the most important aims of this thesis is to develop the technique to do absorption spectroscopy of CaF_2 samples. An experimental setup was built (see section 5.2) and mounted onto the existing setup for the generation of the tuneable VUV laser light. Two solar blind photomultiplier tubes are used to detect simultaneously the amount of the light split off by beam splitters before and after the sample. The absorbance is calculated using equation 6.2.1. Seven samples were used for this investigation and their descriptions can be found in section 6.2.4.

6.5.1 Sensitivity curves of the photomultiplier tubes

In the absorption spectroscopy it is necessary to investigate the sensitivity of the PMTs before using it. This investigation tells us how the output signal depends on the high voltage

applied to the PMT and it shows how well the PMT is functioning. PMTs (Hamamatsu R6836) used for our absorption spectroscopy with VUV laser source have a high voltage supply ranging from 100 V to 2000 V.

The voltage on the power supplier of the PMTs was varied from 500 V to 2000 V in steps of 100 V and the corresponding signal on the oscilloscope were recorded while keeping the input laser intensities and all other conditions constant. Therefore the VUV light intensity detected by the PMT is constant.

For the two PMTs it can be observed that the recorded signal from 500 V to 800 V is zero. The results are shown in Figure 6.35. We assumed that 800 V could be the photomultiplier detection limit for our generated VUV. However, a linear increase of the PMT signal was observed at 800 V to 2000 V and 1400 V to 2000 V for PMT_1 and PMT_2 respectively. No decrease in the rising slope is seen at higher voltage values, therefore, these PMTs are not saturated by sum-frequency generated signal. It is seen that the output signals of both PMTs are different. This is an indicator of the fact that PMT_2 has lost sensitivity in some voltage range. This can be associated with the aged of the PMT_2 , as PMT_2 is much older than PMT_1 . This presents us with a challenge when it comes to the calculation of the absorbance.

This problem can be solved by using higher HV value for PMT_2 so that the signals are approximately the same and by multiplication of the PMT_2 signal by a normalisation factor. The normalisation factor is determined from measurements as described in the next section.

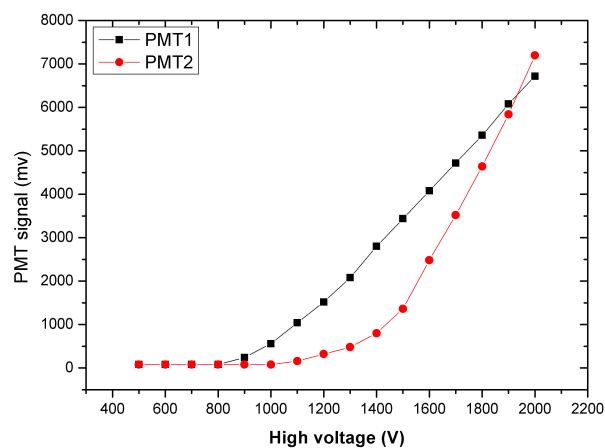


Figure 6.35: Sensitivity curves of PMTs

6.5.2 Data processing of PMT signals

The principal requirement for performing an absorption spectroscopy in which intensities of the incident light and light passing through the sample are measured simultaneously with two detectors is to assure that these two detectors are matched. This requirement demands that the sensitivity of the PMTs to be the same and that there should be an exact equality of the optical path length and equality in the output of signals for both PMTs when no sample is inserted in the light path.

Our experimental setup was designed so that the path length of the light through the vacuum towards both PMTs are equal when the sample is inserted.

The requirement of equality in the output intensity signals of PMTs is achieved by adjusting the PMT high voltage which leads to the changes on the PMT gain. This was done by observing the PMT signal on an oscilloscope. However, even though this is achieved perfectly the recorded output signals are not of equal magnitude (see Figure 6.36). Therefore, an output signal normalisation is needed for both PMTs before doing the absorption measurements of CaF_2 samples.

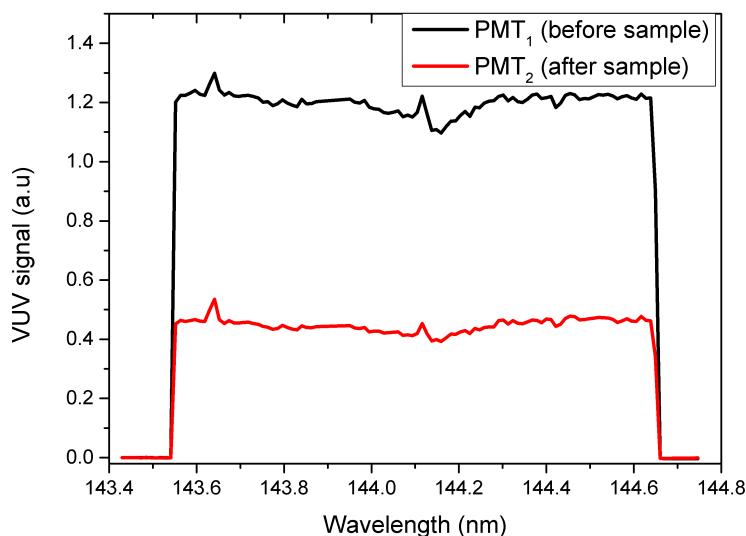


Figure 6.36: VUV light recorded simultaneously with two PMTs without a sample in the evacuated sample cell. This graph shows the difference between signal magnitudes with two PMTs of which the output intensity signals were perfectly adjusted at the same level using an oscilloscope.

The normalisation procedure of the output signals of the PMTs can be done by recording simultaneous spectra of the VUV light over the relevant range without a sample. The ratio of the mean of the data sets recorded with both PMTs is then determined. The second data set (signal recorded with the second PMT) is then multiplied with the mean ratio

to make its magnitude approximately equal to the output signal of the first PMT. Figure 6.36 and 6.37 show the signal of PMTs before and after the normalisation procedure.

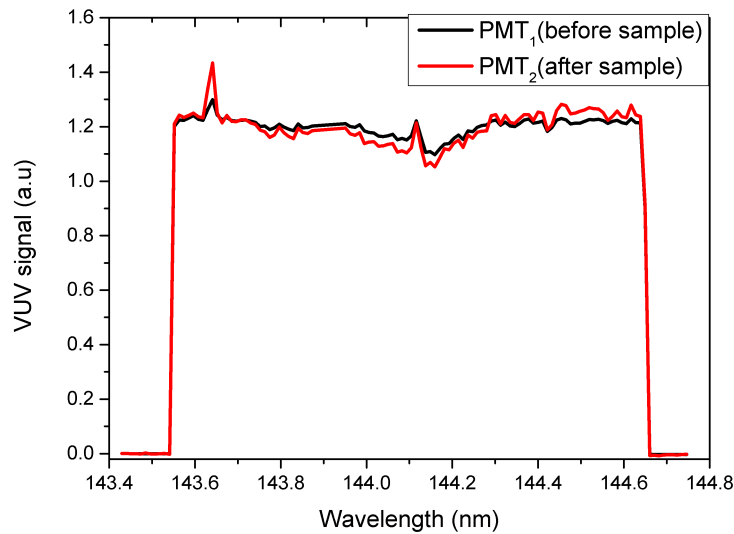


Figure 6.37: Illustration of the PMT signal normalisation. PMT_1 represent a spectrum of sum-frequency generation recorded with the first PMT while PMT_2 is the spectrum recorded with the second PMT multiplied by the normalisation factor (the ration of the mean signal before normalisation).

From Figure 6.37 it can be observed that after performing the normalisation of PMT signals, the spectra of Figure 6.36 have approximately the same intensity signals. This is important for the calculation of absorbance, because this normalisation factor will be used to normalise the output signal of the second PMT when the sample will be inserted in the beam path. Therefore the amount of the light that has been absorbed by the sample could be detected. The illustration in which the PMT normalisation is used in order to calculate the absorbance is shown in Figure 6.38.

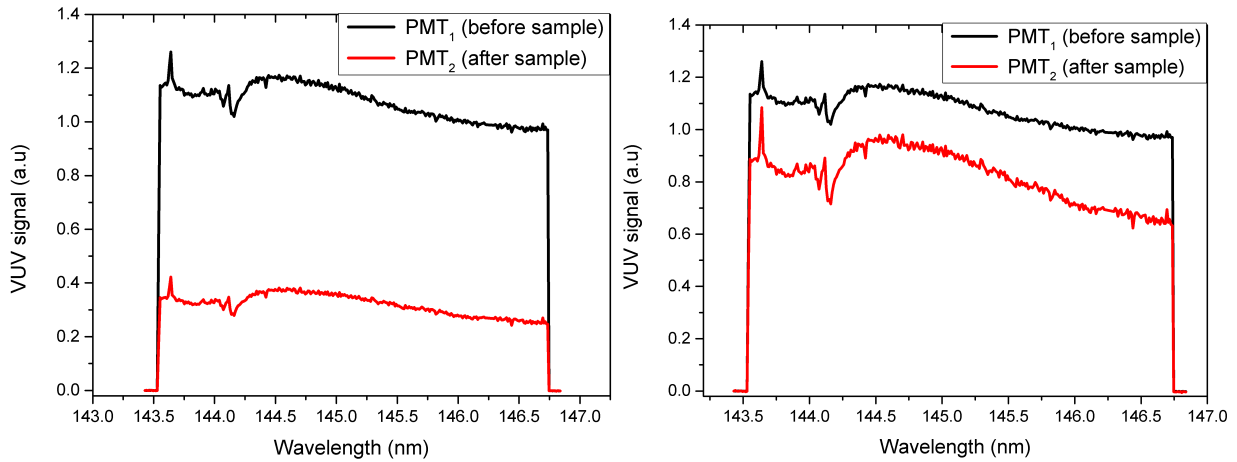


Figure 6.38: VUV spectra of sample *E* before (in left) and after (in right) performing the PMTs normalisation. The normalisation was done with the multiplication factor equal to 2.57.

6.5.3 Measurement procedure of absorption measurement with VUV source

All the measurements are done in the vacuum and its started once the pressure in the sample cell reached $\approx 2.0 \times 10^{-4}$ mbar. First of all two measurements are recorded successively with an empty sample cell. These measurement are used to determine the normalisation factor for the second PMT signals. Thereafter, the sample is inserted into the cell and two other measurements are taken with the sample. At the end, two other measurements are done after having removed the sample from the cell. The empty-cell measurement at the end is a safety measure that shows how much the normalisation factor have been changed with time due to the power decrease of the dye laser. At the start and end of each measurement a dark-background measurement is done by blocking the incident beams before the heat pipe. The dark-background is subtracted from each measurement before the calculation of the absorbance.

6.5.4 Absorption measurements of CaF_2 samples using VUV laser source

The absorption spectra of CaF_2 samples using the generated sum-frequency light is shown in Figures 6.39, 6.40, 6.41. The information related to the samples can be found in section 6.2.4. The experimental conditions for each measurements are given in the Table 6.3.

Samples	HV PMT ₁ (Volt)	HV PMT ₂ (Volt)	Norm.Fact	Dye Laser ₂ Energy(mJ)	Dye Laser ₁ Energy(mJ)
Sample A	-1500	-1600	3.06	10.25	2.6
Sample B	-1300	-1300	6.2	15.7	2.3
Sample C	-1300	-1300	5.73	16	2.32
Sample D	-1500	-1575	3.07	15	2.2
Sample E	-1500	-1600	2.6	14	2.4
Sample F	-1500	-1600	2.65	10	2.2
Sample G	-1500	-1600	3.7	6.1	2.3

Table 6.3: Different experimental conditions used during the VUV laser absorption measurements of samples A-G

In the following Figures (6.39, 6.40, 6.41), the graphs in left hand side are the VUV spectra of the samples after the normalisation process has been performed while the graphs in the right hand side represents the absorption spectra of the samples.

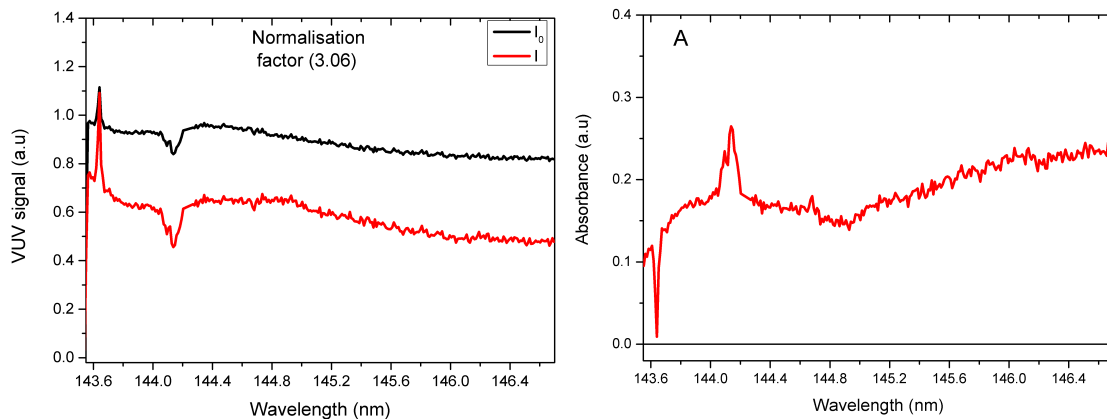


Figure 6.39: Absorption measurements of sample A using the tuneable VUV laser source. Measurements without (I_0) and with sample (I). Absorption spectrum on the right hand side.

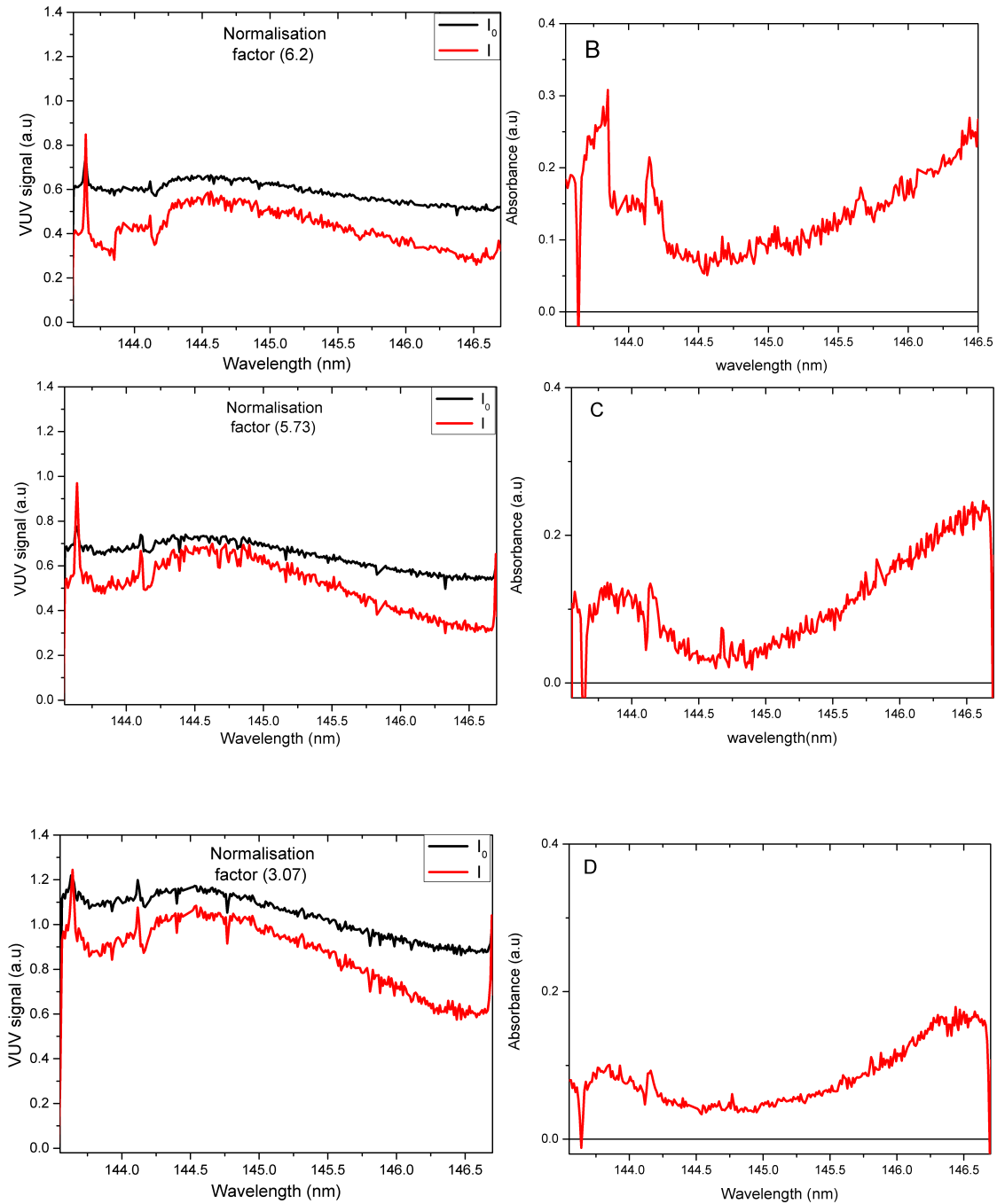


Figure 6.40: Absorption measurements of calcium fluoride samples using the tuneable VUV laser source. Measurements without (I_0) and with sample (I). Absorption spectrum on the right hand side. The graphs are label by the sample labels B-D

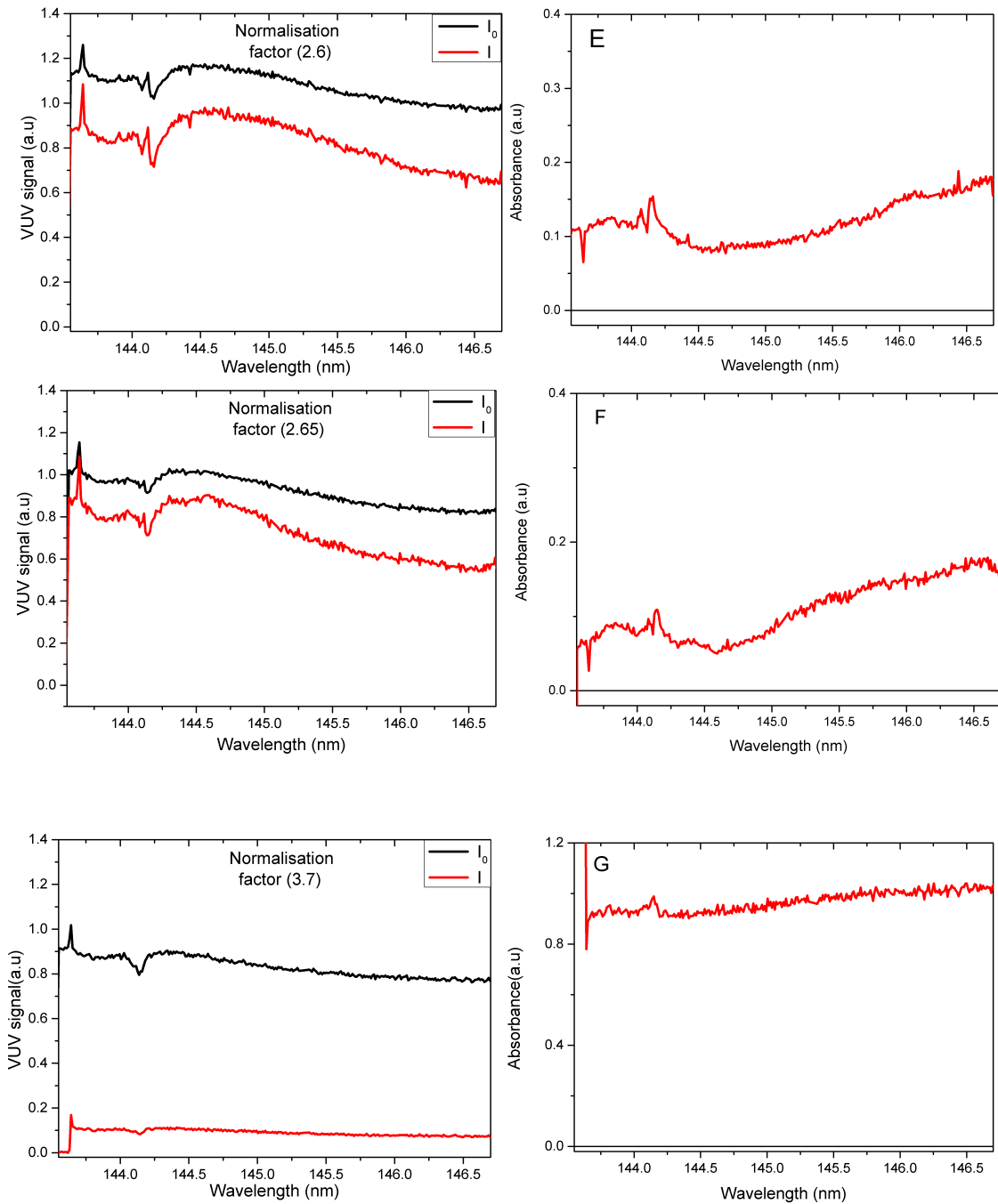


Figure 6.41: Absorption measurements of calcium fluoride samples using the tuneable VUV laser source. Measurements without (I_0) and with sample (I). Absorption spectrum on the right hand side. The graphs are label by the sample labels E-G

The experimental results obtained in the above figures show absorbance features at 143.63 and 144.14 nm. These observed features must be ignored since they are mirror images of the intensity spectra caused by the fact that the sensitivity of the PMTs are not the same. The adjustment of the high voltage and the normalisation of the PMTs does not solve the

problem. In addition, some spectra show more noise than others spectra. This is observed with the spectra which have bigger normalisation factors. This can be explained by the fact that the normalisation factor amplified in the PMT₂ signal but together with the noise. The general shape of each absorption curve looks like the mirror image (vertical) of the VUV spectrum measured with the sample. This is an artifact caused by the sensitivity difference of the PMTs. Therefore the increase in the absorption towards longer wavelengths is an artifacts. A decrease is expected according the monochromator spectra.

Despite the artifacts in the absorption spectra curves, it can be observed absorption features in all samples. Furthermore, sample A (pure sample) shows higher absorption than samples B-F. This should be due to fact that this sample was used much more than the other samples and was possibly dirty. Sample G shows a strong absorption more than other samples. This agree with the with the previous result obtained with the monochromator. If samples had significant and narrow (≤ 1 nm wide) absorption features in this range it would have been observed in spite of artifacts. These observation lead to the conclusion that from 144 nm to 146.7 nm there is no significant absorption peaks which can be related to the impurity in the samples, or to the STE states that may influence the one- or two photon absorption rate.

Chapter 7

Conclusions

7.1 Summary

The aim of this project was to develop techniques for measuring the absorption spectra of pure and lead (Pb) doped calcium fluoride crystal samples in the vacuum ultraviolet spectral range.

A vacuum scanning (McPherson model 225) with a deuterium lamp (McPherson model 632) was initially used for measuring the absorption measurements over a wider spectral range at a lower spectral resolution. Two sets of absorption spectra of CaF_2 samples in the 115-180 nm range were measured. Firstly, the absorption spectra recorded under the condition in which the sample cell was purged with 1 bar Nitrogen. Secondly, the absorption spectra of CaF_2 samples were recorded with the sample cell under vacuum condition. Our results show that total absorption of the VUV light by CaF_2 can be observed in 115-126 nm range. A similarity in the absorption spectra for samples A, B, C and D have been observed. It was deduced that sample D may also be a sample containing Na as an impurity. The lead doped samples E and F show similar spectra broad absorption feature at approximately 155 nm. Sample G shows a strong absorption more than others samples. This may be due to high concentration Pb doping, or doping with another impurity. In addition, the effect of vacuum and gas purged conditions and the influence of the stray light background in the monochromator have been determined.

The second part of this thesis was to do the absorption spectroscopy of CaF_2 samples using the tunable vacuum ultraviolet (VUV) laser light with a narrow spectral bandwidth generated by a 3rd order nonlinear optical process. The absorption spectra of CaF_2 samples in the 143-146.7 nm range was measured and absorption features in all samples have been observed. No significant peaks were observed which can be related to the STE in CaF_2 . Due

to the sensitivity difference of both PMTs, it is important to highlight that the general shape of the absorption spectra obtained with the VUV laser light are not accurate measurements of the absorption in the samples.

7.2 Conclusion regarding methods

In this thesis two different methods has been use for measuring the intensity of the incident light and light passing through the sample .

The first method using the monochromator and deuterium lamp involved measuring two spectra separately in which the first measurement is done without any sample in the light path while the second is recorded after a sample has been inserted in the light path. This method requires a constant intensity of the lamp output during the measurements since both spectra are not recorded simultaneously. The vacuum pressure into the monochromator and sample cell must be also taken into account. In our measurements, the second measurements are always better (showing a higher VUV intensity) than the first since the pressure keeps decreasing during the experiment as visualised in Figure 6.28. Therefore a strict measurement procedure was followed to make sure that the vacuum conditions are approximately the same in the I and I_o spectra that were used to calculate absorbance.

For the second method the incident light and the light passing through the sample are recorded simultaneously with two PMTs. This method was used with the laser source and required two PMTs, that should in the ideal circumstances have identical sensitivities. Our PMTs had different sensitivity curves and balancing the PMTs sensitivities by adjusting the high voltage was not sufficient. Therefore, the normalisation of the PMTs signals is needed before each measurement. We observed artifacts in spite of these methods. A systematic investigation of different instrument composing the data acquisition system (Boxcar, Data acquisition devise channels) has to be done for accurate measurements of the light intensity.

7.3 Conclusion regarding the possibility to observe STE states.

The scientific question in this thesis was to explore the possibility of observing the STE states in the CaF_2 using a narrow-bandwidth tunable VUV laser. The STE in CaF_2 is formed after a prior excitation of the sample by simultaneous absorption of two-photons. The previous experiments [1, 2] have shown that two-photon absorption coefficient in high

purity CaF_2 samples obtained with nanosecond pulses are about 3 factor bigger than the coefficient obtained with femtosecond laser pulses. This is explained by the fact that the pulse duration of the femtosecond laser pulse is shorter than the STE formation time (about 1 ps) [2]. This implies that the two-step absorption via intermediate STE state can not occur during the pulse. However, according to Mühlig et al, [2] the simultaneous absorption of two photons and the two-step absorption via intermediate STE energy states can occur within the long duration of the nanosecond laser pulses. This means that amount of total absorption will be wavelength dependent due to resonances with STE energy levels. Therefore, from this hypothesis we believe that by irradiating our samples with a nanosecond laser beam that has a tunable wavelength and narrow spectral bandwidth it is possible to observe absorption features that could be related to the STE state.

Our results do not show significant strong and narrow absorption features that could be associated with the STE state. This was expected with the monochromator because the light lamp of the monochromator is not intense enough to excite the electrons to the conduction band by two-photon absorption leading to the formation of STE states in the band gap. However, with our tunable laser light we did expect to observe it but unfortunately we did not. The possible reason could be the STE states are not within the wavelengths range of 143-146.7 nm investigated in this thesis.

7.4 Future work

Future investigation in the CaF_2 crystal should be done in order to find the exact energy levels of the STE states. This must be conducted using tunable VUV laser light with a narrow spectral bandwidth. Instead of the absorption measurement we believe that the laser induced fluorescence can be the suitable technique. The fluorescence wavelength 280 nm related to STEs should be recorded while tuning the VUV wavelength.

Appendices

Appendix A

Result and discussion

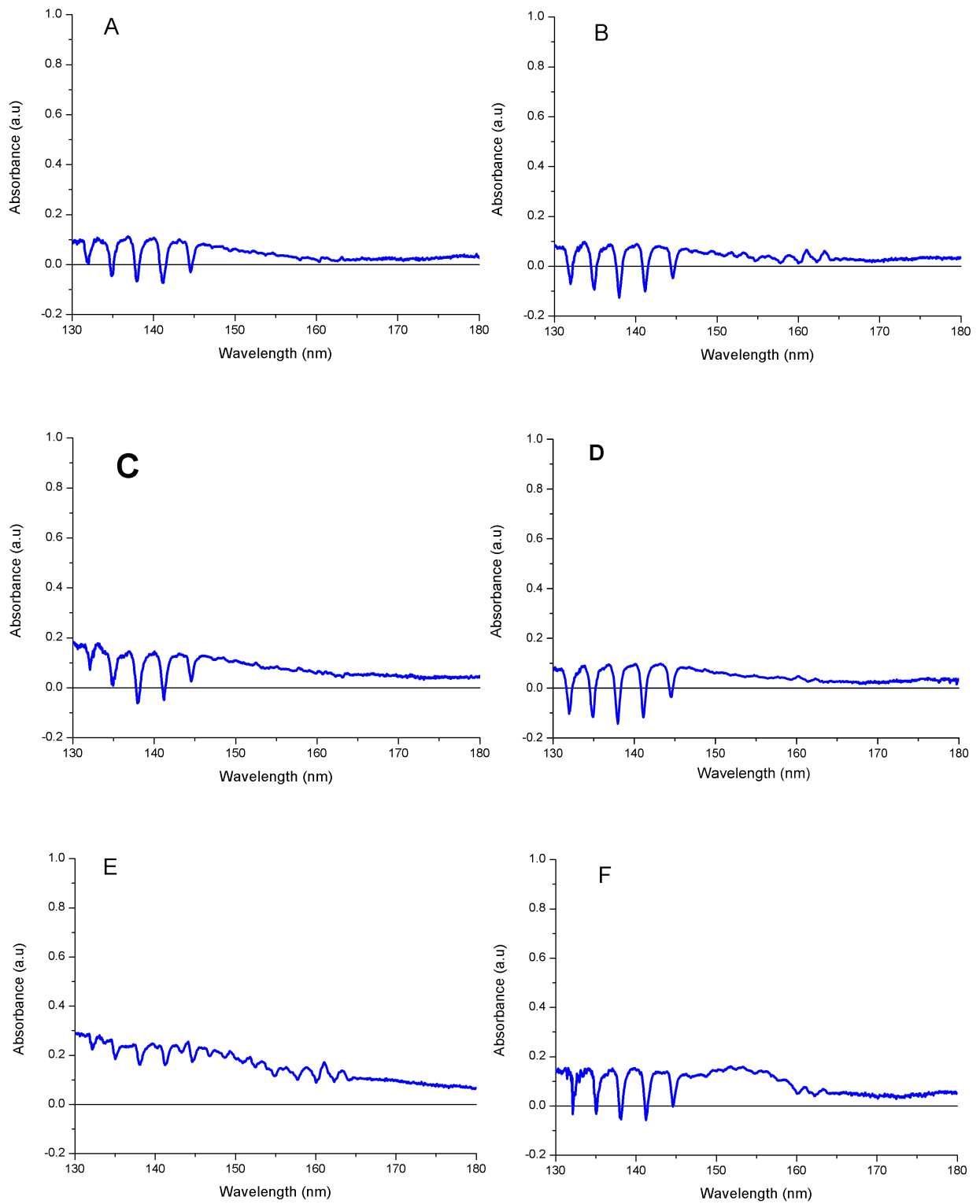
A.1 Data Processing

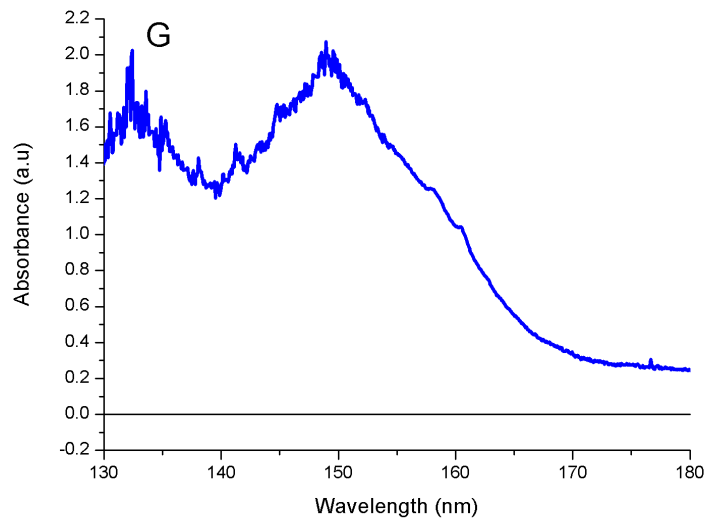
A.1.0.1 Measurement procedure with a gas purged sample cell

It is important to emphasise that when the sample is insert to the cell and before any other measurements, the evacuation of the cell is needed for 5 min and then the purge of nitrogen can start for at least 45 min before taking the next measurements. In order words, between two measurements taken with and without the sample, the sample cell must be evacuated for 5 min and flush 45 min with the nitrogen before starting to do the measurements. This requirement is also applicable for the last measurements (measurement after removing the sample). Scanning from 115 to 180 nm can take around 13 minutes if the scanning motor is set at 0.5 A min

A.1.0.2 Absorption measurements of CaF₂ samples recorded with sample cell purge with 1 bar nitrogen 5.0

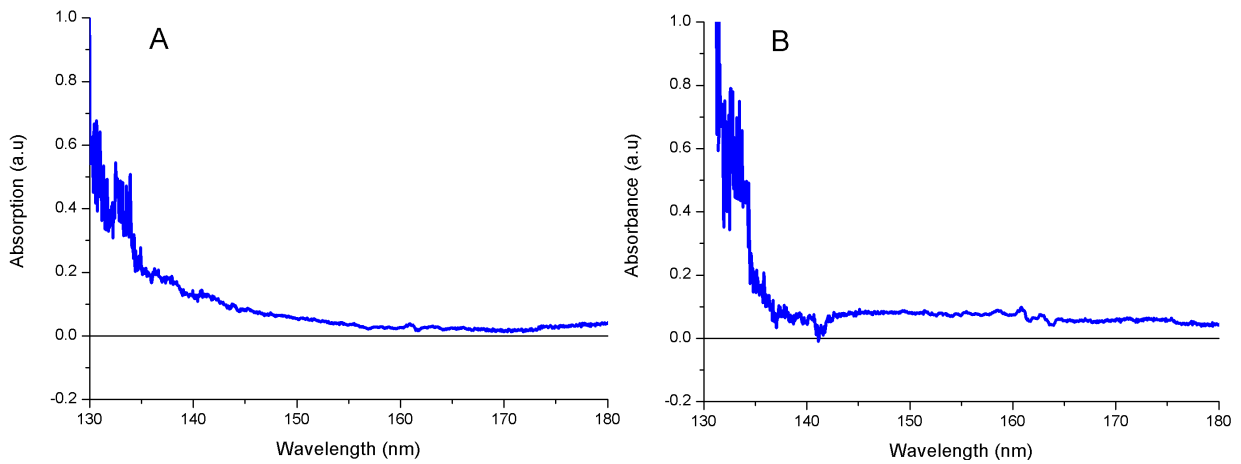
The following figures are the absorption measurements (130-180 nm) of pure and doped calcium fluoride samples recorded with sample cell purge with 1 bar nitrogen 5.0. The spectra were taken without the use of the extra tube to keep the optical path length in the gas the same. The figures are labelled with the letters A-G corresponding to labels at samples as on page [6.2.4](#).

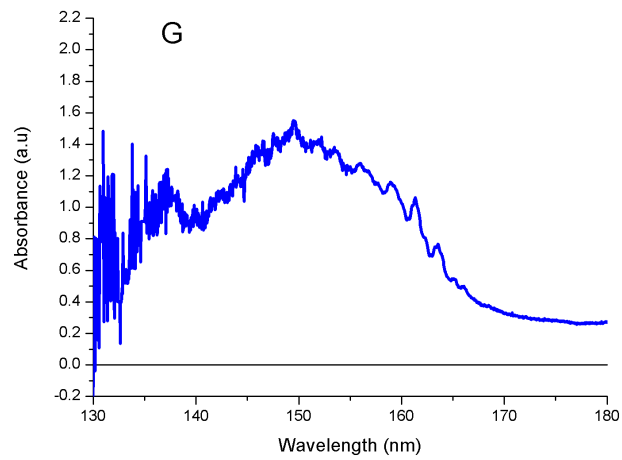
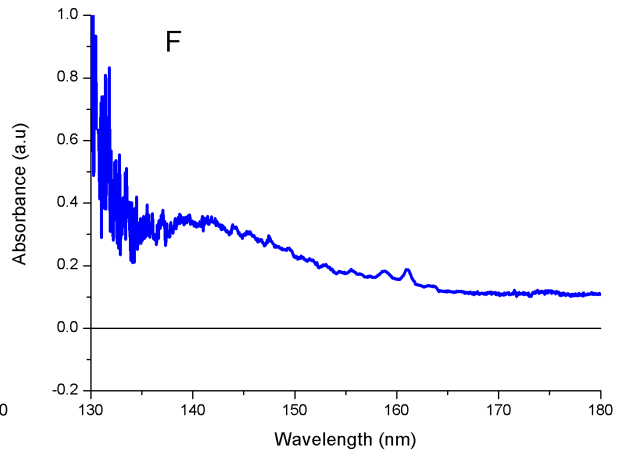
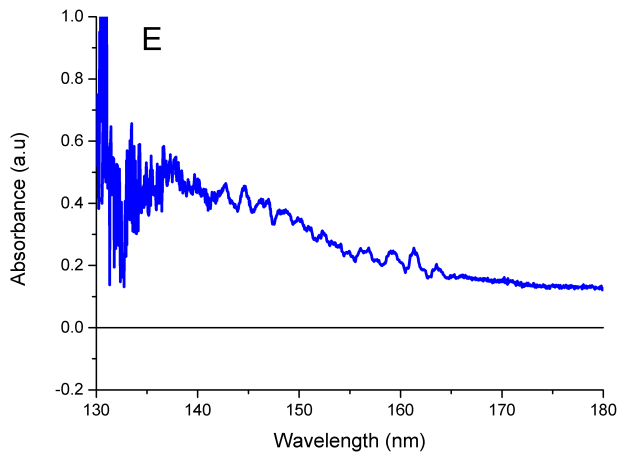
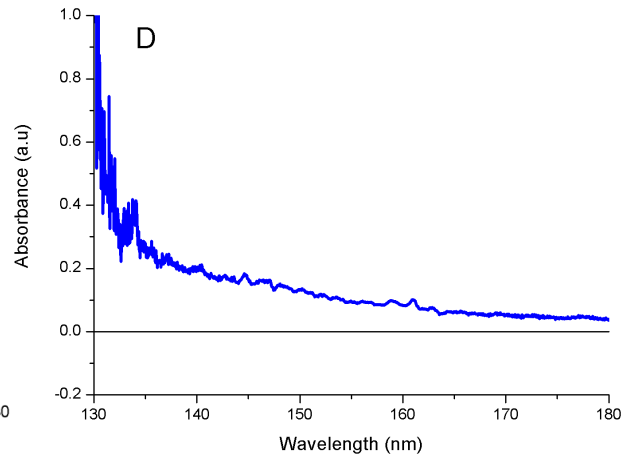
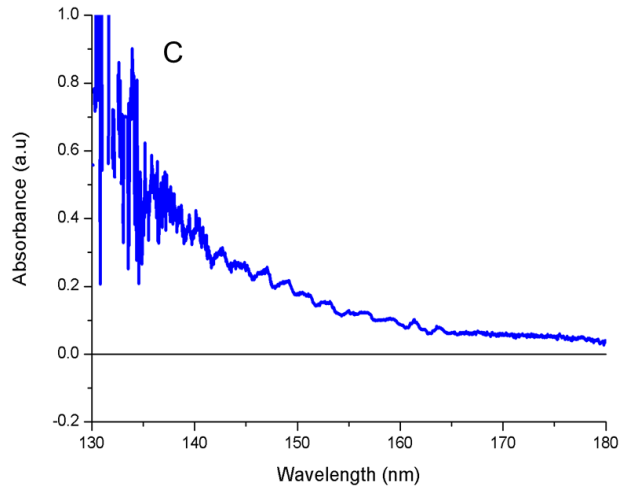




A.1.0.3 Absorption measurements of pure and doped calcium fluoride samples recorded with sample cell under vacuum

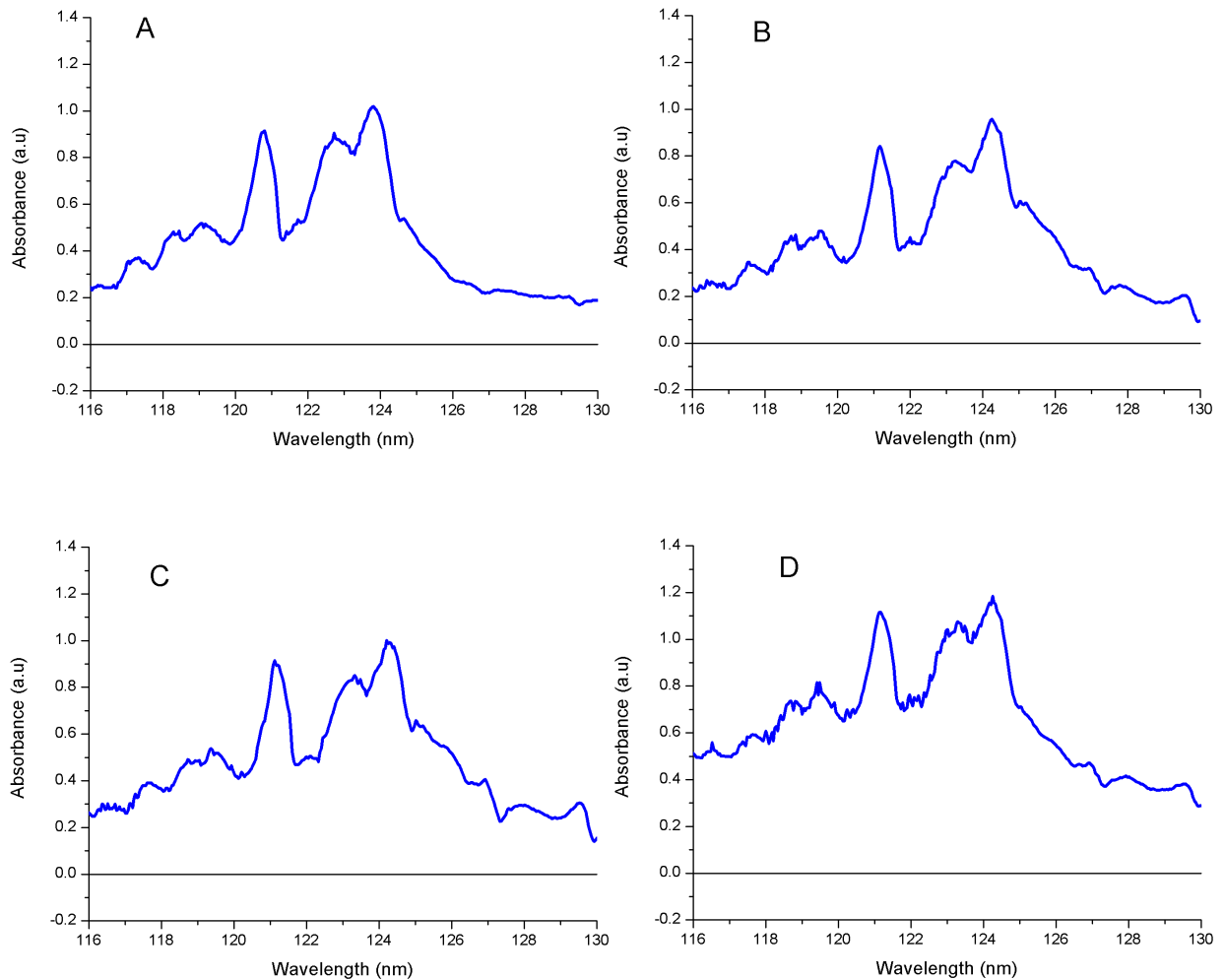
The following figure are the absorption measurements (130-180 nm) of CaF_2 samples recorded with sample cell under vacuum. The figures are labelled with the letters A-G corresponding to labels at samples as on page 6.2.4.

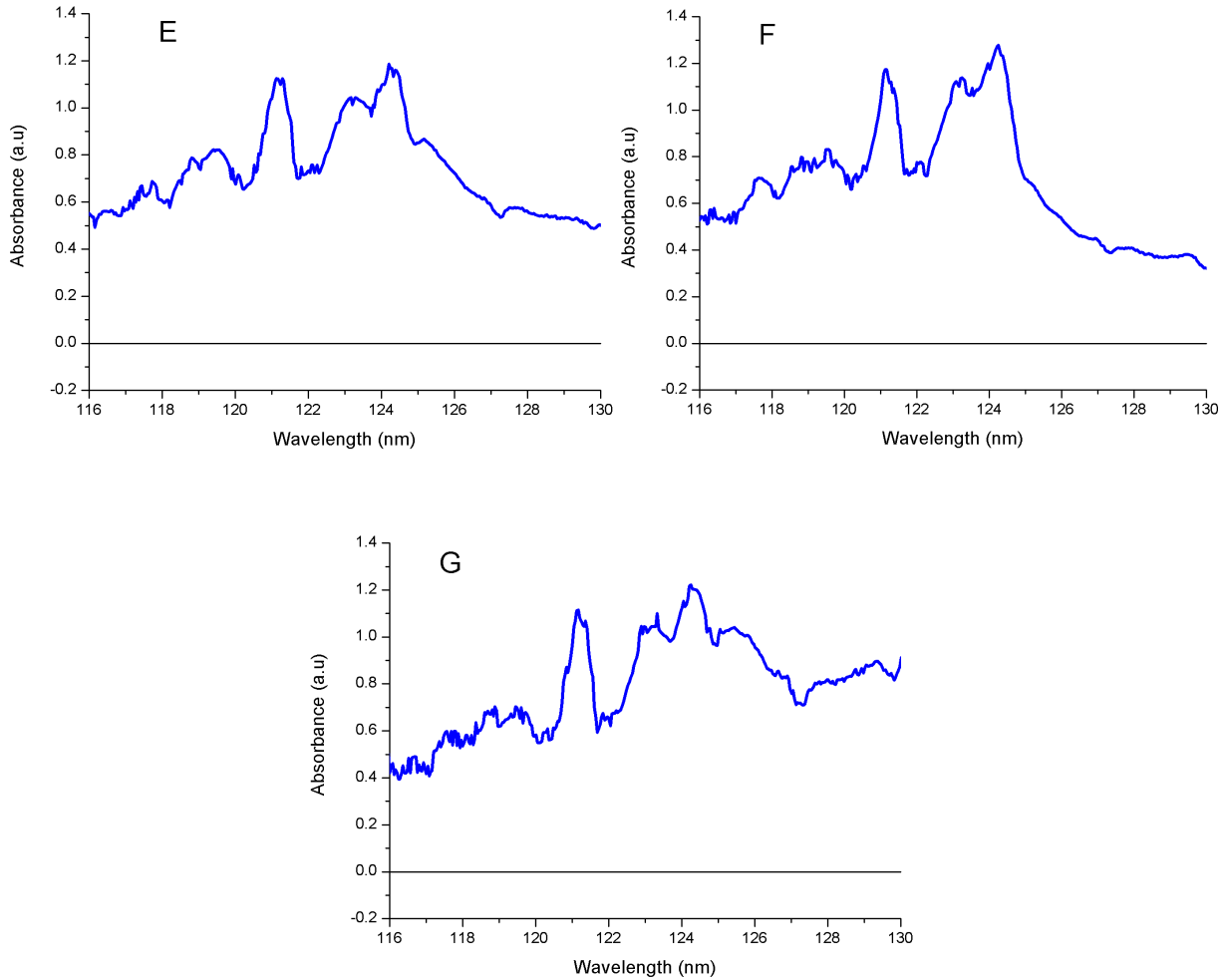




A.1.1 Absorption measurements of CaF_2 samples in 115-130 nm range

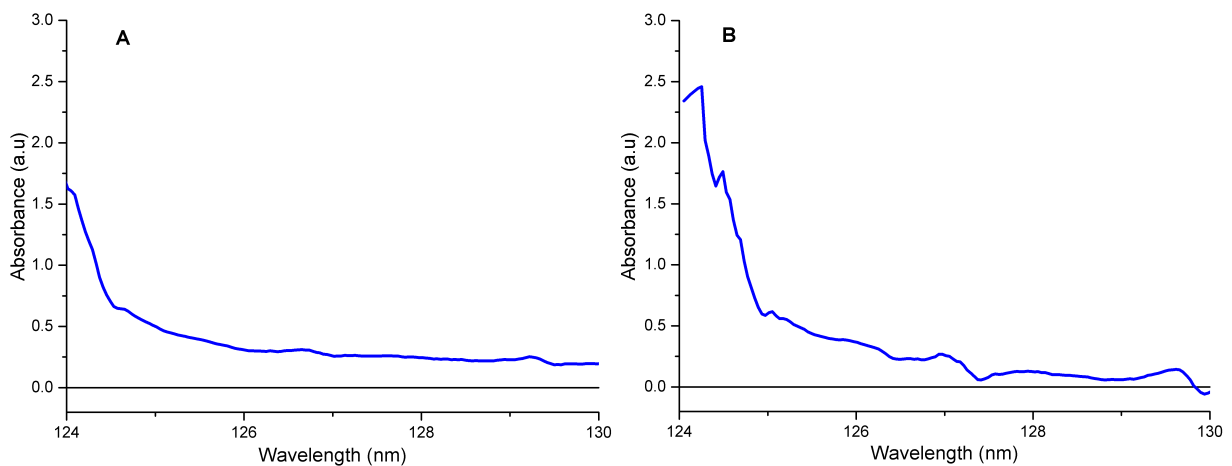
The following figures are the absorption measurements of pure and doped calcium fluoride samples recorded with sample cell purge with 1 bar nitrogen 5.0. The figures are labelled with the letters A-G corresponding to labels at samples as on page 6.2.4.

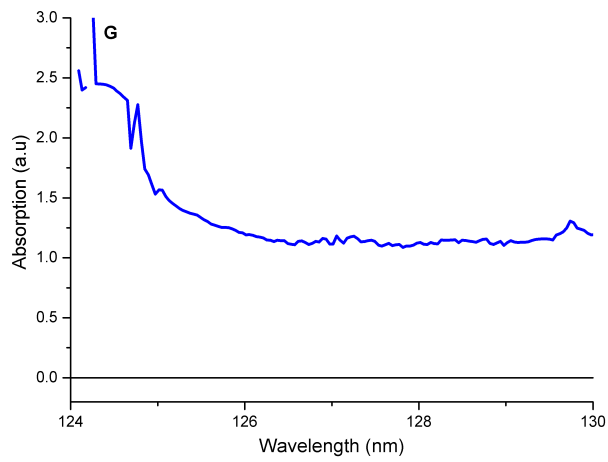
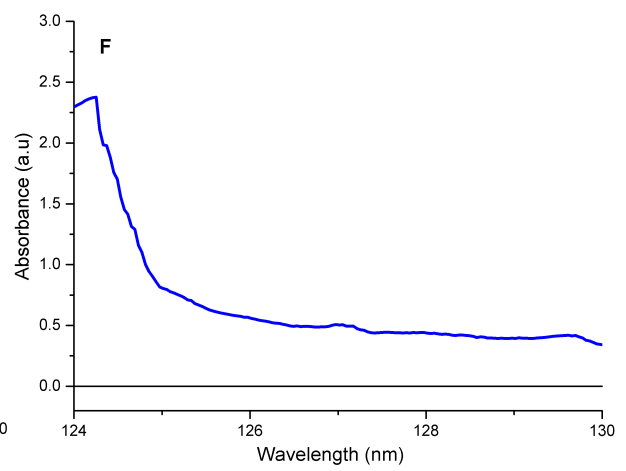
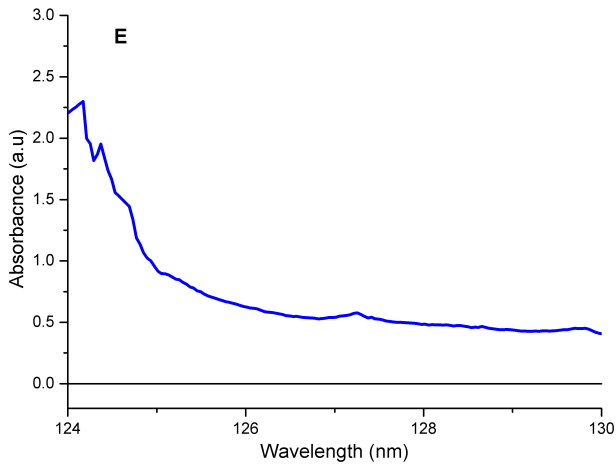
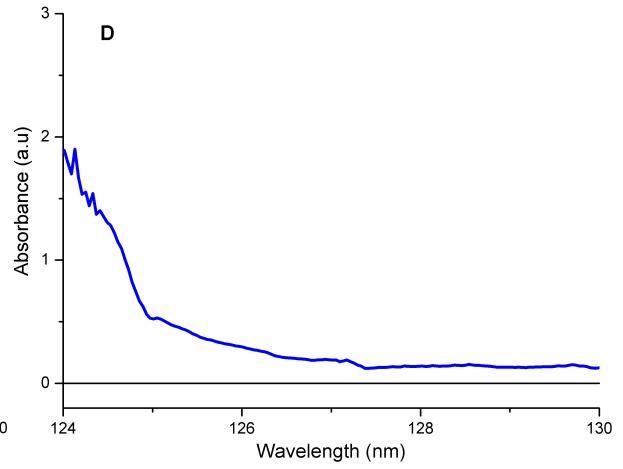
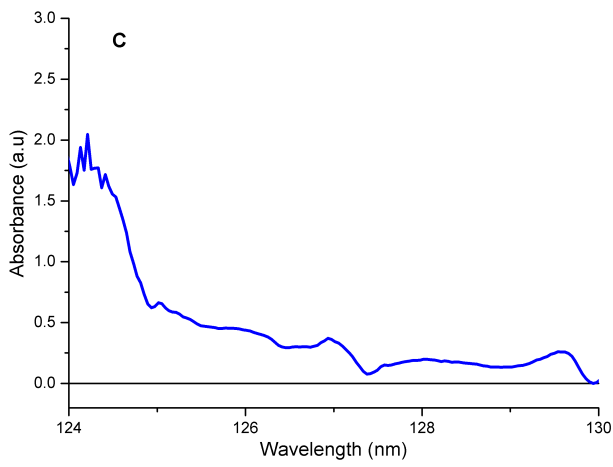




A.1.1.1 Physical reason for peaks at 116-126 nm

The following figures are the true absorption spectra of pure and doped calcium fluoride samples recorded with sample cell purge with 1 bar nitrogen 5.0. The figures are labelled with the letters A-G corresponding to labels at samples as on page 6.2.4.





List of References

- [1] C. Mühlig, W. Triebel, H. Stafast, and M. Letz. Influence of Na-related defects on ArF laser absorption in CaF₂. *Applied Physics B-laser and optics*, 99(3):525–533, 2010.
- [2] C. Mühlig, W. Triebel, H. Stafast, and M. Letz. Influence of Na-related defects on DUV nonlinear absorption in CaF₂: Nanosecond versus femtosecond laser pulses. *PROC SPIE*, 7504(1):7504i1–7504i14, 2009.
- [3] T. Zeuner, W. Paa, W. Triebel C. Mühlig, and H. Stafast. Picosecond kinetic confirmation of overlapping Ca cluster and M_{Na} absorption bands in UV grade CaF₂. *Journal of Applied Physics*, 110(5):056101–3, 2011.
- [4] C. M. Steenkamp. Nonlinear optics, 2013. Unpublished manuscript.
- [5] C. M. Steinmann. Development and characterisation of a tunable laser source in the vacuum ultraviolet. Master’s thesis, Stellenbosch University, December 1999.
- [6] R. W. Boyd. *Nonlinear Optics*. Number 133 in London. Providence, RI, 1992.
- [7] Christopher Palmer. *Diffraction Grating Handbook*. Newport Corporation, gratings@newport.com, seventh edition, 2014.
- [8] Ping Huang. Diagnostics in vuv laser spectroscopy. Master’s thesis, University of Stellenbosch, 2005.
- [9] Lakowicz. Principles of fluorescence spectroscopy. *Springer*, XXVI:954, 2006.
- [10] Nora H. de Leeuw and Timothy G. Cooperb. A computational study of the surface structure and reactivity of calcium fluoride. *Journal of Materials Chemistry*, 13:93–101, 2003.
- [11] S. M. Kaczmarek, T. Tsuboi, M. Ito, G. Boulon, and G. Leniec. Optical study of Yb³⁺/Yb²⁺ conversion in CaF₂ crystals. *Journal of Physics: Condensed Matter*, 17:3771–3786, 2005.
- [12] Marten Huisinga. *Ultraviolet photoelectron spectroscopy and electron stimulated desorption from CaF₂*. PhD thesis, Fachbereich Physik, Freie Universität Berlin, 1998.

- [13] Crystal lattice, calcium fluoride. [Online]. Available: <http://www.jeuilin.com> [2013, December 14] .
- [14] C. Karras, C. Mühlig, W. Paa, H. Stafast, W. Triebela, and T. Zeuner. Population kinetics of the fluorescing M_{Na} center state in CaF_2 upon fs laser excitation at 392 nm and 262 nm. *Laser-induced Damage in Optical Materials*, 7842(1):78421R–1–78421R–8, 2010.
- [15] C. Karras, C. Mühlig, W. Paa, H. Stafast, W. Triebela, and T. Zeuner. Femtosecond relaxation kinetics of highly excited M_{Na}^{**} states in CaF_2 at 3.2 eV and 4.7 eV. *Applied Physics B-laser and optics*, 104(1):17–20, 2011.
- [16] P. W. M. JACOBS and S. H. ONG. Point defect parameters for calcium fluoride from ionic conductivity measurements at low temperatures. *Journal de DE Physique*, 37:C7–331, 1976.
- [17] K.P. Oboth, F.J. Lohmeier, and F. Fischer. VUV and UV spectroscopy of Pb^{2+} and Bi^{3+} centers in alkaline-earth fluorides. *physica status solidi (b)*, 154:789–803, 1989.
- [18] S.B. Sastry and M. Kennedy. Optical absorption, fluorescence, and thermally stimulated emission on $\text{CaF}_2 : \text{Dy} : \text{Pb}$ single crystal. *Phys. C : Solid State Phys (b)*, 180:521, 1993.
- [19] I. Nicoara, M. Munteanu, N. Pecingina-Garjoaba, M. Stef, and L. Lighezan. Dielectric relaxation in PbF_2 -doped and X-ray irradiated CaF_2 crystals. *The Electrochemical Society*, 11:51–58, 2006.
- [20] Irina Nicoara and Marius Stef. *Modern Aspects of Bulk Crystal and Thin Film Preparation*, chapter Growth and Characterization of Doped CaF_2 Crystals, pages 72–96. InTech, 2012.
- [21] M. Fockelet, F. Lohsef, J-M. Spaethht, and R.H. Bartram. Identification and optical properties of axial lead centres in alkaline-earth fluorides. *J. Phys. Condens. Matter*, 1:13–26, 1989.
- [22] Anton du Plessis. *Laser Spectroscopy of the Fourth Positive System of Carbon Monoxide Isotopomers*. PhD, University of Stellenbosch, 2006.
- [23] A. Kramida, Yu. Ralchenko, J. Reader, and NIST ASD Team. NIST Atomic Spectra Database (ver. 5.1), [Online]. Available: <http://physics.nist.gov/asd> [2014, April 19]. National Institute of Standards and Technology, Gaithersburg, MD., 2013.
- [24] Steven R. Meier, June L. Tveekrem, and Ritva A. M. Keski-Kuha. A far-ultraviolet contamination-irradiation facility for in situ reflectance measurements. *Review of Scientific Instruments*, 69(NUMBER 10):3642, OCTOBER 1998.
- [25] B. Azmoun, R.P. Pisani, S. Stoll, and C. Woody. A study of the performance of the gas transmission monitor of the phenix hadron blind detector. In *Nuclear Science Symposium Conference Record*, pages 1931–1934. Department of Energy, Division of Nuclear Physics, November 2010.

- [26] McPherson, 7A Stuart Road, Chelmsford MA 0182. *Plasma Cleaning Vacuum Ultraviolet Optics to Obtain Good %T and %R Measurements.*
- [27] Mc Pherson, 7A Stuart Road, Chelmsford MA 01824 USA , Tel. 978-256-4512, Fax 978-250-8625 , Email MCP@McPhersoninc.com. *Vacuum Ultraviolet Deuterium Light Source.*
- [28] H.-C. Lu, H.-K. Chen H.-F.Chen, B.-M.Cheng, and J. F. Ogilvie. Absorption cross section of molecular oxygen in the transition $E^3 \sum_u^- V = 0 - X^3 \sum_g^- V = 0$ at 38 k. *Astronomy and Astrophysics*, 520:A19, 2010.
- [29] K. Watanabe, Murray Zelikoff, and Edward. C. Y. INN. Absorption coefficients of several atmospheric gases. *Geophysical Research Papers*, 21:1–76, 1953.
- [30] R.D. Hudson. Critical review of ultraviolet photoabsorption cross sections for molecules of astrophysical and aeronomic interest. *Review of geophysics and Spaces physics*, 9:106, 1971.
- [31] W. C. Price and George Collins. The far ultraviolet absorption spectrum of oxygen. *Physical Review*, 48:714–720, 1935.
- [32] Nikon Corporation, 10-1, Asamizodai 1-chome, Minami-ku, Sagamihara, Kanagawa 252-0328 Tel: +81-42-740-6746 Mail:glass.sales@nikon.co.jp. *Nikon NICF Series Calcium Fluoride*, 2013.
- [33] CRYSTRAN LTD, 1, Broom Road Business Park, Poole, BH12 4PA, UK TEL: +44 (0)1202 307650 FAX +44 (0)1202 307651 Email: sales@crystran.co.uk www.crystran.co.uk. *Crystran's Guide to Calcium Fluoride Grades*, july 2010.
- [34] Anton Christiaan Nortje. Development and application of tunable vuv laser sources. Master's thesis, Stellenbosch University, 2013.